HIGH CAPACITY SHORT-REACH OPTICAL TRANSMISSION SYSTEM BASED ON FIBER-EIGENMODE MULTIPLEXING

JIANBO ZHANG

PhD

The Hong Kong Polytechnic University

2023

The Hong Kong Polytechnic University

Department of Electrical and Electronic Engineering

High Capacity Short-reach Optical Transmission System based on Fiber-eigenmode Multiplexing

Jianbo ZHANG

A thesis submitted in partial fulfilment of the requirements for the degree of Doctor of Philosophy

Nov.2022

Certificate of Originality

I hereby declare that this thesis is my own work and that, to the best of my knowledge and belief, it reproduces no material previously published or written, nor material that has been accepted for the award of any other degree or diploma, except where due acknowledgment has been made in the text.

____________________________ (Signed)

Zhang Jianbo (Name of student)

Dedicated
To my Families

High Capacity Short-reach Optical Transmission System based on Fiber-eigenmode Multiplexing

Abstract

The fast development of bandwidth-hungry services is catalyzing the explosion of data in the current information and artificial intelligence (AI) era. Accordingly, the meteoric-growth capacity requirement has brought out the need to continuously accelerate the transmission rate to keep pace with the rapid-increasing traffic flow. Mode-division multiplexing (MDM), as an implementation of space-division multiplexing (SDM) technologies, is regarded as a promising solution to cope with the capacity crisis in fiber-based communication systems. Potentially, MDM can significantly increase the capacity of optical systems by multiplying the capacity of a single-mode fiber by the number of co-transmitted modes. Vector modes (VMs) are the full-vectorial eigenmodes supported by circular-core fibers. As true fiber-eigenmodes, VM-based MDM fiber transmission has captured much research interest recently. This thesis focuses on the studies of VM-based MDM short-reach optical transmission.

The primary characteristic of fiber eigenmode is first investigated based on the high-order Poincaré sphere model. Then, the propagation characteristic of VM through free space and few-mode fiber (FMF) is studied. For free-space optical (FSO) transmission, the travel behavior of four VMs multiplexing-based link is evaluated under three atmospheric turbulence conditions. For FMF transmission, VM characteristic along the FMF transmission is simulated and presented.

Based on VMs, two types of MDM short-reach fiber links, including uni-directional and bi-directional transmissions are demonstrated. For uni-directional transmission, two MDM links over 5 km FMF, including two VMs of the same order multiplexing transmission with 360 Gbit/s total capacity and two VMs of different orders multiplexing transmission with 400 Gbit/s total capacity are demonstrated based on Kramers–Kronig (KK) receiver, respectively. For bi-directional transmission, two MDM full-duplex bi-directional architectures including symmetrical and asymmetrical transmissions based on dual-VMs multiplexing over 3 km FMF are respectively implemented based on coherent detection and 2×2 MIMO. Firstly, four VMs, each carrying 14 GBaud quadrature phase-shift keying (QPSK) signal, is simultaneously employed on two terminals and a 224 Gbit/s homo-modal bi-directional transmission is demonstrated. To strengthen the immunity against backscattering crosstalk, hetero-modal bi-directional transmission is proposed, in which two VMs of $l = 0$ and two VMs of $l = +2$ are respectively utilized in the uplink and downlink and a 448 Gbit/s bi-directional transmission with 28 GBaud 16-ary quadrature amplitude modulation (QAM) modulation is realized. Furthermore, by combining with WDM technology, a 1.792 Tbit/s VM-based WDM-MDM full-duplex bi-directional transmission is also achieved.

Next, a versatile scheme of MG filter for mode-group division multiplexing (MGDM) IM/DD transmission is proposed and experimentally demonstrated over 5 km FMF in a 152 Gbit/s MIMO-free IM/DD MGDM dual-channel simultaneous transmission and detection system. The bit error ratios (BERs) of each channel are below 7% hard-decision forward error correction (HD-FEC) threshold under both static and dynamic tests. Finally, unlike most MIMO-based SDM/MDM demonstrations without consideration of singular problems, non-Singular MIMO DSP based on multi-user constant modulus algorithm (MU-CMA) is implemented on the four-VMs-multiplexed KK reception system with an aggregate rate of 448 Gbit/s. None of the singular phenomena is observed under both static and dynamic performance evaluation.

Acknowledgments

At the moment, I realize that I am almost approaching the end of my Ph.D. study. Hereby, I truly want to express the depth of my gratitude to a number of people in the course of my Ph.D. journey. Firstly, I am deeply indebted to my supervisor Prof. Chao Lu, for his continued guidance, support and encouragement. He gave me the opportunity to pursue my Ph.D at PolyU and I have benefited greatly from his expertise and experience sharing.

I take this opportunity to express my particular thanks to Prof. Zhaohui Li from Sun Yat-sen University and his research group members, including Dr.Jiangping Li, Dr. Xingwen Yi, Dr. Shecheng Gao, Dr. Jiajing Tu and Mr. Jiawei Luo. They offered me lots of valuable suggestions and support during my study trip at Sun Yat-sen University.

In addition, I would like to thank Mr. Xiong Wu for the continuous collaboration, academic discussion and practical help. He is always full of energy and has many interesting ideas. My sincere thanks also go to Ms. Yaxi Yan, Ms YuYao Wang, Mr. Yu Wang, Mr. Zhuo Wang, Mr. Jingchuan Wang and Mr. lingwang Lu and many others. Without their support and help, I cannot complete the work in this thesis. My thanks are also extended to other colleagues in the Photonics Research Center. Many thanks also go to my roommates Ms. Di Yang and Ms. Nico, thank you for listening, giving me advice, and supporting me.

Moreover, I must express the depth of my gratitude to my dear parents, for their unconditional love and encouragement.

Finally, I am grateful to PolyU. My life in PolyU is an unforgettable experience.

Publication List (relevant to this dissertation)

Journals:

[1] **Jianbo Zhang**, Xiong Wu*, Alan Pak Tao Lau, Zhaohui Li, and Chao Lu, "Dynamic analysis of PAM-4 IM/DD OAM-based MGDM transmission enabled by mode-group filter approach," *Optics Letters*, **48**(12), 3259-3262 (2023).

[2] Xiong Wu, **Jianbo Zhang***, Qirui Fan, Zhongwei Tan*, Jianping Li, Xingwen Yi, Zhaohui Li, Alan Pak Tao Lau, and Chao Lu, "Dynamic Evaluation of Four CV Modes Multiplexing System using KramersKronig Reception and 4×4 Non-Singular MIMO," *Journal of Lightwave Technology* **40**(7), 1962-1971 (2021).

[3] **Jianbo Zhang**, Xiong Wu*, Qirui Fan, Xingwen Yi*, Zhongwei Tan, Jianping Li, Zhaohui Li, and Chao Lu, "High-capacity bi-directional full-duplex transmission based on fiber-eigenmode multiplexing over a FMF with 2×2 MIMO," *Optics Express* **29**(19), 30473–30482 (2021).

[4] **Jianbo Zhang**, Xiong Wu*, Jianping Li*, Linyue Lu, Jiajing Tu, Zhao Li, and Chao Lu, "Fiber Vector Eigenmode Multiplexing Based High Capacity Transmission Over 5-km FMF With Kramers-Kronig Receiver," *Journal of Lightwave Technology* **39**(15), 4932–4938 (2021).

[5] JiaJing Tu, Zhengyong Liu*, Shecheng Gao, Zhuo Wang, **Jianbo Zhang**, Bin Zhang, Jianping Li, Weiping Liu, Hwayaw Tam, Zhaohui Li, Chanyuan Yu, and Chao Lu, "Ring-core fiber with negative curvature structure supporting orbital angular momentum modes," *Optics Express* **27**(15), 20358–20372 (2019).

Conferences:

[1] **Jianbo Zhang**, Xiong Wu*, Zhuo Wang, Jiajing Tu, Zhaohui Li, and Chao Lu,"MIMO-free two-mode-multiplexing transmission over 10-m hollow-core fiber," in *28th Optoelectronics and Communications Conference (OECC),* (Optical Society of America, 2023), Accepted.

[2] **Jianbo Zhang**, Xiong Wu*, Zhaohui Li, and Chao Lu, "Performance of CVB-based MDM FSO Link under Atmospheric Turbulence using 4×4 Non-Singular MIMO," in *27th Optoelectronics and Communications Conference (OECC),* (Optical Society of America, 2022), pp. 1-3.

[3] **Jianbo Zhang**, Xiong Wu*, Qirui Fan, Xingwen Yi, Zhongwei Tan, Jianping Li, Zhaohui Li, and Chao Lu, "4×56 Gb/s MIMO-less Fiber-eigenmode multiplexing transmission over 3 km FMF," in *26th Optoelectronics and Communications Conference (OECC),* (Optical Society of America, 2021), p. W3B.3.

[4] **Jianbo Zhang**, Xiong Wu*, Linyue Lu, Jianping Li*, Jiajing Tu, Zhaohui Li, and Chao Lu, "1.12 Tbit/s fiber vector eigenmode multiplexing transmission over 5-km FMF with Kramers-Kronig receiver," in *Optical Fiber Communication Conference (OFC) 2020,* (Optical Society of America, 2020), p. W1D.5.

Contents

List of Figures

List of Tables

List of Abbreviations

5G	The fifth generation
ACF	Air core fiber
AI	Artificial intelligence
AM	Angular momentum
ASE	Amplified spontaneous emission
AT	Atmospheric turbulence
AWG	Arbitrary waveform generator
BER	Bit error rate
CCD	Charge-coupled device camera
CDM	Core division multiplexing
CIR	Circulator
CMA	Constant modulus algorithm
CSPR	Carrier-to-signal power ratio
CVBs	Cylindrical vector beams
CW	Continuous wave
DCI	Data center interconnect

DeMUX	Demultiplexer
DGD	Differential group delay
DMGD	Differential mode group delay
DoF	Degree of freedom
DP	Dual-polarization
DSP	Digital signal processing
EA	Electrical amplifier
ECL	External cavity laser
EDFA	Erbium-doped fiber amplifier
FFE	Feed-forward equalizer
FMF	Few-mode fiber
FMF-PC	Few-mode fiber-based polarization controller
FO	Frequency offset
FR	Fresnel reflection
FSO	Free space optical
HD-FEC	Hard decision forward error correction
HKT	Hong Kong time
HWP	Half-wave plate
I/Q modulator	In-phase/quadrature modulator
IoT	Internet of things
ISI	Inter-symbol interference
KK	Kramers-Kronig
LO	Local oscillator

LP	Linearly polarized
MCF	Multicore-fiber
MDG	Mode-dependent gain
MDL	Mode-dependent loss
MDM	Mode-division multiplexing
MGDM	Mode-group division multiplexing
MGs	Mode groups
MIMO	Multiple-input multiple-output
MMF	Multimode fiber
MRC	Maximal ratio combining
MU-CMA	Multi-user constant modulus algorithm
MZM	Mach-Zehnder modulator
NOMA	Non- orthogonal multiplexing access
NPBS	Non-polarizing beam splitter
OAM	Orbital angular momentum
OBPF	Optical bandpass filter
OC	Optical coupler
ONU	Optical network unit
OSC	Oscilloscope
PAM-4	Four-level pulse-amplitude-modulation
PBC	Polarization beam combiner
PBS	Polarization beam splitters
PC	Polarization controller
PDL	Polarization-dependent loss
PDM	Polarization-division multiplexing

PDs	Photodetectors
PG	Polarization grating
PM-RCF	Polarization-maintaining ring-core fiber
PM-VOA	Polarization-maintaining variable optical attenuator
PMC	Polarization-maintaining coupler
PMF	Polarization-maintaining fiber
PON	Passive optical network
QAM	Quadrature amplitude modulation
QPSK	Quadrature phase-shift keying
RB	Rayleigh back scattering
RC	Raised-cosine
RCF	Ring core fiber
RDE	Radius directed equalizer
RF	Roll-off factor
SDM	Space-division multiplexing
SE	Spectral efficiency
SEFDM	Spectrally efficient frequency division multiplex
SIMO	Single-input multiple-output
SISO	Single-input and single-out
SMF	Single-mode fiber
SNR	Signal to noise ratio
SoP	State of polarization
SSB	Single side band
TDM	Time division multiplexing
TIA	Trans-impedance amplifier

VMs	Vector modes
VOA	Variable optical attenuator
VPP	Vortex phase plate
VQF	Vector quality factor
VWP	Vortex wave plate

WDM	Wavelength-division multiplexing
WRON	Wavelength-routed optical network
WSS	Wavelength selective switch

List of Major Notations

$\mathbf{E}$	Electric field
$\mathbf{H}$	Magnetic field
λ	Wavelength
β	Propagation constant
k	Wave number
ε_0	Permittivity of vacuum
μ_0	Permeability of vacuum
ω	Angular frequency
n	Refractive index
V	Normalized frequency
U	Normalized transverse phase parameter
W	Normalized transverse attenuation parameter
d_R	Rayleigh range
w_0	Radius of the beam waist
l	Azimuthal order of fiber modes
m	Radial order of fiber modes
$\boldsymbol{\Psi}$	Optical field
$\boldsymbol{J}$	Total angular momentum of the beam
$\mathbf{S}$	Stokes vector
ψ	State of polarization
σ_i	Expectation value of each Pauli operator
n_{eff}	Effective refractive indice

1

Introduction

In this chapter, the derivation and development of space-division multiplexing/mode-division multiplexing (SDM/MDM) technique are first reviewed. Afterwards, the challenges of SDM/MDM-based fiber communication systems are illustrated. Then, the research objectives and organization of this thesis are given.

1.1 Overview of SDM/MDM

Optical communication networks, which are unchallenged for global data transmission with low cost and low latency, have been experiencing the ongoing revolution since its introduction in the 1970s[3–5]. Fueled by the relentless exponential growth of traffic demand, numerous technological breakthrough and strategies including ultra-low-loss optical fibers, erbium-doped fiber amplifiers (EDFA), multiplexing techniques in the physical dimensions of time, frequency, polarization and phase, and digital coherent receiver have been deployed to keep pace with the capacity trend. The evolution of key optical communication technologies driving the ever-increasing capacity around tenfold every 4 years is depicted in Fig.1.1.

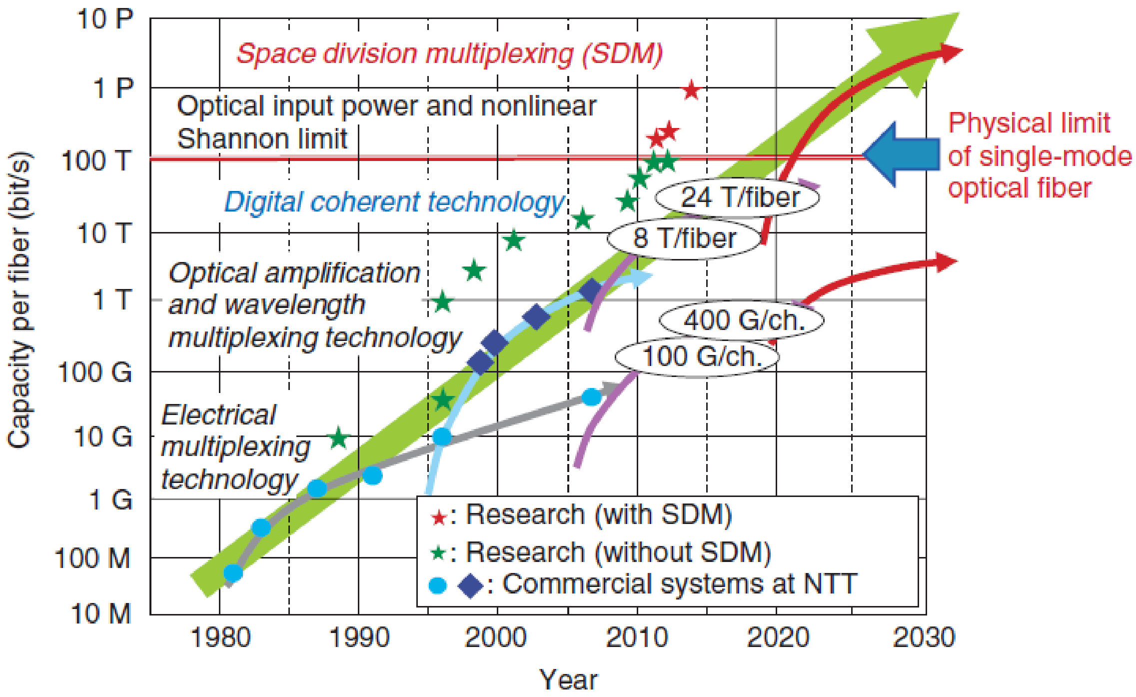

Figure 1.1: Evolution of communication capacity based on optical fibers as well as future forecast[1].

According to the theoretical Shannon limit, the standard single-mode fiber (SMF)-based traditional optical transmission systems are gradually approaching saturation — 100 Tbit/s, which are enabled by fully utilizing C and L bands via optical amplifiers at a spectral efficiency (SE) of approximate 10 bit/$(\mathrm{s} \cdot \mathrm{Hz})$[3,6]. Undoubtedly, In the

5G and artificial intelligence (AI) era, a more reliable, efficient and significant upgrade of the backbone network is needed to accommodate the high-throughput requirement. However, enhancing the transmission speed beyond 100 Tbit/s by SMF-based architecture has been perceived to be extremely hard due to limited SE and limited incident power density. Against this background, space division multiplexing (SDM) scheme, which exploits the spatial granularity as parallel communication channels to carry information streams has been proposed to break the forthcoming capacity bottleneck[7]. In fact, the first relatively obvious scheme for SDM could be dated back to 1979, when optical fibers started to take over the function of coaxial cables in the long-haul communication[8]. However, it was only until recent years that substantial attention has been paid to exploring the potential of SDM to upscale the per-fiber capacity, because all other physical dimensions in the field of optical communication have been almost exhausted[9–12]. SDM-based structures can be mainly categorized into three types:

(1) Fiber bundles with several physically independent SMF together. Fiber ribbon is an early attempt at SDM and is already commercially available. On the one hand, it is the most straightforward scheme for its compatibility and simplicity. On the other hand, it receives little interest due to low spatial channel density and low-level integration for SDM schemes.

(2) Few-mode fiber (FMF)/multimode fiber (MMF) with a single core supporting a limited/multiple number of fiber modes at a certain wavelength. It is noted that there are lots of specially designed FMF, such as elliptical core fiber[13], trench-assisted fiber[14], air-core fiber (ACF) and ring core fiber (RCF)[15,16]. FMF/MMF-based transmission links are generally classified as mode-division multiplexing (MDM), which utilizes mutually orthogonal spatial modes as the individual information-carrying channels to increase capacity density in proportion to the number of co-transmitted mode channels (Fig.**1.2** (b)). To study the optimal performance of various basis sets of fiber mode, there have been plenty of works on MDM systems based on linearly polarized (LP) modes, orbital angular momentum (OAM) mode, Bessel modes and vector mode (VM) up to now.

(3) Multicore-fiber (MCF) containing many cores incorporated in a single cladding, where each core could be SMF or FMF (Fig.1.2 (c)). MCF is generally sorted into two categories. One is the strong-coupled MCF with a higher core density that allows the propagation of supermodes. Due to strong channel-to-channel coupling, equalization by full multi-input multi-output (MIMO) process is essential to handle this impairment. At the same time, the strong mode mixing following the random-walk process during the propagation is beneficial to alleviate the impairment of mode-dependent loss/gain (MDL/MDG) and differential group delay (DGD) to some extent, because MDL and DGD are proportional to the square root of the transmission length instead of linearly. Another type is weakly-coupled MCF with enough core pitches to suppress inter-core crosstalk. Considering the limitation of the maximum fiber cladding diameter in practice, a variety of design schemes for weakly-coupled MCF have been proposed to realize higher spatial density and further reduce crosstalk between neighboring cores, such as hole-assisted MCFs, trench-assisted MCFs and heterogeneous MCFs. Compared with multi-core single-mode fiber (MC-SMF), multi-core few-mode fiber (MC-FMF) could achieve higher spatial efficiency and higher spatial channel count by the combination of core and mode multiplexing, which can be a potential candidate for ultra-dense SDM transmission.

Table 1.1 summarizes the representative SDM-based transmission systems from the literature in recent works in both single-core FMF/MMF and multicore fiber. It can be seen that SDM-based transmission has achieved a total capacity of 10.66 Pbit/s over 13 km 38-core-3-mode fiber and a total capacity of 105.1 Tbit/s over 14350 km 12-core-single-mode fiber, which indicates SDM is a promising scheme to provide a big jump for both short reach and long-haul transmission in the near future.

In the SDM/MDM-based fiber-optic link, the transmission signal will be degraded by the linear and nonlinear impairments, which absolutely necessitates the digital signal process (DSP) dealing with these issues. Multiple input–multiple output (MIMO) processing with multiple equalizers is commonly employed in the SDM/MDM networks to dynamically address linear impairments including crosstalk and differential mode

Table 1.1: Representative SDM-based transmission systems in recent works.

Fiber type		Distance (km)	Modulation format	MIMO DSP	Total capacity (Tbits^{-1})	Spectral efficiency ($\mathrm{bits}^{-1}\ \mathrm{Hz}^{-1}$)	Capacity-distance Product ($\mathrm{Tbits}^{-1} \cdot \mathrm{km}^{-1}$)	Number of spatial channels	Number of WDM channels	Refs
FMF/MMF	FMF	48-km	PS-16QAM	2×2 MIMO 4×4 MIMO	402.7	39.7	19329.6	20	750	Ref[17]
	FMF	26.5-km	8 QAM	90×90 MIMO	101	202	2676.5	90	20	Ref[18]
	MMF	23-km	64 QAM	30×30 MIMO	1010	105.8	23230	30	382	Ref[19]
	RCF	18-km	8 QAM	MIMO-free	8.4	3.0	151.2	2	112	Ref[20]
	RCF	100-km	QPSK	4×4 MIMO	2.56	10.2	256	8	10	Ref[21]
MC-FMF	MC-SMF	31-km	64 QAM	2×2 MIMO	2150	215.6	66650	44	399	Ref[22]
	MC-SMF	14350-km	8D APSK	2×2 MIMO	105.1	38.4	1510000	24	82	Ref[23]
	MC-SMF	2040-km	16 QAM	6×6 MIMO	172	17.8	351000	6	359	Ref[24]
	MC-FMF	11.3-km	16 QAM 64 QAM	12×12 MIMO	10160	1100	114808	228	739	Ref[25]
	MC-FMF	13-km	64 QAM 256 QAM	6×6 MIMO	10660	1158.7	138580	228	368	Ref[26]

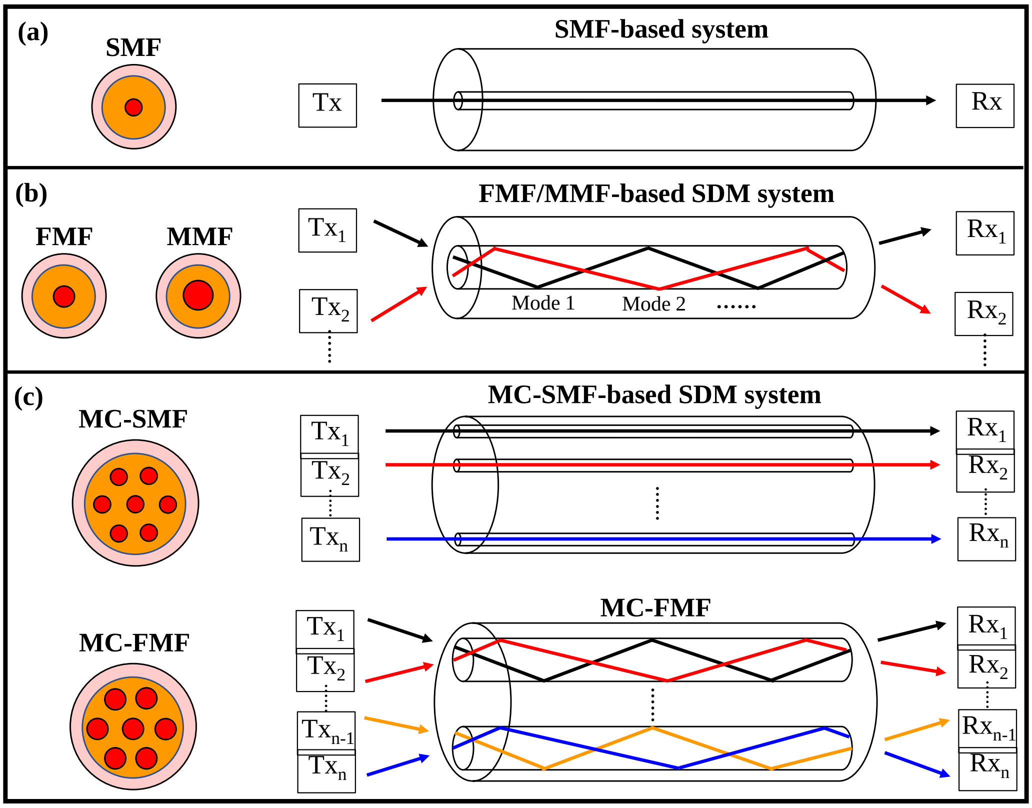

Figure 1.2: (a): Conventional optical transmission system based on SMF. (b) and (c): Two main types of SDM systems based on FMF/MMF or MC-SMF/ MC-FMF, respectively. Tx: transmitter; Rx: receiver.

group delay (DMGD) among different spatial channels[27,28]. According to the size of MIMO, SDM/MDM architecture can be classified into three categories, including full-MIMO, partial-MIMO and MIMO-free transmission, which are respectively illustrated in Fig.1.3 (a), (b) and (c). Full-MIMO SDM scheme could realize high spectral efficiency, high spatial mode density and robust performance at the price of high cost, high DSP complexity and high power consumption. The complexity of the time domain MIMO DSP is governed by the number of transmitted modes and the number of taps in the MIMO equalizer. The number of equalizers increases squarely with the number of co-transmitting spatial channels and the number of taps (memory depth) per equalizer is determined by the maximum differential mode/mode-group delay (DMD/DMGD) which is increased with transmission distance. Table 1.2 lists some demonstrations of full-MIMO SDM-based transmission systems. Core division multiplexing (CDM) based on supermodes in coupled MC-SMF is a representative example, allowing large mode effective area and high spatial density. Super-modes can be treated as a superposition of modes of strongly-coupled cores and the mixed signals of super-modes can be recovered by full-MIMO processing at the receiver side. In recent publications, the MDM transmission with a mode multiplicity of 90 over 26.5 km MMF has been demonstrated and 90×90 MIMO with more than 300 taps is utilized to compensate for mode coupling and DMD among these mode channels. For the practicality and commercialization of SDM link, however, such large-scale MIMO DSP is difficult to realize and the number of taps is impractical for DSP processing. Thus, it is highly significant to reduce the cost and DSP complexity of SDM links. To alleviate the burden of MIMO processing, two opposite technical road maps including strong coupling and weak coupling schemes are taken into account. For the former, low-DMD fiber with enhanced coupling among different spatial channels is the most suitable choice to reduce the impulse response width, thereby combating DMD accumulation during the fiber propagation, especially long-haul transmission. However, the computational load is still heavier compared to that in a weakly-coupling regime with partial-MIMO or MIMO-free processing. Partial-MIMO is regarded as a tradeoff between full-MIMO with optimal performance and MIMO-free at minimal cost, in which MIMO block is only used for impairment equalization and channel demultiplexing among partial spatial channels with severe crosstalk, thereby making SDM scenarios more applicable. Some representative partial-MIMO SDM-based transmission systems are listed in Table 1.3. Partial-MIMO mode group division multiplexing (MGDM) scheme is a typical example of jointly reducing the MIMO size and increasing the spatial mode channels, in which crosstalk between adjacent mode groups (MGs) is guaranteed a reasonable level after transmission and MIMO block is only performed over degenerated modes within one MGs, thereby reducing the DSP complexity. A MIMO-free SDM scheme is the most cost-effective system with the simplest implementation. For such systems, negligible crosstalk among spatial channels is the most essential factor. To effectively suppress modal crosstalk, specially-designed fiber such as air-core fiber, elliptical-core FMF, and polarization-maintaining ring-core fiber (PM-RCF) are proposed to differ the effective refractive index space which is the critical determinant for intermodal crosstalk among spatial channels. Moreover, because modal crosstalk will accumulate during the fiber transmission, MIMO-free SDM systems are generally realized in short-reach fiber links with relatively fewer spatial channels. Table 1.4 lists some representative works of MIMO-free SDM-based transmission systems in recent years.

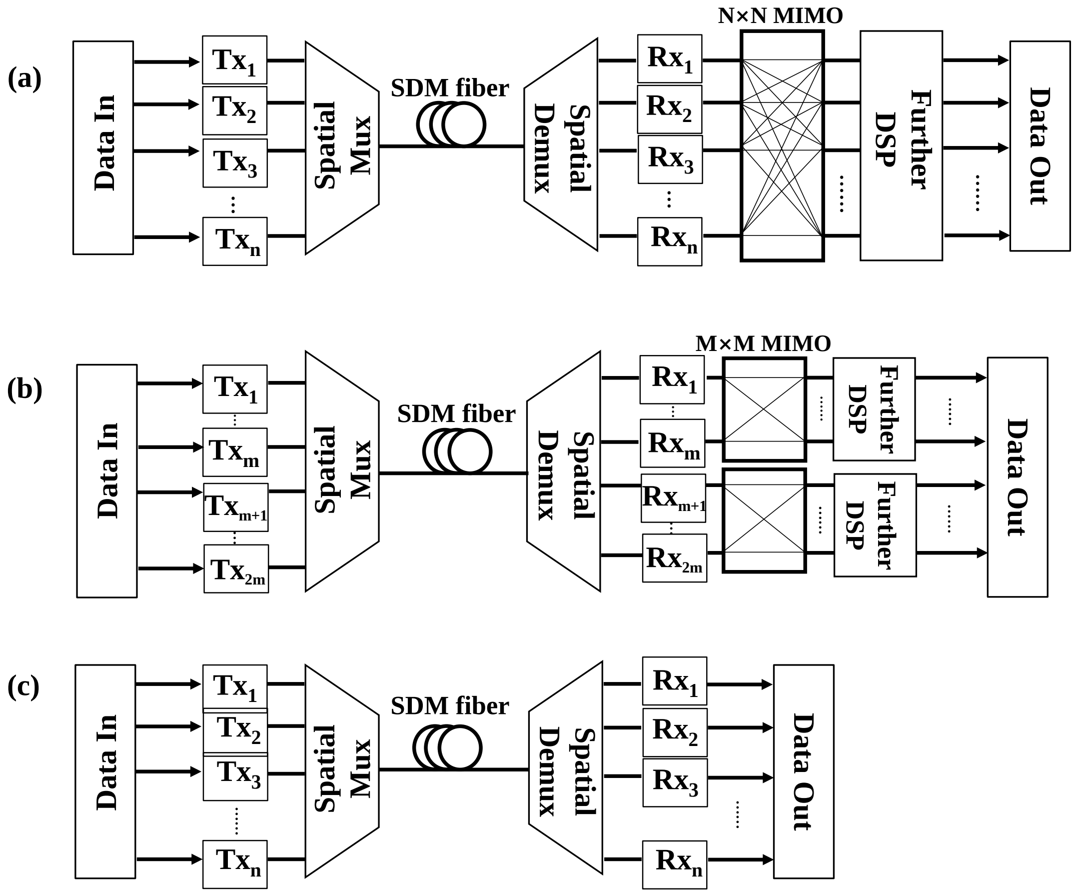

Figure 1.3: SDM-based (a) full-MIMO, (b) partial-MIMO and (c) MIMO-free fiber transmission systems.

Table 1.2: Representative full-MIMO SDM-based transmission systems in recent works..

Fiber type	Distance (km)	Modulation format	Total capacity (Tbits^{-1})	Number of spatial channels	MIMO DSP	Mode basis	Refs
RCF	1	16-QAM	1.12	10	10×10	LP mode	Ref[29]
MC-SMF	6020	QPSK	6.144	8	8×8	Fundamental mode	Ref[30]
FMF	3	16-QAM	0.448	4	4×4	Vector mode	Ref[31]
MMF	26.5	QPSK 16-QAM	101	90	90×90	LP mode	Ref[18]
MMF	23	64-QAM	1010	30	30×30	LP mode	Ref[19]

Table 1.3: Representative partial-MIMO SDM-based transmission systems in recent works.

Fiber type	Distance (km)	Modulation format	Total capacity (Tbits^{-1})	Number of spatial channels	MIMO DSP	Mode basis	Refs
RCF	100	QPSK	2.56	8	4×4	OAM mode	Ref[21]
FMF	3	16-QAM	0.224	4	2×2	Vector mode	Ref[32]
FMF	48	QPSK	257	20	2×2 4×4	LP mode	Ref[33]
FMF	48	PS-16QAM	402.7	20	2×2 4×4	LP mode	Ref[17]
MC-RCF	34	QPSK	1223	80	4×4	OAM mode	Ref[34]

Table 1.4: Representative MIMO-free SDM-based transmission systems in recent works.

Fiber type	Distance (km)	Modulation format	Total capacity (Gbits^{-1})	Number of spatial channels	MIMO basis	Refs
FMF	10	OOK	40	4	LP mode	Ref[35]
ACF	1.2	QPSK	14400	12	OAM mode	Ref[36]
RCF	50	OOK	15	2	OAM mode	Ref[37]
ERCF	0.9	QPSK	384	6	LPV mode	Ref[38]
MMF	2.6	QPSK	40	2	OAM mode	Ref[39]

1.2 Scalar mode and Vector mode

For MDM fiber transmission systems, orthogonality of specific spatial modes effectively assists multiplex multiple co-propagating signals. In general, all the eigenmodes that a given fiber can support form a set of orthogonal bases. Arbitrary light fields existing in this given fiber could be viewed as the linear superposition of this set of orthogonal bases. Actually, various types of modal basis sets have been employed as orthogonal channels in MDM systems, which could be divided into two main categories: vector mode based on the exact analytic expression for the theory of optical fibers and scalar mode based on the simplified analytic expression for the theory of optical fibers.

Vector modes can be regarded as the true waveguide modes of fiber, which are the rigorous solutions for Maxwell's equations. The typical feature of VMs is polarization distribution, which is tailored in a unique way and such advanced polarization tailoring provides a complete orthogonality. Here, the exact optical fiber theory based on vector mode is first introduced. In cylindrical coordinate system, the electric **E** and magnetic

H fields can be calculated as,

$$\begin{cases} \mathbf{E} = E_r \hat{e}_r + E_\varphi \hat{e}_\varphi + E_z \hat{e}_z \\ \mathbf{H} = H_r \hat{e}_r + H_\varphi \hat{e}_\varphi + H_z \hat{e}_z \end{cases} \tag{1.1}$$

where (E_r, E_φ, E_z) and (H_r, H_φ, H_z) denote the electric and magnetic fields in radial $\hat{e}_r$, angular $\hat{e}_\varphi$ and axial $\hat{e}_z$ directions, respectively. According to Maxwell's equations[40], the wave equations can be written as,

$$\begin{cases} \frac{\partial^2 E_z}{\partial r^2} + \frac{1}{r}\frac{\partial E_z}{\partial r} + \frac{1}{r^2}\frac{\partial^2 E_z}{\partial \varphi^2} + \left[k^2 n(r)^2 - \beta^2\right] E_z = 0 \\ \frac{\partial^2 H_z}{\partial r^2} + \frac{1}{r}\frac{\partial H_z}{\partial r} + \frac{1}{r^2}\frac{\partial^2 H_z}{\partial \varphi^2} + \left[k^2 n(r)^2 - \beta^2\right] H_z = 0 \end{cases} \tag{1.2}$$

where $k = \frac{2\pi}{\lambda}$ denotes the wave number and β denotes the propagation constant for the waveguide mode. $n(r)$ represents the refractive index profile of the cross-section of the fiber. Basically, transverse electrical and magnetic fields can be further calculated as

$$\begin{cases} E_r = -\frac{j}{[k^2 n(r)^2 - \beta^2]} \left(\beta \frac{\partial E_z}{\partial r} + \frac{\omega \mu_0}{r}\frac{\partial H_z}{\partial \varphi}\right) \\ E_\varphi = -\frac{j}{[k^2 n(r)^2 - \beta^2]} \left(\frac{\beta}{r}\frac{\partial E_z}{\partial \varphi} - \omega \mu_0 \frac{\partial H_z}{\partial r}\right) \\ H_r = -\frac{j}{[k^2 n(r)^2 - \beta^2]} \left(\beta \frac{\partial H_z}{\partial r} + \frac{\omega \varepsilon_0 n(r)^2}{r}\frac{\partial E_z}{\partial \varphi}\right) \\ H_\varphi = -\frac{j}{[k^2 n(r)^2 - \beta^2]} \left(\frac{\beta}{r}\frac{\partial H_z}{\partial \varphi} + \omega \varepsilon_0 n(r)^2 \frac{\partial E_z}{\partial r}\right) \end{cases} \tag{1.3}$$

Here, ε_0 and μ_0 respectively denote the permittivity and permeability of the vacuum. ω is the angular frequency. Since the structure of the optical fiber is generally circularly symmetrical distribution, the optical field confined in the fiber also follows the circularly symmetrical distribution. Accordingly, it is convenient to introduce $\cos(l\varphi)$ and $\sin(l\varphi)$ to describe the optical field in the fiber (l is the azimuthal order and φ is the azimuthal angle on the traverse plane). The electrical and magnetic fields can be rewritten as,

$$\begin{cases} E = F(r) \begin{pmatrix} \cos(l\varphi) \\ \sin(l\varphi) \end{pmatrix} \exp(j\beta z) \\ H = G(r) \begin{pmatrix} \cos(l\varphi) \\ \sin(l\varphi) \end{pmatrix} \exp(j\beta z) \end{cases} \tag{1.4}$$

where $F(r)$ and $G(r)$ respectively represent the radial field distribution of electric and magnetic fields, which are related to the Bessel equation. Specifically, the forms of the optical field are slightly different for different structures of fiber. Next, the step-index fiber, as a typical optical fiber, is taken as an example to illustrate the basic characteristics of light waves in the fiber. The index profile of a step-index fiber with core diameter $2a$ can be described as follows,

$$n(r) = \begin{cases} n_1 & r \leq a \\ n_2 & r > a \end{cases} \tag{1.5}$$

where n_1 and n_2 respectively denote the refractive index of core and cladding. Based on Eq.(1.2), Eq.(1.5) and the boundary condition in the fiber, the longitudinal electric and magnetic field components can be given,

$$E_z = \begin{cases} AJ_l\left(\frac{U}{a}r\right)\cos(l\varphi) & (0 \leq r \leq a) \\ A\frac{J_(lU)}{K_l(W)}K_l\left(\frac{W}{a}r\right)\cos(l\varphi) & (r > a) \end{cases} \tag{1.6}$$

$$H_z = \begin{cases} BJ_l\left(\frac{U}{a}r\right)\sin(l\varphi) & (0 \leq r \leq a) \\ B\frac{J_l(U)}{K_l(W)}K_l\left(\frac{W}{a}r\right)\sin(l\varphi) & (r > a) \end{cases} \tag{1.7}$$

Substituting Eq.(1.6) and Eq.(1.7) into Eq.(1.3), the transverse electric and magnetic field components can be obtained by Bessel-type functions,

$$E_r = \begin{cases} -j\left(\frac{a}{U}\right)^2\left[A\beta\frac{U}{a}J_l'\left(\frac{U}{a}r\right) + B\omega\mu_0\frac{l}{r}J_l\left(\frac{U}{a}r\right)\right]\cos(l\varphi) & (0 \leq r \leq a) \\ j\left(\frac{a}{\mathrm{W}}\right)^2\left[A\beta\frac{\mathrm{W}}{a}K_l'\left(\frac{W}{a}r\right) + B\omega\mu_0\frac{l}{r}K_l\left(\frac{W}{a}r\right)\right]\frac{J_l(U)}{K_l(W)}\cos(l\varphi) & (r > a) \end{cases} \tag{1.8}$$

$$E_\varphi = \begin{cases} -j\left(\frac{a}{U}\right)^2\left[-A\beta\frac{l}{r}J_l\left(\frac{U}{a}r\right) - B\omega\mu_0\frac{U}{a}J_l'\left(\frac{U}{a}r\right)\right]\sin(l\varphi) & (0 \leq r \leq a) \\ j\left(\frac{a}{\mathrm{W}}\right)^2\left[-A\beta\frac{l}{r}K_l\left(\frac{W}{a}r\right) - B\omega\mu_0\frac{W}{a}K_l'\left(\frac{W}{a}r\right)\right]\frac{J_l(U)}{K_l(W)}\sin(l\varphi) & (r > a) \end{cases} \tag{1.9}$$

$$H_r = \begin{cases} -j\left(\frac{a}{U}\right)^2 \left[A\omega\varepsilon_0 n_1^2 \frac{l}{r} J_l\left(\frac{U}{a}r\right) + B\beta\frac{U}{a} J_l'\left(\frac{U}{a}r\right)\right] \sin(l\varphi) & (0 \leq r \leq a) \\ j\left(\frac{a}{\mathrm{W}}\right)^2 \left[A\omega\varepsilon_0 n_2^2 \frac{l}{r} K_l\left(\frac{W}{a}r\right) + B\beta\frac{W}{a} K_l'\left(\frac{W}{a}r\right)\right] \frac{J_l(U)}{K_l(W)} \sin(l\varphi) & (r > a) \end{cases} \tag{1.10}$$

$$H_\varphi = \begin{cases} -j\left(\frac{a}{U}\right)^2 \left[A\omega\varepsilon_0 n_1^2 \frac{U}{a} J_l'\left(\frac{U}{a}r\right) + B\beta\frac{n}{r} J_l\left(\frac{U}{a}r\right)\right] \cos(l\varphi) & (0 \leq r \leq a) \\ j\left(\frac{a}{\mathrm{W}}\right)^2 \left[A\omega\varepsilon_0 n_2^2 \frac{W}{a} K_l'\left(\frac{W}{a}r\right) + B\beta\frac{m}{r} K_l\left(\frac{W}{a}r\right)\right] \frac{J_l(U)}{K_l(W)} \cos(l\varphi) & (r > a) \end{cases} \tag{1.11}$$

Here, $J_l(x)$ and $K_l(x)$ are the first Bessel function and the second Bessel function, respectively. The constant parameters U and W of transverse optical fields are calculated using the following equations,

$$U = a\sqrt{k^2 n_1^2 - \beta^2} \tag{1.12}$$

$$W = a\sqrt{\beta^2 - k^2 n_2^2} \tag{1.13}$$

where U and W respectively represent the lateral oscillation frequency in the core region and the attenuation speed of the optical field in the cladding region. In addition, normalized frequency V determining the number of supported modes in the fiber is related to parameters U and W, which can be obtained as follows,

$$V^2 = U^2 + W^2 = a^2 k^2 (n_1^2 - n_2^2). \tag{1.14}$$

A and B are constants and obey the following relation,

$$B = -A\frac{\beta}{\omega\mu_0} \frac{m\left(\frac{1}{U^2} + \frac{1}{W^2}\right)}{\left[\frac{J_n'(U)}{UJ_m(U)} + \frac{K_n'(W)}{WK_m(W)}\right]}. \tag{1.15}$$

For a given fiber of specific parameters, a series of propagation constants $\beta_1, \beta_2, \beta_3 ... \beta_N$ can be obtained based on the above derivation. Each propagation constant β_i corresponds to a specific electromagnetic field distribution (except for even and odd modes of hybrid modes, which is defined as fiber eigenmode. According to the distribution characteristic, the electromagnetic fields are divided into four types: TE, TM, HE and EH modes. TE mode is the transverse electric mode with no electric field ($E_z = 0$) along the direction of propagation. TM mode is the transverse magnetic mode with no magnetic field ($H_z = 0$) along the direction of propagation. When $E_z \neq 0$ and $H_z \neq 0$, both electric and magnetic fields have the component along the propagation direction and the electromagnetic fields are viewed as hybrid modes, denoted as EH and HE modes. Each EH/HE mode also includes even mode and odd mode with a $\frac{\pi}{2}$ azimuthal rotation. Since all four types of optical fields manifest polarization distribution, such fiber eigenmodes are also called vector mode.

Compare to vector modes, scalar modes are derived by the weakly guiding approximation in the optical fiber, where the refractive index difference between the core and the cladding is extremely small and can be neglected. Namely, the refractive index of the core and cladding need to satisfy the following condition:

$$\Delta = \frac{n_1^2 - n_2^2}{2n_1^2} \approx \frac{n_1 - n_2}{n_1} \approx \frac{n_1 - n_2}{n_2} \ll 1. \tag{1.16}$$

Here, the full vectorial wave equation could be further simplified to a scalar wave equation and the guiding wave in the fiber is very close to the form of TEM mode where neither electric nor magnetic field has a component under such weakly guiding condition. Accordingly, the scalar mode in the fiber can be uniformly described as the linearly polarized (LP) mode which is the most commonly used. Different from vector mode with spatial variant state of polarization (SoP), LP mode only has two orthogonal linear SoPs. In the Cartesian coordinate system, the transverse electric field can be written as,

$$\mathbf{E_t} = E_x \hat{e}_x + E_y \hat{e}_y. \tag{1.17}$$

When an appropriate coordinate is chosen, only one component of the electric field exists, which can be described as follows,

$$\mathbf{E_t} = E_x \hat{e}_x. \tag{1.18}$$

Substituting this expression into the wave equation, the electric and magnetic fields corresponding to X-polarization can be respectively obtained as follows,

$$\begin{cases} E_x = \frac{A}{J_l(U)} J_l\left(\frac{U}{a}r\right) \begin{Bmatrix} \cos(l\varphi) \\ \sin(l\varphi) \end{Bmatrix} & 0 \leq r \leq a \\ E_x = \frac{A}{K_l(W)} K_l\left(\frac{W}{a}r\right) \begin{Bmatrix} \cos(l\varphi) \\ \sin(l\varphi) \end{Bmatrix} & r > a \end{cases} \tag{1.19}$$

$$\begin{cases} H_x = -\sqrt{\frac{\varepsilon_0}{u_0}} \frac{An_1}{J_l(U)} J_l\left(\frac{U}{a}r\right) \begin{Bmatrix} \cos(l\varphi) \\ \sin(l\varphi) \end{Bmatrix} & 0 \leq r \leq a \\ H_x = -\sqrt{\frac{\varepsilon_0}{u_0}} \frac{An_2}{K_l(W)} K_l\left(\frac{W}{a}r\right) \begin{Bmatrix} \cos(l\varphi) \\ \sin(l\varphi) \end{Bmatrix} & r > a \end{cases} \tag{1.20}$$

Likewise, when $\mathbf{E_t} = E_y \hat{e}_y$, another set of solutions corresponding to Y-polarization can be obtained and β, U and W for each scalar mode also needs to be solved based on the same derivation. In the weakly guiding regime, there is a certain relationship between vector mode and LP mode according to the propagation constant β of each mode, which is listed in Table 1.5 (l and m represent azimuthal and radial order of modes, respectively).

Table 1.5: The relationship between LP and vector mode.

$\ell = 0, m \geq 1$	$\mathrm{LP_{0,m}}$	$HE^e_{1,m}$, $HE^o_{1,m}$
$\ell = 1, m \geq 1$	$\mathrm{LP_{1,m}}$	$TM_{0,m}$, $TE_{0,m}$, $HE^e_{2,m}$, $HE^o_{2,m}$
$\ell > 1, m \geq 1$	$\mathrm{LP_{\ell,m}}$	$HE^e_{(l+1),m}$, $HE^o_{(l+1),m}$, $EH^e_{(l-1),m}$, $EH^o_{(l-1),m}$

Actually, as the eigenmode of fiber, VM with spatially inhomogeneous SoP has lately attracted much attention for its intrinsic characteristics. Any other type of basis sets of fiber modes could be identified as the coherent superposition of a set of vector eigenmodes. Besides, to further suppress mode crosstalk between/among MGs, specially-designed fibers that can stably guide eigenmodes have been widely investigated, such as ring-core fibers with circular symmetry[41,42]. Integrated optical vortex emitter, mode converter and mode multiplexer/de-multiplexer for fiber eigenmodes have also attracted lots of attention lately[42–44]. Thus, fiber eigenmode-based MDM transmission deserves more investigation and consideration.

1.3 Challenges to SDM/MDM optical fiber Short-Haul Transmissions

Short-reach optical interconnects, such as data center interconnect (DCI), are important components in the infrastructure to support massive Internet applications based on data centers. In order to enable optical interconnects to develop into economically feasible solutions in practical short-distance transmission, both the cost and operational complexity of the transmission link need to be minimized while better and faster performance is guaranteed. SDM/MDM scheme, as an appealing technology to considerably upsurge the capacity of optical transmission system, has enormous potential to break the capacity crunch of SMF-based systems and further alleviate the bandwidth requirement. Moreover, from the point of view of communication networks, when assessing the viability of SDM/MDM-based systems, a wide array of key factors need to be considered, including the cost per bit, power consumption, compatibility with the mainstream communication technologies, reliability of systems and computational complexity of DSP. However, several current constraints limit the use of SDM/MDM techniques in practical short-reach systems to meet the ever-increasing traffic demand. Here, the main challenges for SDM/MDM short-haul fiber systems are discussed as follows:

A: How to increase the transmission data rate per fiber?

Theoretically, the transmission capacity is determined by density in an amount proportional to the number of co-transmitted channels. SDM scheme indeed offers a new

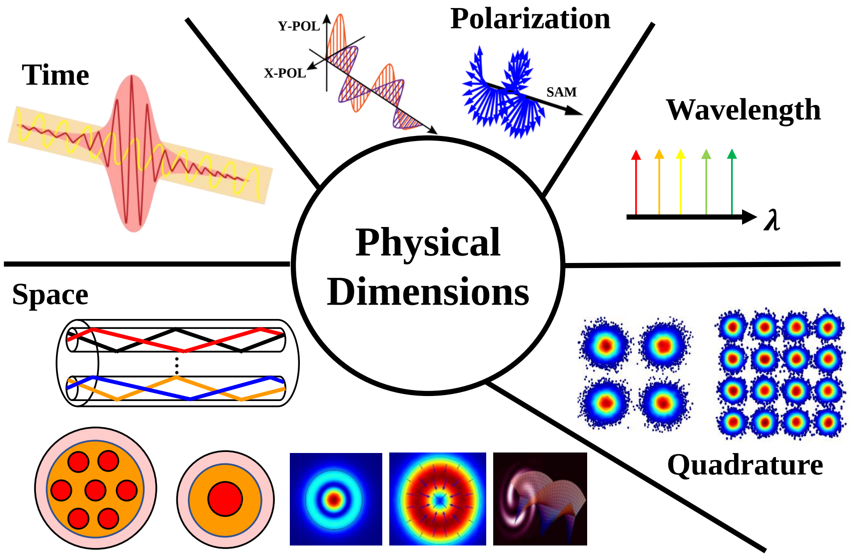

Figure 1.4: Different physical dimensions for modulation and multiplexing.

degree of freedom (DoF) to stretch the capacity of communication links in addition to time, wavelength, polarization and phase dimensions which have been successfully carried out in commercial systems. To keep pace with the actual traffic demand in the near future, SDM scheme needs to be compatible with the existing mature technologies, such as wavelength division multiplexing (WDM), time division multiplexing (TDM) and advanced modulation format, because hybrid network architectures are most likely to fully upgrade optical communication transmission. Accordingly, optimizing the allocation of these physical dimension resources (shown in Fig.**1.4**) is of great importance.

B: How to decrease the cost and increase the efficiency of the transmission system?

Potentially, SDM/MDM scheme can remarkably enlarge the capacity of optical systems in an amount proportional to the number of co-transmitted spatial channels without extra bandwidth resources. Compared to WDM scheme, SDM/MDM might be deemed more suitable for short-reach links in terms of size and cost of the system. However, modal crosstalk caused by mode-coupling in fiber transmission is a major barrier to infinitely increasing mode channel counts[45]. To address this concern, coherent detection in conjunction with MIMO DSP is frequently resorted to compensate the signal impairment, which will definitely induce prohibitive costs, high power consumption and huge computational complexity[46,47]. For short-reach transmission systems, low cost, energy efficiency, and simple implementation are critical considerations. SDM/MDM scenarios must not only scale up the capacity but also minimize the cost- and energy-per-bit when involved in short-reach links. Thus, achieving a high-capacity as well as low-cost SDM/MDM system is still a long-standing challenge.

C: How to guarantee the reliability and robustness of SDM/MDM-based systems?

The dependability and stability of SDM/MDM structure are of great significance as well, especially when it is applied in field experiments and commercial networks, which requires that SDM/MDM-based system possesses the good capability of anti-jamming. Whenever and wherever stable polarization-/mode-independent performance is highly pursued. Up to now, most experimental demonstrations of SDM/MDM links are implemented in labs with a stable environment and the performance of SDM/MDM links in the practical deployment deserves further testing and evaluation. After all, future communication networks are expected to be more reliable and robust.

1.4 Research Objectives and Organization of the Thesis

1.4.1 Research Objectives

The research aims and objectives conducted in the thesis are to develop short-reach MDM fiber links based on direct vector eigenmodes and extend the available trade-off between transmission performance and the size of such systems, so as to improve the resilience and usability of VM-based MDM systems. More particularly, the thesis focuses on the following main issues:

A: Only vector modes strictly obey Maxwell's equations when traveling through the optical fiber, which indicates that vector mode is the one and only direct, orthogonal and comprehensive modal set for fiber transmission. The characteristic features and implications of using true vector eigenmodes in fiber transmission is first investigated and analyzed based on the higher-order Poincaré sphere framework.

B: Based on direct fiber vector eigenmodes multiplexing technology, two main types of short-reach transmissions, including uni-directional and bi- directional links are experimentally investigated, demonstrated and evaluated. In addition, multi-dimensional hybrid WDM-PDM-MDM systems are also conducted for capacity boost.

C: Practical usage of proposed VM-based MDM scenarios is investigated. For practical or commercial applications, apart from total capacity and cost per bit, robust and reliable performance is equally important. The research shall focus on minimizing the performance fluctuation of such MDM systems during the dynamic performance evaluation.

1.4.2 Organization of the Thesis

There are 5 chapters in this thesis.

In Chapter 1, the thesis starts with the background and the development of SDM/MDM technology. Next, two typical modal sets including scalar mode and vector mode for MDM fiber transmission scenarios are elaborated in detail. Though the capacity boost of the communication systems could be realized by this technology, this research field still encounters serious challenges, especially for practical applications of SDM/MDM technology. In the end, the research objectives and organization of this thesis are listed.

In Chapter 2, the transmission performance of vector mode through free-space optical transmission is investigated and discussed, including the degree of divergence and the impact of atmospheric turbulence. Based on the higher-order Poincare sphere framework, the typical features of vector mode are presented. Moreover, the relationship between SoPs including homogeneous and non-homogeneous SoPs and optical angular momentum including spin angular momentum and orbital angular momentum is also established and is further demonstrated and analyzed by experimental studies.

In Chapter 3, in order to characterize the potential of fiber eigenmode-based MDM systems, two types of short-reach fiber links: uni-directional and bi- directional transmission systems are studied. For uni-directional link, MIMO-free MDM transmission over anti-resonant hollow core fiber and step-index FMF are respectively demonstrated and analyzed. For bi-directional link, two full-duplex structures including homo-modal and hetero-modal transmissions based on dual-VMs multiplexing over 3 km FMF are proposed and implemented. In tandem with WDM technology, A total capacity of 1.792 Tbit/s link with 28 GBaud 16-quadrature amplitude modulation (16-QAM) signal over each channel is successfully realized over the 3 km FMF.

Chapter 4 extends to focus on the practicality and robustness of the short-reach MDM systems. First, a simple but versatile scheme of MG filter for mode-group-division multiplexing intensity-modulated direct-detection transmission is proposed and experimentally demonstrated. This scheme applies to any mode basis in the fiber, and it also satisfies the needs of low complexity, low power consumption, and high system performance. By employing the proposed MG filter scheme, a 152 Gbit/s MIMO-free IM/DD co-channel simultaneous transmit and receive system based on two orbital angular momentum (OAM) MGs, each carrying 38-GBaud four-level pulse amplitude modulation (PAM-4) signal, is experimentally demonstrated over 5 km FMF. Both static and dynamic performance evaluation confirm the practicality and stability of this proposed MGDM scheme. Next, based on Kramers–Kronig Reception and 4 $\times$ 4 non-Singular MIMO DSP, a 448 Gbit/s four-VMs-multiplexing link, each mode carrying 28-GBaud 16-QAM signal is experimentally demonstrated over 3 km FMF. To confirm the real availability of this system, 7408 signal sets including 598 static sets and 13-hour 6,810 dynamic sets are tested and none of the singularities is observed. The experimental results fully highlight that this VM-based MDM scheme could find great scope for development in high-speed short-reach networks.

Finally, Chapter 5 summarizes the research contributions contained in the thesis and then discusses potential future works of this research field.

2

Vector mode characterization in FSO and FMF propagation

In this chapter, the transmission performance of VM-based MDM free space optical link under atmospheric turbulence is evaluated and discussed. Then, the main characterizations of vector mode based on the high-order Poincaré sphere are introduced. Finally, the performance of VMs propagated in FMF is characterized based on high-order Poincaré sphere analysis.

2.1 Performance of CVB-based MDM FSO Link under Atmospheric Turbulence using 4×4 Non-Singular MIMO

2.1.1 Introduction

In recent years, free space optical (FSO) communications where free space is a transport medium between transmitter and receiver have drawn great attention due to its advantages of the unlicensed broad optical spectrum, large bandwidth potential, low power consumption and flexibility in setting up the communication link. The ever-increasing bandwidth demands have also urged more complex modulation formats to be deployed in FSO communication systems. However, the performance of FSO transmission link is inevitably affected by the atmospheric turbulence (AT) in the air[48]. When the beam travels in the atmosphere, Refractive index fluctuations caused by AT can destroy the coherence of the light field and lead to random changes in the transmitted light field, thereby affecting the transmission quality of the beam. In FSO communication link, the fluctuations caused by AT will influence the intensity and phase of the light signal, which definitely degrades the link performance, especially in long-distance FSO transmission and high AT conditions. Moreover, some other factors will also affect the transmission performance of FSO link. First, due to optical diffraction in free space, the transmission distance will be limited to some extent. In addition, beam diffraction can cause signal attenuation at the receiver, which may affect the performance of the transmission. The beam size is also a key factor because it is related to the Rayleigh range within which the performance of FSO transmission is relatively good.

To keep up with the exponentially growing demand for high-capacity transmission, multiplexing technologies by employing different physical dimensions including wavelength, polarization, amplitude and phase have been implemented in FSO link. Currently, MDM schemes have also been implemented in FSO link as well[49,50]. According to the existing reports, the influence of AT on vector beams is relatively weak compared with its effect on scalar beams. This indicates that cylindrical vector beams (CVBs) with spatially variant SoP distribution have enormous potential in FSO communication link and deserve more investigation[51–53]. On the other hand, compared to the fundamental mode, the divergence of CVBs with doughnut-like intensity is more serious. Thus, it is worth investigating which type of beam is more suitable for FSO system.

In this chapter, by using Kramers–Kronig (KK) reception and 4×4 non-singular MIMO algorithm (4×4 multi-user constant modulus algorithm (MU-CMA)), VM-based MDM FSO link under different atmospheric turbulence conditions is experimentally demonstrated. Performance of averaged bit error rate (BER) of four VMs, each carrying 28-GBaud 16-QAM signals, is evaluated and discussed.

2.1.2 Experimental setups

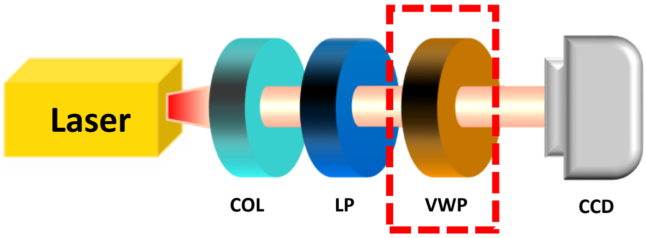

Figure 2.1: Experimental setup for evaluating the divergence of VM. COL: collimator; LP: linear polarizer; VWP: vortex wave plate; CCD: charge-coupled device camera.

In order to properly implement VM-based MDM FSO link, the divergence of VM is first evaluated, shown in Fig.2.1. The continuous wave (CW) light-wave from the optical laser (1550.12 nm) is collimated first. After passing through a linear polarizer and vortex wave plate (VWP), linearly polarized fundamental mode/vector mode is generated. Then, the patterns of these two kinds of modes are captured by charge-coupled device camera (CCD) at different propagated distances, which are shown in Fig.2.2 and Fig.2.3, respectively. For the demonstration, the radius of the collimated beam of the collimator used is approximated 1.05 mm which is regarded as the initial beam size. Finally, the beam sizes of these two kinds of modes are estimated according to the captured profiles, which is illustrated in Fig.2.4. As can be seen from these figures, the estimated beam size of both modes becomes larger with a longer transmission distance. Furthermore, compared to the linearly polarized fundamental mode, the donut-shaped vector mode obviously diverges faster.

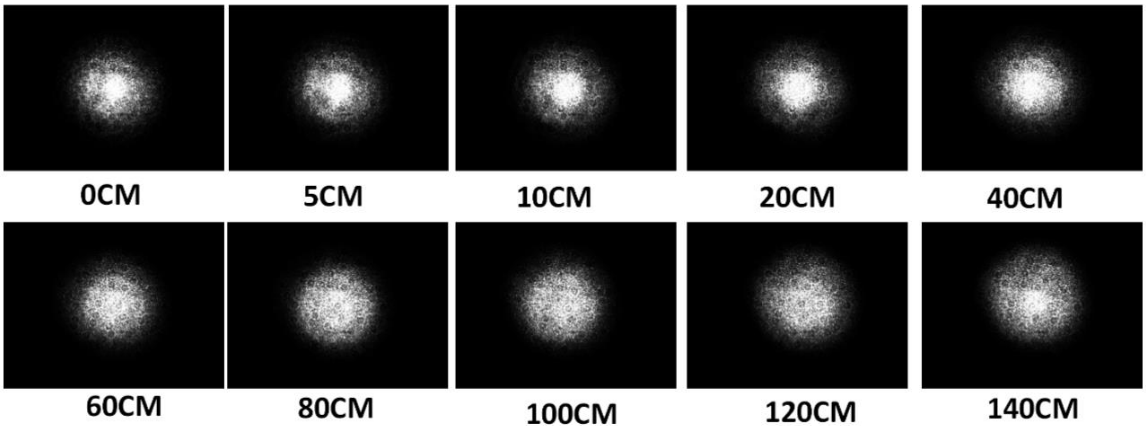

Figure 2.2: The captured intensity profiles of fundamental mode propagated at different distances.

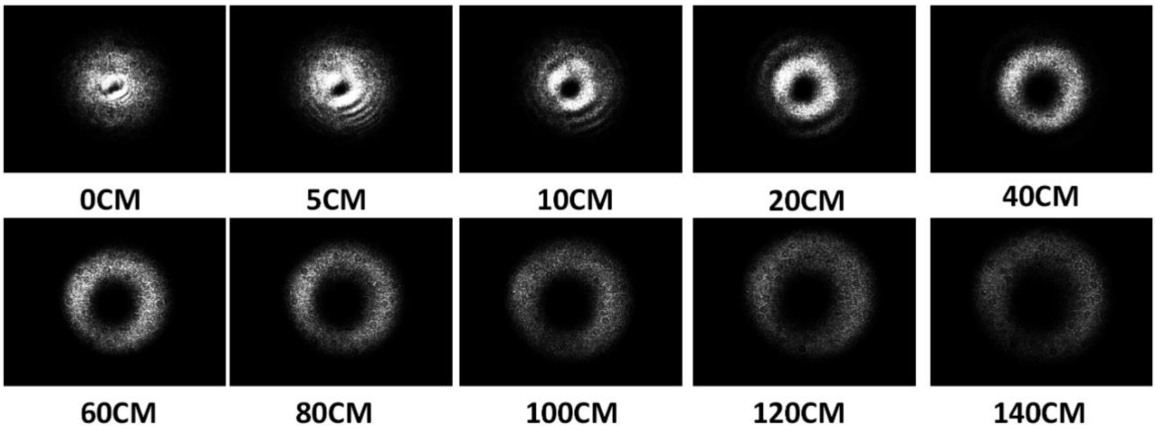

Figure 2.3: The captured intensity profiles of vector mode propagated at different distances.

To properly detect and demultiplex the vector mode, which becomes prohibitively larger with increased link distance, a matching receive aperture is needed at the receiver. Moreover, according to Ref[54], eigenmode based MDM FSO transmission is relatively viable only when the distance is within the Rayleigh range d_R, which is determined by the radius of the beam waist and the wavelength,

$$d_R = \frac{\pi w_0^2}{\lambda} \tag{2.1}$$

where the w_0 corresponds to the radius of the vector mode at beam waist and the λ corresponds to the wavelength of the optical carrier. Thus, the Rayleigh range in

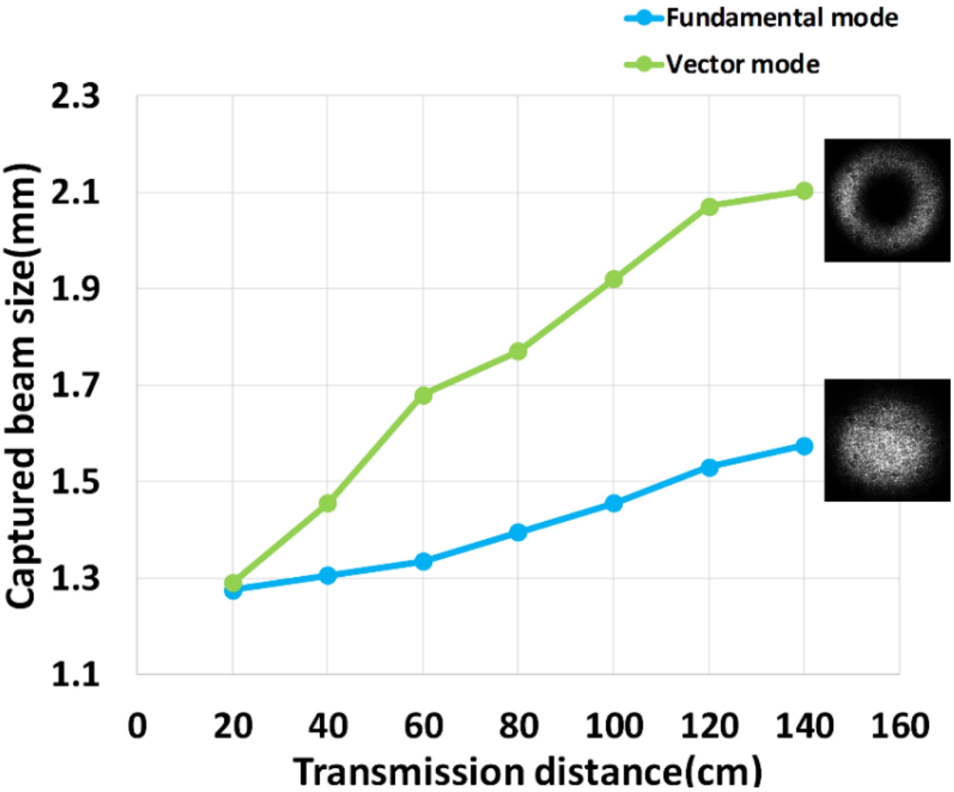

Figure 2.4: The estimated beam size of two kinds of modes propagated at different distances.

our experiment is 2.2 m ($\boldsymbol{d}_R = \pi \times (1.05 \text{ mm} \times 1.05 \text{ mm})/1.55\mu\text{m} \approx 2.2$ m). It can be deduced that the beam size is an impact factor for the transmission distance of FSO link and the transmission distance can be extended when a larger-size beam is adopted. In view of the Rayleigh range and the experimental conditions in the lab, the transmission distance is set to 80 cm in the following FSO transmission experiment.

Figure 2.5 illustrates the experimental setup of four CV modes of $|l| = 2$ multiplexing-based FSO link under three experimental conditions of atmospheric turbulence. At the transmitter, the lightwave from the external cavity laser (ECL, 1550.12 nm) is launched into the in-phase/quadrature modulator (I/Q modulator) and modulated with 28-GBaud 16-QAM signals. Then, polarization-division multiplexing (PDM) is emulated by a polarization beam splitter (PBS) and polarization beam combiner (PBC). Afterwards, the dual-polarization (DP) signals are amplified by an EDFA and divided into two branches. At the CVB-based MDM FSO transmission part, one branch is converted to CV mode of $l = +2$ by a VWP and another is converted to CV mode

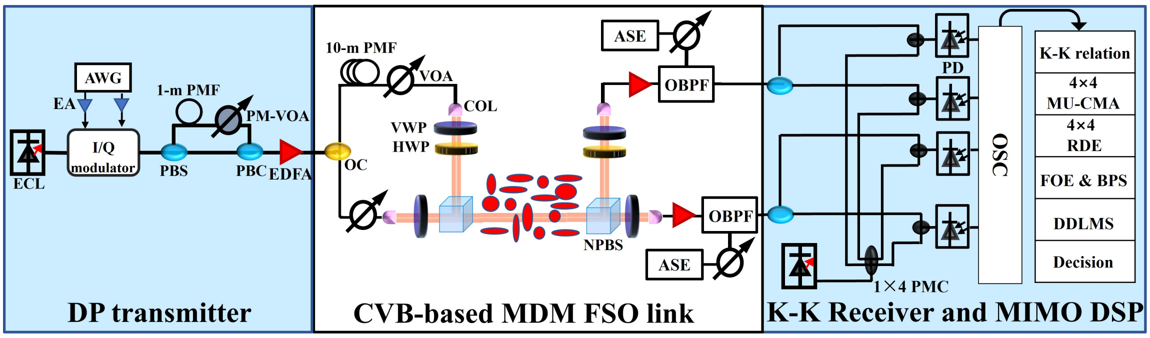

Figure 2.5: Experimental setup of four CV modes of $|l| = 2$ multiplexing-based FSO link under different experimental conditions of atmospheric turbulence. AWG: Arbitrary waveform generator; EA: Electrical amplifier; I/Q Mod.: In-phase/Quadrature modulator; ECL: External cavity laser; PBS: Polarization beam splitter; PMF: Polarization maintaining fiber; PM-VOA: Polarization maintaining variable optical attenuator; PBC: Polarization beam combiner; EDFA: Erbium-doped fiber amplifier; OC: Optical coupler; VOA: Variable optical attenuator; Col: Collimator; VWP: Vortex wave plate; HWP: Half-wave plate; NPBS: Non-polarizing beam splitter; OBPF: Optical bandpass filter; ASE: Amplified spontaneous emission source; PMC: Polarization maintaining coupler; PD: Photodetector; OSC: Oscilloscope.

of $l = -2$ by a VWP cascaded with a half-wave plate (HWP). These four modes are combined by a non-polarizing beam splitter (NPBS). During 80 cm FSO transmission (assuming transmission path of light beams along Z direction), three AT conditions including normal lab environment without any air disturbance (Case 1), hot air flow from X direction (surface temperature of heater: 300°C) (Case 2), hot air flow from X (surface temperature of heater: 300°C) and Y direction (surface temperature of heater: 200°C) (Case 3) are respectively prepared for this experiment. After FSO link, the light beam is divided into two branches by NPBS. One branch passes through a VWP and only CV modes of $l = +2$ are demodulated, while only CV modes of $l = -2$ of another branch are converted to fundamental modes after HWP and VWP. Then, these two branches are respectively coupled into SMF for KK receiver. The local oscillator (LO) whose polarization is the same as the received signal has a frequency offset of 28-GHz×(1+0.1)/2 compared to the lightwave at the transmitter and the carrier-to-signal power ratio (CSPR) is set to 12 dB to fulfill the requirement of KK reception. Finally, the signals are detected by four photodetectors (PDs) and then sampled by a real-time oscilloscope (OSC) and processed by offline DSP (including KK reception and equalization of 4×4 MU-CMA and RDE[55]).

2.1.3 Experimental results

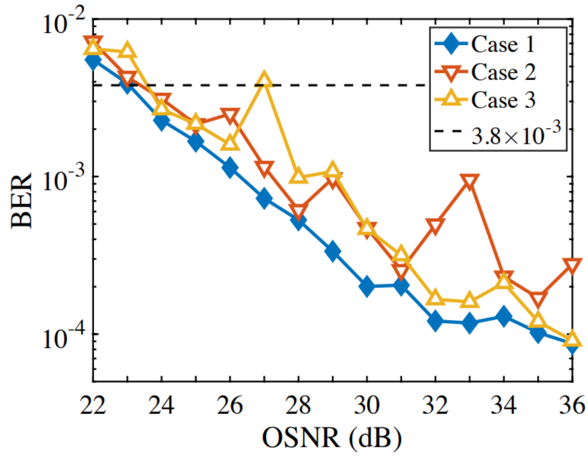

Figure 2.6: Averaged BERs of four CV modes versus OSNR under three AT conditions including normal lab environment without any air disturb (case I), hot air flow from X direction (case II) and hot air flow from X and Y direction (case III).

The averaged BERs for all four modes under different optical signal-to-noise ratio (OSNR) of all three AT cases are shown in Fig.2.6. With existing AT, the used $|l| = 2$ mode group can be transferred to other mode groups and then the crosstalks from other mode groups are induced. It can be seen that BERs of Case 2 and Case 3 fluctuate and degrade. Besides, AT can affect the mode coupling within one mode group. Here the absolute value of weights over all 16 filters of 4×4 MIMO after equalization are used as the evaluation of mode coupling[55]. The large value of w_{ij} represents the large mode coupling from mode j to i. The weights of all results from Fig.2.6 are depicted in Fig.2.7 (a), (b), and (c), representing Case 1, 2, and 3, respectively.

It's observed that without AT, the mode coupling mainly occurs between signal over polarizations ($w_{ij}|_{i,j=1,2}$, or $w_{ij}|_{i,j=3,4}$) within one CV mode ($l = +2$ or $l = -2$) since each CV mode is converted to fundamental mode and coupled into SMF before K-K reception, where there is random polarization rotation existed in the SMF. With the existing AT for two cases (Case 2 and Case 3), the mode coupling could occur between different CV modes, namely the larger value of weights observed in Fig.2.7 (b) and (c) compared to it in Fig.2.7 (a). Especially in Fig.2.7 (c), it's observed that the maximum values of w_{14} and w_{32} are near 1 and it's possibly resulted by the more complex AT condition.

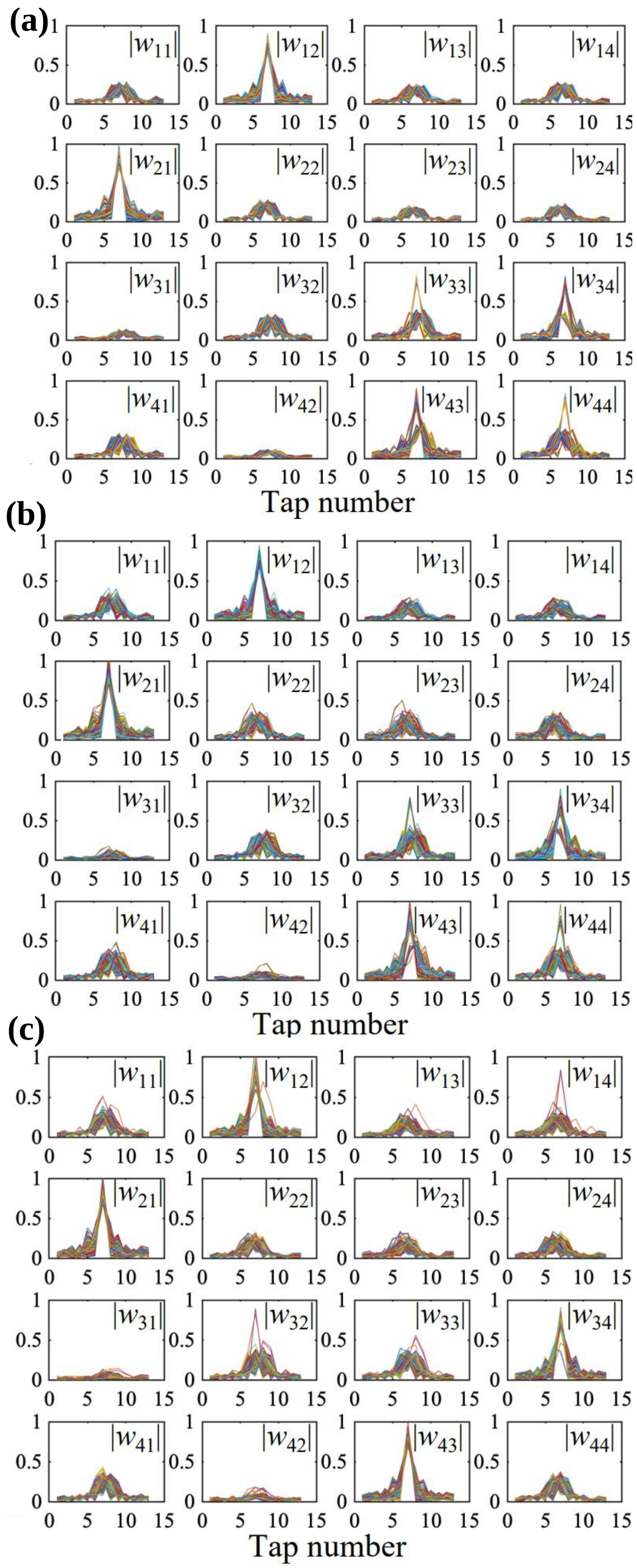

Figure 2.7: Absolute value of weights under (a) Case 1; (b) Case 2; (c) Case 3.

2.2 High-order Poincaré sphere analysis of vector vortex beams

2.2.1 High-order Poincaré sphere model

Structured light field is determined by intrinsic multiple degrees of freedom (DoFs), such as temporal amplitude, state of polarization (SoP), spatial mode, optical phase, wave vector and wavelength[56]. In general, structured light fields can be categorized into two types: separable and nonseparable states[57], see Fig.2.8.

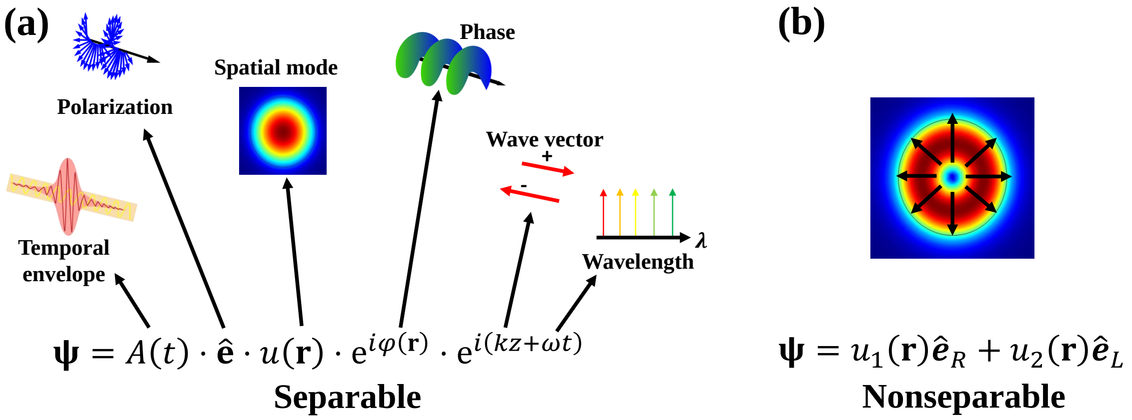

Figure 2.8: (a) Separable and (b) nonseparable light fields.

For the separable state of light, arbitrary DoF can behave independently, see Fig.2.8 (a). This type of light field can be described as,

$$\boldsymbol{\Psi} = A(t) \cdot \hat{\mathbf{e}} \cdot u(\mathbf{r}) \cdot e^{i\varphi(\mathbf{r})} \cdot e^{i(kz+\omega t)}. \tag{2.2}$$

where $A(t)$, $\hat{\mathbf{e}}$, $u(\mathbf{r})$, $e^{i\varphi(\mathbf{r})}$, k and ω denote temporal envelope, polarization, spatial mode, phase, wave vector and wavelength, respectively. As can be seen, each parameter can be factorized as independent factor in the Eq.(2.2). In mathematics, the function is separable if it can be expressed as a product of the certain amount of independent terms, such as the function $F(x, y) = Ag(x)p_1(y)+ Bg(x)p_2(y) = [g(x)] [Ap_1(y) + Bp_2(y)]$ (A and B are constants).

On the contrary, nonseparability indicates that two or more DoFs cannot separately behave in the optical system if and only if it is a whole joint state that can absolutely determine the DoF-dependent characterization. Mathematically, the function

$F(x,y) = Ag_1(x)p_1(y) + Bg_2(x)p_2(y)$ is nonseparable, where g_1 and g_2 (p_1 and p_2) are mutual orthogonal functions, A and B are constants. Moreover, a generalized nonseparable state is expressed as[57],

$$\begin{aligned} |\Psi\rangle =& \sum_{i=1}^{n} \alpha_i \bigotimes_{j=1}^{m} \left| d_j^{(i)} \right\rangle \\ =& \alpha_1 \left| d_1^{(1)} \right\rangle \left| d_2^{(1)} \right\rangle \cdots \left| d_m^{(1)} \right\rangle + \alpha_2 \left| d_1^{(2)} \right\rangle \left| d_2^{(2)} \right\rangle \cdots \left| d_m^{(2)} \right\rangle \\ &+ \cdots + \alpha_n \left| d_1^{(n)} \right\rangle \left| d_2^{(n)} \right\rangle \cdots \left| d_m^{(n)} \right\rangle . \end{aligned} \tag{2.3}$$

Here, the parameters $\alpha_i (i = 1, 2, \ldots, n)$ are non-zero constant terms, the substate $\left| d_j^{(i)} \right\rangle (j = 1, 2, \ldots, m)$ represents the jth DoF (nonseparable in total m DoFs) and each substate $\left| d_j^{(i)} \right\rangle$ can no longer be factorized. Vector beam with nonuniform SoP is a typical nonseparable state of light as its polarization and space DoFs are non-separable, shown in Fig.2.8 (b) and can be expressed as,

$$\boldsymbol{\Psi} = \sqrt{a} u_R(\mathbf{r}) \hat{\mathbf{e}}_R + \sqrt{(1-a)} u_L(\mathbf{r}) \hat{\mathbf{e}}_L \tag{2.4}$$

where the spatial mode dimension is mapped onto a two-dimensional subspace $\{u_R(\mathbf{r}), u_L(\mathbf{r})\}$($u_R(\mathbf{r})$ and $u_L(\mathbf{r})$ are mutual orthogonal). The constant a determines the ratio between fields of $u_R(\mathbf{r})$ and $u_L(\mathbf{r})$ that obey the relation $\int |u_{R,L}|^2 \, r dr d\phi = 1$. $\hat{\mathbf{e}}_R$ and $\hat{\mathbf{e}}_L$ corresponds to left- and right-circular polarizations.

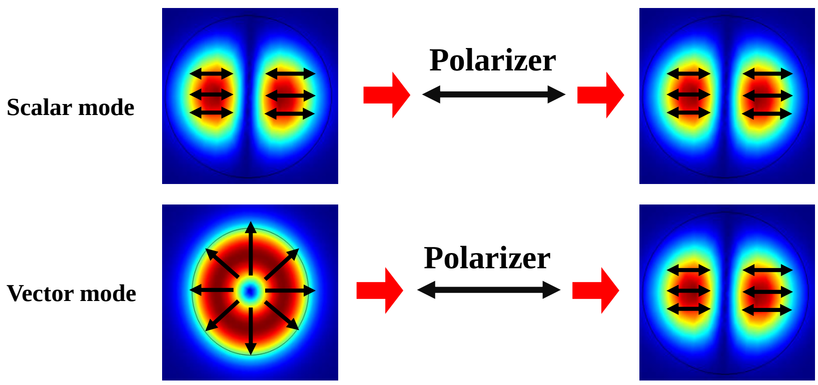

Figure 2.9: Scalar mode and vector mode.

The polarization distribution is an intrinsic property of the electromagnetic field and

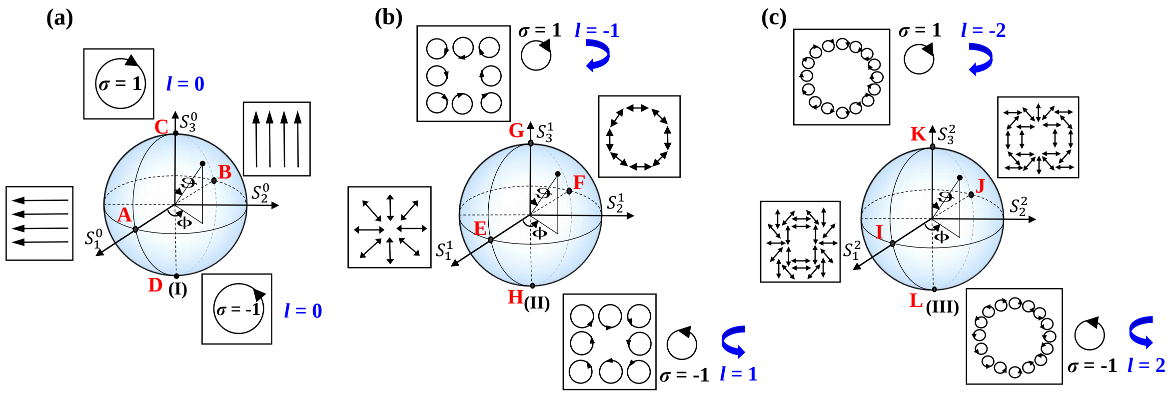

Figure 2.10: Four typical states of polarization on (a) the fundamental Poincaré sphere ($l = 0$), (b) the first-order Poincaré sphere and (c) the second-order Poincaré sphere, respectively.

is also a significant character of light. Compared with spatially uniform polarization of scalar mode, vector modes have the unique characteristic of cylindrical symmetric polarization, as depicted in Fig.2.9. For scalar mode, the spatial pattern will not be changed after passing through the linear polarizer. For vector modes, However, the spatial pattern will change with the rotated polarizer. For example, the donut-shaped vector mode in Fig.2.9 is converted to two petals orientated along the horizontal axis after the polarizer with the transmission orientation of the horizontal axis.

The homogeneous SoP is generally characterized based on two-dimensional Jones vector $\mathbf{E} = (E_x, E_y)$, which only represents completely polarized light. E_x and E_y respectively describe the oscillation amplitude of electric field in the x and y directions. For the orthogonal circular basis, $\begin{pmatrix} E_{\mathrm{R}} \\ E_{\mathrm{L}} \end{pmatrix} = \begin{pmatrix} 1 & \mathrm{i} \\ 1 & -\mathrm{i} \end{pmatrix} \begin{pmatrix} E_x \\ E_y \end{pmatrix}$ and E_R and E_L respectively stand for the amplitude of electric field in the right- and left-circular directions. According to stereographic projection $E_{\mathrm{L}}/E_{\mathrm{R}} = \tan(\theta/2)\exp(\mathrm{i}\phi)$, Poincaré sphere in three-dimensional Stokes space can be obtained, where θ and ϕ are respectively the colatitude and azimuth spherical angles ($0 \leq \theta \leq \pi$ and $0 \leq \phi < 2\pi$). Compared to Jones vector, Poincaré sphere is another powerful prescription to describe SoP, which can represent both completely and partially polarized light. Here, only completely polarized light corresponding to the spherical surface is considered. An arbitrary homogeneous SoP ψ can be geometrically projected as a certain point on the surface of the sphere (Fig.2.10 (a).), which is constructed by the Stokes vector

$\mathbf{S} = (S_1, S_2, S_3)$. These normalized Stokes parameters satisfy $S_0 = S_1^2 + S_2^2 + S_3^2 = 1$ and S_1, S_2, S_3 correspond to X-, Y- and Z-axis, respectively. Here, the normalized Stokes parameters are defined as,

$$S_0 = \frac{I}{I} = \frac{|E_x|^2 + |E_y|^2}{|E_x|^2 + |E_y|^2} = 1 = \frac{|E_R|^2 + |E_L|^2}{|E_R|^2 + |E_L|^2} \tag{2.5}$$

$$S_1 = \frac{I_{0^\circ} - I_{90^\circ}}{I} = \frac{|E_x|^2 - |E_y|^2}{|E_x|^2 + |E_y|^2} = \frac{2Re(E_R^* E_L)}{|E_x|^2 + |E_y|^2} \tag{2.6}$$

$$S_2 = \frac{I_{45^\circ} - I_{135^\circ}}{I} = \frac{E_x^* E_y + E_x E_y^*}{|E_x|^2 + |E_y|^2} = \frac{2Im(E_R^* E_L)}{|E_x|^2 + |E_y|^2} \tag{2.7}$$

$$S_3 = \frac{I_{\mathrm{R}} - I_{\mathrm{L}}}{I} = -\frac{\mathrm{i}\left(E_x^* E_y - E_x E_y^*\right)}{|E_x|^2 + |E_y|^2} = \frac{|E_R|^2 - |E_L|^2}{|E_R|^2 + |E_L|^2} \tag{2.8}$$

where I stands for the total intensity of the beam, I_c stands for the intensity of the beam after passing through the polarizer with the transmission axis of c (I_R/I_L denotes right/left-circular polarizations. According to Fig.**2.10** (a) and Eq.**(2.8)**, linear polarization corresponds to the equator; right- and left-circular polarizations with a spin angular momentum (SAM, $\sigma\hbar$, $\sigma = \pm 1$) correspond to north and south poles, respectively. Except for the equator and two poles, all other points on the spherical surface correspond to elliptical polarizations. Apart from SAM, light beam can also possess higher dimensional angular momentum (AM): OAM, $l\hbar$, $l = \pm 1, \pm 2, \pm 3$,...) with the topological charge l of helical phase, described by Hilbert factor $\exp(il\varphi)$. $\varphi = \arctan(y/x)$ is referred as the azimuthal angle. Thus, the total optical AM of the light beam is $\boldsymbol{J} = (\sigma + l)\hbar$. Just as the light beam can carry higher dimensional AM, Poincaré sphere can also be extended to the higher-order Poincaré sphere, which fully elucidates the relationship between polarization and optical AM for optical light beams[58,59]. In addition, due to the feature of visualization, Higher-order Poincaré sphere can also simplify the procedure of investigation of such light beams. The normalized higher-order Stokes parameters with respect to the higher-order circular basis

$|R_l\rangle$ and $|L_l\rangle$ can be summarized as,

$$S_0^\ell = \frac{|\langle R_\ell|\psi\rangle|^2 + |\langle L_\ell|\psi\rangle|^2}{|\langle R_\ell|\psi\rangle|^2 + |\langle L_\ell|\psi\rangle|^2} = 1 \tag{2.9}$$

$$S_1^\ell = \frac{2\,\mathrm{Re}\left(\langle R_\ell|\psi\rangle^* \langle L_\ell|\psi\rangle\right)}{|\langle R_\ell|\psi\rangle|^2 + |\langle L_\ell|\psi\rangle|^2} \tag{2.10}$$

$$S_2^l = \frac{2\,\mathrm{Im}\left(\langle R_\ell|\psi\rangle^* \langle L_\ell|\psi\rangle\right)}{|\langle R_\ell|\psi\rangle|^2 + |\langle L_\ell|\psi\rangle|^2} \tag{2.11}$$

$$S_3^\ell = \frac{|\langle R_\ell|\psi\rangle|^2 - |\langle L_\ell|\psi\rangle|^2}{|\langle R_\ell|\psi\rangle|^2 + |\langle L_\ell|\psi\rangle|^2} \tag{2.12}$$

where the circular basis $\{|R_l\rangle, |L_l\rangle\}$ can be written as,

$$R_\ell = (\hat{x} + \mathrm{i}\hat{y})\mathrm{e}^{-\mathrm{i}\ell\varphi}/\sqrt{2}, \tag{2.13}$$

$$L_\ell = (\hat{x} - \mathrm{i}\hat{y})\mathrm{e}^{\mathrm{i}\ell\varphi}/\sqrt{2}. \tag{2.14}$$

Here, $\hat{x}/\hat{y}$ is the unit vector in the x/y direction. Then, an arbitrary point (θ, ϕ) on the higher-order Poincaré sphere of l-order can stand for the SoP $\psi_\ell|\theta, \phi\rangle$ as follows,

$$\psi_\ell|\theta, \phi\rangle = \cos\left(\frac{\theta}{2}\right)|R_l\rangle\, e^{\frac{i\phi}{2}} + \sin\left(\frac{\theta}{2}\right)|L_l\rangle\, e^{-\frac{i\phi}{2}}. \tag{2.15}$$

For example, Fig.2.10(b) and (c) depict the first-order and the second-order Poincaré spheres, respectively. The SoP of E point $(\frac{\pi}{2}, 0)$ on the equator of the first-order Poincaré sphere can be expressed as,

$$\psi_{+1}\left|\frac{\pi}{2}, 0\right\rangle = \cos\varphi\hat{x} + \sin\varphi\hat{y} \tag{2.16}$$

which corresponds to the normalized Jones vector $[\cos\varphi \;\sin\varphi]^{\mathrm{T}}$. The SoP of I point $(\frac{\pi}{2}, 0)$ on the second-order Poincaré sphere can be expressed as,

$$\psi_{+2}\left|\frac{\pi}{2}, 0\right\rangle = \cos 2\varphi\hat{x} + \sin 2\varphi\hat{y} \tag{2.17}$$

which corresponds to the normalized Jones vector $[\cos 2\varphi \; 2\sin\varphi]^{\mathrm{T}}$. According to Eq.(2.15), it can be deduced that higher-order Poincaré sphere can intuitively describe the SoP of general vector beams which are all projected onto the equator of each higher-order Poincaré sphere of l-order. Thus, the SoP of vector beams can be expressed based on Jones vector,

$$\psi_l \left| \frac{\pi}{2}, \phi \right\rangle = \left[\cos\left(\frac{\phi}{2} - l\varphi \right) \; - \sin\left(\frac{\phi}{2} - l\varphi \right) \right]^{\mathrm{T}}. \tag{2.18}$$

Two poles of the higher-order Poincaré sphere represent the vector vortex beams with both SAM $\sigma\hbar$ and OAM $l\hbar$. respectively. Except for two poles and an equator, all other intermediate points on the spherical surface correspond to elliptically polarized vector beams.

According to the above analysis, the fundamental Poincaré sphere can characterize the homogeneous SoP distribution and the higher-order Poincaré sphere can characterize the non-homogeneous SoP distribution. In addition, when a in Eq.(2.4) is 0 or 1, namely $\theta = 0$ or π, Eq.(2.4)/Eq.(2.15) can be regarded as the separable state (a product state), which represents the light beam is purely scalar. whereas a in Eq.(2.4) is $\frac{1}{2}$, namely $\theta = \frac{\pi}{2}$, the light field is viewed as purely vector (the maximally entangled state). Except for purely scalar and purely vector, the light field could also be partially vector which is an intermediate state between scalar and vector fields. Since vector mode is generally regarded as the entangled state in its spatial mode and polarization dimensions, the degree of entanglement C is employed to characterize the vector quality factor (VQF), ranging from 0 (purely scalar field) to 1 (pure vector field)[60,61]. The VQF can be presented based on the parameter C,

$$\mathrm{VQF} = \mathrm{Re}(C) = \mathrm{Re}\left(\sqrt{1 - s^2}\right) = |\sin(\theta)|. \tag{2.19}$$

Here, s can be viewed as the degree of polarization of the averaged SoP and can be expressed as follows,

$$s = \left(\sum_i \langle \sigma_i \rangle^2 \right)^{1/2} \tag{2.20}$$

where σ_i is the expectation value of each Pauli operator (i = 1, 2 and 3) and can be calculated from 12 normalized intensity I_{Rj}/I_{Lj} as,

$$\langle \sigma_1 \rangle = (I_{R3} + I_{L3}) - (I_{R5} + I_{L5}), \tag{2.21}$$

$$\langle \sigma_2 \rangle = (I_{R4} + I_{L4}) - (I_{R6} + I_{L6}), \tag{2.22}$$

$$\langle \sigma_3 \rangle = (I_{R1} + I_{L1}) - (I_{R2} + I_{L2}). \tag{2.23}$$

Here, the circular basis $\{|R_l\rangle, |L_l\rangle\}$ is employed as the measurement basis and the intensity $I_{R/Lj}$ is normalized to the total intensity. For each basis state $|R_l\rangle/|L_l\rangle$, right- and left-circular polarizations with associated OAM and four superposition states, $|R_l\rangle + \exp(i\Theta)|L_l\rangle/|L_l\rangle + \exp(i\Theta)|R_l\rangle$ ($\Theta = 0, \pi/2, \pi, 3\pi/2$) are marked by I_{Rj}/I_{Lj}, which are listed in Table **2.1**. In this way, the VQF can be effectively evaluated.

Table 2.1: 12 normalized Intensity measurements based on the circular basis.

Basis state	ℓ	$-\ell$	$\Theta=0$	$\Theta=\pi/2$	$\Theta=\pi$	$\Theta=3\pi/2$
$\lvert R_l\rangle$	I_{R1}	I_{R2}	I_{R3}	I_{R4}	I_{R5}	I_{R6}
$\lvert L_l\rangle$	I_{L1}	I_{L2}	I_{L3}	I_{L4}	I_{L5}	I_{L6}

2.2.2 Theoretical model for generation and transformation of VM

For circular-core shaped fiber, vector eigenmodes are the direct solutions to vector wave equation and nonuniform distribution in polarization dimension is a main feature, which could be characterized by parameters l and γ,

$$|l, \gamma\rangle = [\cos(l\varphi + \gamma)\ \sin(l\varphi + \gamma)]^{\mathrm{T}}. \tag{2.24}$$

Here, l denotes the azimuthal order number and γ is 0 or $\frac{\pi}{2}$, which determines the initial polarization angle. $\varphi = \arctan(y/x)$ is referred as the azimuthal angle on the transverse plane. For example, $|1, 0\rangle$ and $|1, \frac{\pi}{2}\rangle$ represents the radial vector mode (TM_{01}) and azimuthal vector mode (TE_{01}), respectively. Similar to the Poincaré sphere method, Jones matrix theory can be used to characterize generation and transformation of the vector mode, which can be derived with,

$$\mathbf{E_{out}} = \mathbf{J_s}\mathbf{E_{in}}. \tag{2.25}$$

Here, $\mathbf{J_s}$ denotes the operator of the used optical element which acts on the input light beam and $\mathbf{E_{in}}/\mathbf{E_{out}}$ represents the SoP of input/output light beam. For the generation of vector mode, passive generation methods based on VWPs or Q-plates are commonly used in free space[62]. Here, take Q-plate as an example. Q-plate is a liquid optical device which is able to regulate the SoP of incident light field and the local optical axis χ of Q-plate is written as[63],

$$\chi(r, \varphi) = q\varphi + \chi_0 \tag{2.26}$$

where q in this expression stands for the topological charge and χ_0 stands for the constant offset angle with reference to the x axis. As can be seen, the optical axis orientation is assumed as specified by the angle φ. Thus, the Jones matrix of such Q-plate to be acted on the incident light field at each point of can be expressed as,

$$\mathbf{Q} = R(-\chi)\begin{bmatrix} 1 & 0 \\ 0 & -1 \end{bmatrix} R(\chi) = \begin{bmatrix} \cos 2\chi & \sin 2\chi \\ \sin 2\chi & -\cos 2\chi \end{bmatrix}. \tag{2.27}$$

In this equation, $R(\chi)$ is the standard 2×2 rotation matrix. When Eq.(2.26) is substituted into Eq.(2.27), the $\mathbf{Q}$ can be written as,

$$\mathbf{Q} = \begin{bmatrix} \cos 2\left(q\varphi + \chi_0\right) & \sin 2\left(q\varphi + \chi_0\right) \\ \sin 2\left(q\varphi + \chi_0\right) & -\cos 2\left(q\varphi + \chi_0\right) \end{bmatrix}. \tag{2.28}$$

Thus, when the incident light is the fundamental mode with homogeneous linear SoPs $[\cos\phi\ \ \sin\phi]^{\mathrm{T}}$ (ϕ represents the azimuth spherical angle.) which correspond to the equator of fundamental Poincaré sphere, Q-plate can modify it into vector mode according to Eq.(2.24) and Eq.(2.29), which can be written as,

$$\begin{aligned}\mathbf{E_{out}} = \mathbf{QE_{in}} &= \begin{bmatrix} \cos 2\left(q\varphi + \chi_0\right) & \sin 2\left(q\varphi + \chi_0\right) \\ \sin 2\left(q\varphi + \chi_0\right) & -\cos 2\left(q\varphi + \chi_0\right) \end{bmatrix} \begin{bmatrix} \cos\phi \\ \sin\phi \end{bmatrix} \\ &= \begin{bmatrix} \cos(2q\varphi + 2\chi_0 + \phi) \\ \sin(2q\varphi + 2\chi_0 + \phi) \end{bmatrix}. \end{aligned} \tag{2.29}$$

With regard to the higher-order Poincaré sphere model and Jones calculus, the generation of vector mode based on Q-plate can be given by (assuming $\chi_0 = 0$),

$$\psi_l \left|\frac{\pi}{2}, \phi\right\rangle \overset{\mathrm{QP}(\chi_0=0)}{\leftrightarrows} \psi_{(2q-l)} \left|\frac{\pi}{2}, -\phi\right\rangle. \tag{2.30}$$

Some typical transformations about vector mode generation by Q-plate based on higher-order Poincaré sphere model are illustrated in Fig.2.11. In addition, HWP is a common type of retarder plate and is usually employed to rotate linear polarized light traveling through it. HWP can also be applied to the transformation of vector mode and the Jones matrix of HWP with the fast axis at angle α to the x axis is given by,

$$\mathbf{P} = \begin{bmatrix} \cos\alpha & -\sin\alpha \\ \sin\alpha & \cos\alpha \end{bmatrix} \begin{bmatrix} \exp(i\pi/2) & 0 \\ 0 & \exp(i\pi/2) \end{bmatrix} \begin{bmatrix} \cos\alpha & \sin\alpha \\ -\sin\alpha & \cos\alpha \end{bmatrix} \tag{2.31}$$

Similar to the above derivation, the function of HWP acting on vector mode corresponding to the equator of high-order Poincaré sphere ($|l| \geq 1$) can be summarized as ($\mathbf{E_{out}} = \mathbf{PE_{in}}$),

$$\psi_l \left|\frac{\pi}{2}, \phi\right\rangle \overset{\mathrm{HWP}}{\leftrightarrows} \psi_{-l} \left|\frac{\pi}{2}, -(\phi + 4\alpha)\right\rangle \tag{2.32}$$

in which the order of vector mode is transformed from l-order to $-l$-order after traveling through HWP. Some typical transformations about vector mode by HWP based on higher-order Poincaré sphere model are also illustrated in Fig.2.11. Based on the above analysis, the SoP mapped onto a Poincaré sphere of m-order can be transformed to another sphere of n-order with the help of Q-plate and HWP. Here, take three SoPs of labeled points (A, C and E points) in Fig.2.11 to illustrate this transformation, which can be exemplified as follows,

$$\underbrace{(1,0)^{\mathrm{T}}}_{\text{A point}} \overset{\mathrm{QP}(q=1/2,\,\chi_0=0)}{\leftrightarrows} \underbrace{(\cos\varphi, \sin\varphi)^{\mathrm{T}}}_{\text{C point}} \overset{\mathrm{HWP}(\alpha=\pi/2)}{\leftrightarrows} \underbrace{(\cos\varphi, -\sin\varphi)^{\mathrm{T}}}_{\text{E point}} \tag{2.33}$$

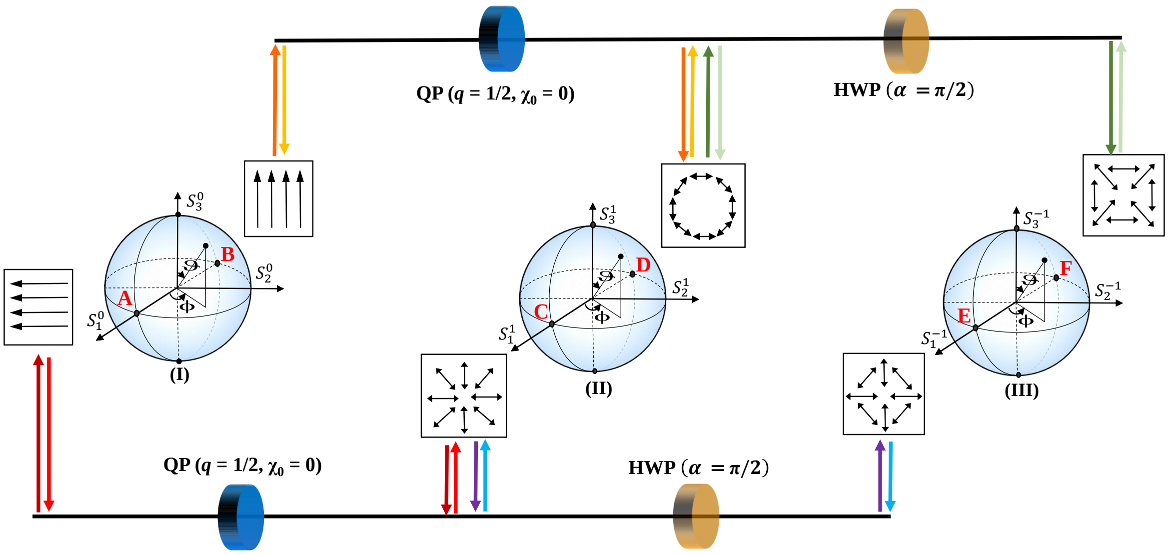

Figure 2.11: Generation and transformation of VM based on high-order Poincaré sphere model. (I): Fundamental Poincaré sphere of $l = 0$; (II) Poincaré sphere of $l = 1$; (III) Poincaré sphere of $l = -1$; QP: Q-plate; HWP: half-wave plate.

This method of procedure can also be extended to the generation of vector vortex beam with SAM ($|R_l\rangle$ $/|L_l\rangle$) and OAM ($\exp(-il\varphi)/\exp(il\varphi)$) based on Q-plate. According to Jones calculus, this transformation obeys the following rules,

$$\psi_l\,|l, R\rangle \overset{\mathrm{QP}}{\leftrightarrows} \psi_{l+2q}\,|l+2q, L\rangle\,, \tag{2.34}$$

$$\psi_l\,|l, L\rangle \overset{\mathrm{QP}}{\leftrightarrows} \psi_{l-2q}\,|l-2q, R\rangle\,, \tag{2.35}$$

as exemplified in Fig.2.12. It can be noted that right-/left- circular polarization located on the north/south pole of the fundamental Poincaré sphere is converted to left-/right circular polarization coupled with OAM of $l = 1/l = -1$ located on the south/north pole of the Poincaré sphere of $l = 1$ by the Q-plate ($q = 1/2$).

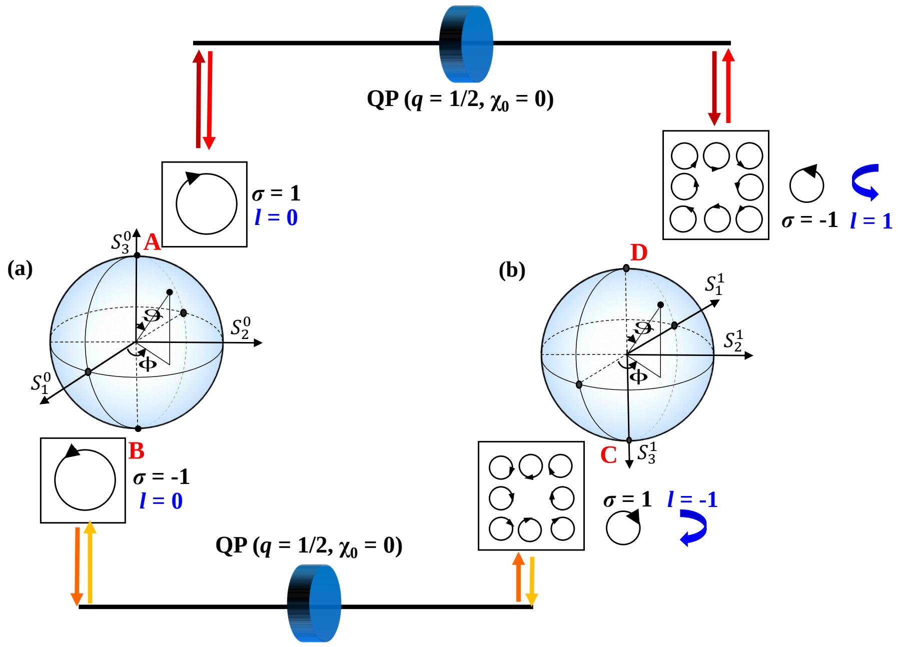

Figure 2.12: Generation of OAM mode based on high-order Poincaré sphere model. (a): Fundamental Poincaré sphere of $l = 0$; (b): Poincaré sphere of $l = 1$; QP: Q-plate.

2.3 Fiber eigenmode characterization in FMF

2.3.1 Mode calculation in FMF

To characterize the performance of vector mode transmission in the fiber, mode calculation of the FMF used in the study is first carried out based on the full-vector finite-element mode solver. Figure 2.13 (a) shows the index profile of the used FMF. Here, the step-index FMF with 5×10^{-3} refractive index difference between the core ($n_1 = 1.449$) and the cladding ($n_1 = 1.444$) is utilized. The core diameter and the cladding diameter of the FMF are respectively 19 μm (2a) and 125 μm (2b). Mode calculation for this FMF is performed by COMSOL multi-physics simulation tool. For wavelength of 1550 nm, seven fiber eigenmodes including HE_{11}, TE_{01}, HE_{21}, TM_{01}, EH_{11}, HE_{31} and HE_{12}, namely four LP modes including LP_{01}, LP_{11}, LP_{21} and LP_{02} are supported by the given FMF, which are respectively illustrated in Fig.2.13 (c) and (b).

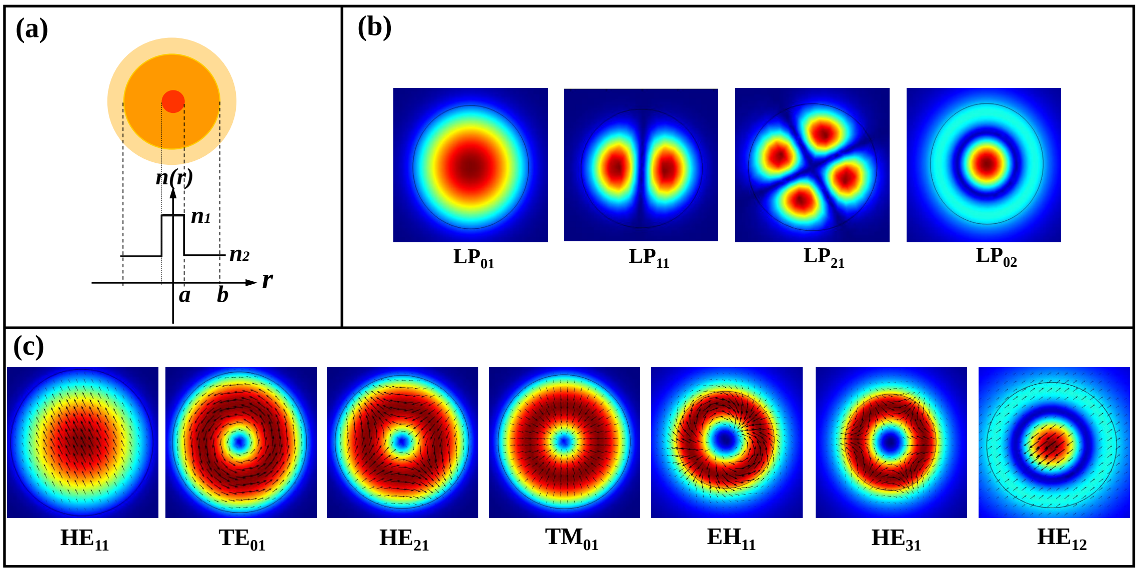

Figure 2.13: (a) Refractive index profile of the used FMF. (b) LP modes and (c) vector modes supported by the used FMF, respectively.

In addition, the effective refractive indices (n_{eff}) of each supported mode is also obtained from the wavelength of 1250 nm to 1650 nm, shown in Fig.2.14. According to the propagation constants β ($\beta = 2\pi n_{eff}/\lambda$) of these modes, they are put into mode groups (MG) of four, shown in Fig.2.15. The modes belonging to the same MG share the same or very similar propagation constant.

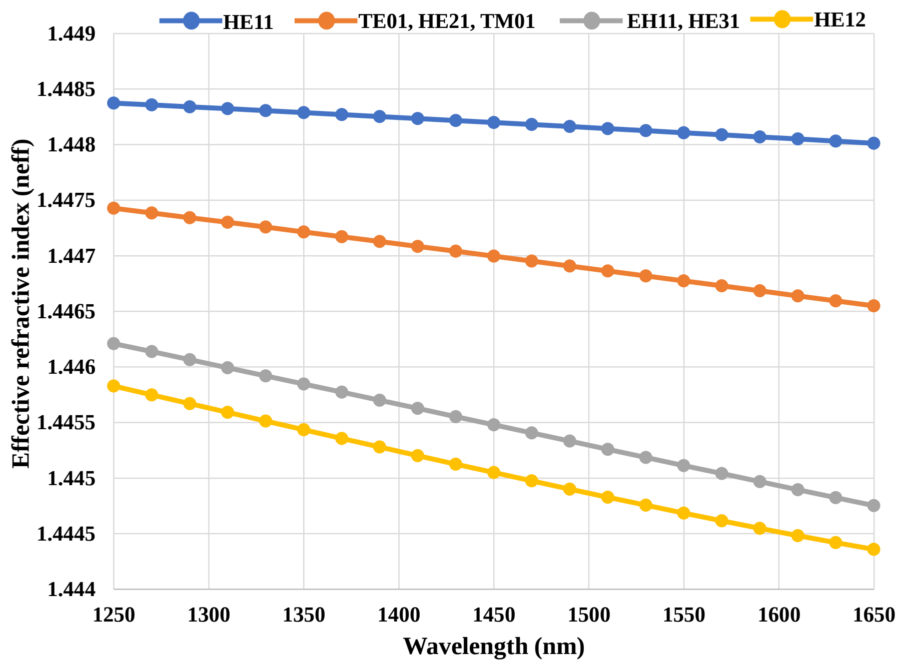

Figure 2.14: Effective refractive index of each VM versus wavelength in the used FMF.

2.3.2 Different mode bases and their relationships

In the first chapter, vector and scalar modes are introduced and it can be deduced that LP modes are actually pseudo modes composed of vector modes with the identical or very similar propagation constant for weakly-guiding fibers. For SMF, only the fundamental mode composed of HE_{11}^{e} and HE_{11}^{o} is allowed to transmit and arbitrary electric field can be regarded as a linear superposition of these two basis states. For FMF or MMF, the fundamental mode and several higher-order modes are all allowed to transmit. Specifically, these modes can be defined by different orders according to l and m. Here, l and m respectively denote azimuthal and radial order of modes. When the polarization of LP mode is also considered, the relationship between LP and VM

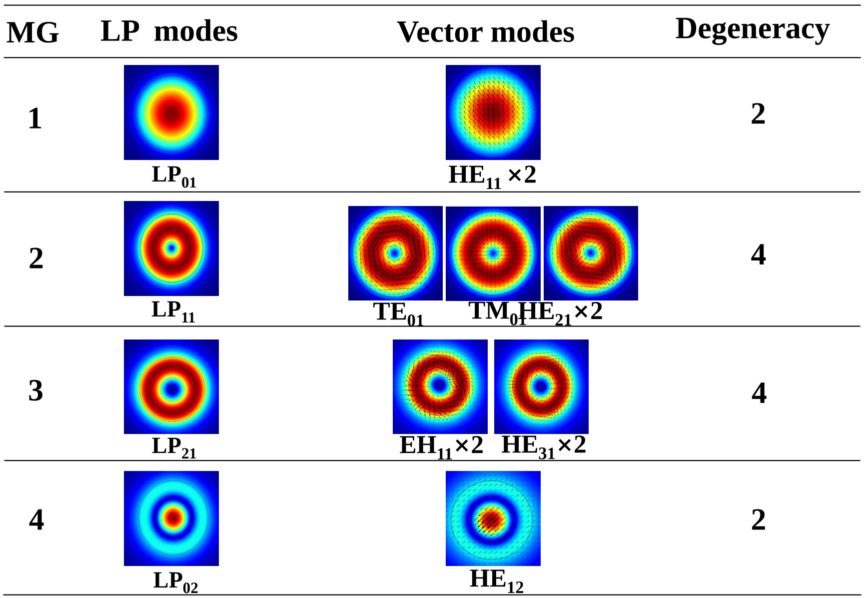

Figure 2.15: Four mode groups in the used FMF.

in a certain order can be given by,

$$\hat{x}/\hat{y}\mathrm{LP}^{e}_{0,m} = \mathrm{HE}^{e/o}_{1,m}. \qquad l = 0, m \geq 1 \tag{2.36}$$

$$\left.\begin{aligned} \hat{x}\mathrm{LP}^{e}_{l,m} &= \mathrm{HE}^{e}_{(l+1),m} - \mathrm{EH}^{e}_{(l-1),m}, \\ \hat{x}\mathrm{LP}^{o}_{l,m} &= \mathrm{HE}^{o}_{(l+1),m} - \mathrm{EH}^{o}_{(l-1),m}, \\ \hat{y}\mathrm{LP}^{e}_{l,m} &= \mathrm{HE}^{o}_{(l+1),m} + \mathrm{EH}^{o}_{(l-1),m}, \\ \hat{y}\mathrm{LP}^{o}_{l,m} &= \mathrm{HE}^{e}_{(l+1),m} + \mathrm{EH}^{e}_{(l-1),m}. \end{aligned}\right\} l \geq 1, m \geq 1 \tag{2.37}$$

It is noted that when $l = 1$, $\mathrm{EH}^{e}_{(l-1),m}/\mathrm{EH}^{o}_{(l-1),m}$ is replaced with $\mathrm{TM}_{0,m}/\mathrm{TE}_{0,m}$ in Eq.(2.37). Thus, when $l \geq 1$, the LP and vector modes both have four basis states in each order and the relationship can be further written as,

$$\begin{bmatrix} \hat{x}\mathrm{LP}^{e}_{l,m} \\ \hat{x}\mathrm{LP}^{o}_{l,m} \\ \hat{y}\mathrm{LP}^{e}_{l,m} \\ \hat{y}\mathrm{LP}^{o}_{l,m} \end{bmatrix} = \begin{bmatrix} 1 & -1 & 0 & 0 \\ 0 & 0 & 1 & -1 \\ 0 & 0 & 1 & 1 \\ 1 & 1 & 0 & 0 \end{bmatrix} \begin{bmatrix} \mathrm{HE}^{e}_{(l+1),m} \\ \mathrm{EH}^{e}_{(l-1),m} \\ \mathrm{HE}^{o}_{(l+1),m} \\ \mathrm{EH}^{o}_{(l-1),m} \end{bmatrix} \qquad l \geq 1, m \geq 1. \tag{2.38}$$

The relationship of OAM with a phase singularity (scalar) and VM with a polarization singularity (vector) could be established based on the higher-order Poincaré

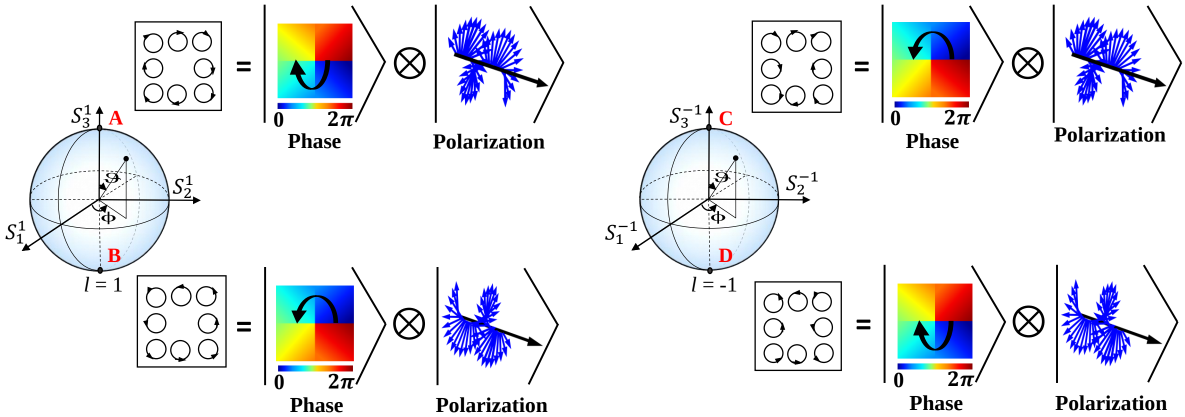

Figure 2.16: Circular polarizations with OAM on the Poincaré sphere of $l = \pm 1$.

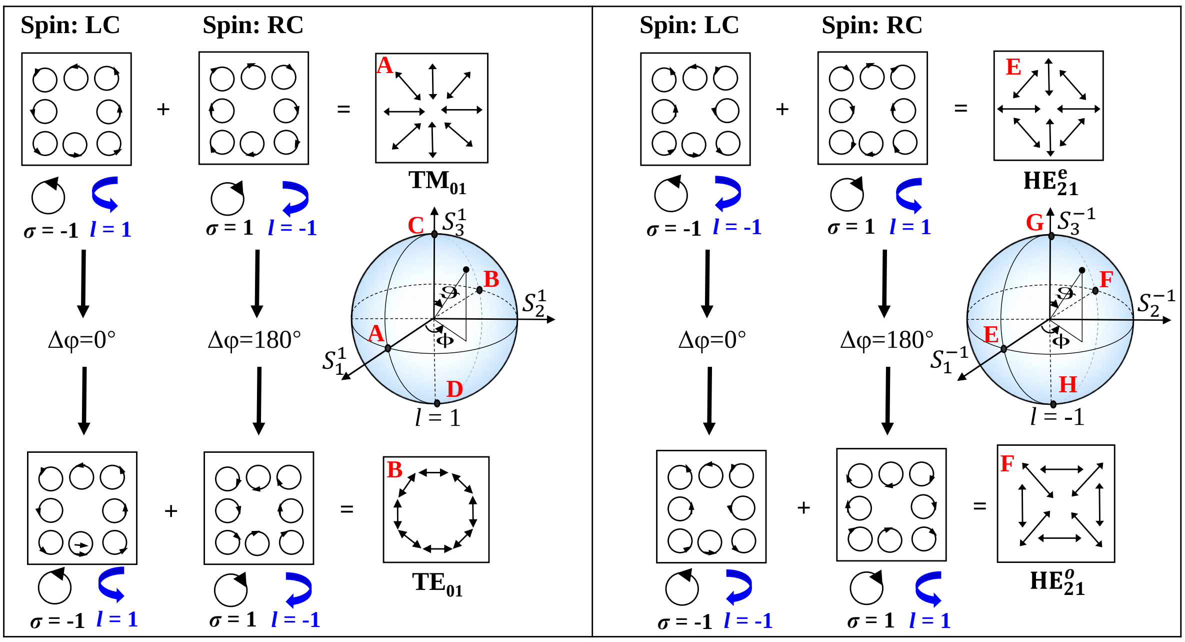

Figure 2.17: Basic superposition mechanism of vector modes.

sphere framework. For example, Fig.2.16 sketches four states all having signs of SAM and OAM on the north/south poles of Poincaré sphere of $l = \pm 1$, which can be viewed as four basis states $\mathrm{OAM}^{+\sigma}_{-1,m}$, $\mathrm{OAM}^{-\sigma}_{+1,m}$, $\mathrm{OAM}^{+\sigma}_{+1,m}$ and $\mathrm{OAM}^{-\sigma}_{-1,m}$ for $|l| = 1$. According to Eq.(2.13) and Eq.(2.14), the states on the north and south poles are regarded as separable, since these states can be expressed as the product of a helical phase state and right-/left- circular SoPs. Algebraically, based on the Eq.(2.15), the standard vector modes: transverse magnetic TM_{01}, transverse electric TE_{01}, hybrid electric even HE^{e}_{21} and hybrid electric odd HE^{o}_{21}, corresponding to A, B, E and F points in Fig.2.17 respectively, can be generated from combinations of four OAM basis states ($\mathrm{OAM}^{+\sigma}_{-1,m}, \mathrm{OAM}^{-\sigma}_{+1,m}, \mathrm{OAM}^{+\sigma}_{+1,m}, \mathrm{OAM}^{-\sigma}_{-1,m}$) and this superposition mechanism is shown in Fig.2.17. As can be seen, TM_{01} or $\mathrm{TE}_{01}/\mathrm{HE}^{e}_{21}$ or HE^{o}_{21} is generated by the superstition of $\mathrm{OAM}^{+\sigma}_{-1,m}$ and $\mathrm{OAM}^{-\sigma}_{+1,m}/\mathrm{OAM}^{+\sigma}_{+1,m}$ and $\mathrm{OAM}^{-\sigma}_{-1,m}$ with zero or π phase offset. Furthermore, this superposition mechanism can also be extended to arbitrary order. Here, standard vector modes mapped on the $(\frac{\pi}{2}, 0)$ and $(\frac{\pi}{2}, \pi)$ points on the higher-order Poincaré sphere of $+l$ and $-l$ ($l \geq 1$) which respectively correspond to $\mathrm{EH}^{\mathrm{e}}_{l-1,m}$ and $\mathrm{EH}^{\mathrm{o}}_{l-1,m}/\mathrm{HE}^{\mathrm{e}}_{l+1,m}$ and $\mathrm{EH}^{\mathrm{o}}_{l+1,m}$ modes are taken into account. These four VMs are specified by the following Jones vectors ($l \geq 1$, $m \geq 1$. When $l = 1$, $\mathrm{EH}^{e}_{(l-1),m}/\mathrm{EH}^{o}_{(l-1),m}$ is replaced with $\mathrm{TM}_{0,m}/\mathrm{TE}_{0,m}$.),

$$\psi_{+l}\left|\frac{\pi}{2}, 0\right\rangle = \begin{pmatrix} \cos(l\varphi) \\ \sin(l\varphi) \end{pmatrix} \qquad \mathrm{EH}^{\mathrm{e}}_{l-1,m}/\mathrm{TM}_{0,m}. \tag{2.39}$$

$$\psi_{+l}\left|\frac{\pi}{2}, \pi\right\rangle = \begin{pmatrix} -\sin(l\varphi) \\ \cos(l\varphi) \end{pmatrix} \qquad \mathrm{EH}^{\mathrm{o}}_{l-1,m}/\mathrm{TE}_{0,m}. \tag{2.40}$$

$$\psi_{-l}\left|\frac{\pi}{2}, 0\right\rangle = \begin{pmatrix} \cos(l\varphi) \\ -\sin(l\varphi) \end{pmatrix} \qquad \mathrm{HE}^{\mathrm{e}}_{l+1,m}. \tag{2.41}$$

$$\psi_{-l}\left|\frac{\pi}{2}, \pi\right\rangle = \begin{pmatrix} \sin(l\varphi) \\ \cos(l\varphi) \end{pmatrix} \qquad \mathrm{HE}^{\mathrm{o}}_{l+1,m}. \tag{2.42}$$

Thus, based on Eq.(2.13), Eq.(2.14), Eq.(2.24) and Eq.(2.15), the generalized relationships between OAM associated with right-/left-circular polarization and standard VMs for each order can be summarized as ($l \geq 1$, $m \geq 1$),

$$\left.\begin{aligned} \mathrm{EH}^{\mathrm{e}}_{l-1,m} &= \left(\mathrm{OAM}^{+\sigma}_{-l,m} + \mathrm{OAM}^{-\sigma}_{+l,m}\right) = u_{l,m}(\mathbf{r})[\cos(l\varphi)\hat{x} + \sin(l\varphi)\hat{y}], \\ \mathrm{EH}^{\mathrm{o}}_{l-1,m} &= i\left(\mathrm{OAM}^{-\sigma}_{+l,m} - \mathrm{OAM}^{+\sigma}_{-l,m}\right) = u_{l,m}(\mathbf{r})[-\sin(l\varphi)\hat{x} + \cos(l\varphi)\hat{y})], \\ \mathrm{HE}^{\mathrm{e}}_{l+1,m} &= \left(\mathrm{OAM}^{-\sigma}_{-l,m} + \mathrm{OAM}^{+\sigma}_{+l,m}\right) = u_{l,m}(\mathbf{r})[\cos(l\varphi)\hat{x} - \sin(l\varphi)\hat{y}], \\ \mathrm{HE}^{\mathrm{o}}_{l+1,m} &= i\left(\mathrm{OAM}^{-\sigma}_{-l,m} - \mathrm{OAM}^{+\sigma}_{+l,m}\right) = u_{l,m}(\mathbf{r})[\sin(l\varphi)\hat{x} + \cos(l\varphi)\hat{y}]. \end{aligned}\right\} \tag{2.43}$$

$$\left.\begin{aligned} \mathrm{OAM}^{\pm\sigma}_{\pm l,m} &= \mathrm{HE}^{\mathrm{e}}_{l+1,m} \pm i\mathrm{HE}^{\mathrm{o}}_{l+1,m} = u_{l,m}(\mathbf{r})(\hat{x} \pm i\hat{y})\exp(\pm il\varphi), \\ \mathrm{OAM}^{\mp\sigma}_{\pm l,m} &= \mathrm{EH}^{\mathrm{e}}_{l-1,m} \pm i\mathrm{EH}^{\mathrm{o}}_{l-1,m} = \mathrm{u}_{l,m}(\mathbf{r})(\hat{x} \mp i\hat{y})\exp(\pm il\varphi). \end{aligned}\right\} \tag{2.44}$$

Here, $u_{l,m}(\mathbf{r})$ represents the radial electric field distribution. The transformation matrix can be further written as ($l \geq 1$, $m \geq 1$),

$$\begin{bmatrix} \mathrm{OAM}^{+\sigma}_{+l,m} \\ \mathrm{OAM}^{+\sigma}_{-l,m} \\ \mathrm{OAM}^{-\sigma}_{+l,m} \\ \mathrm{OAM}^{-\sigma}_{-l,m} \end{bmatrix} = \begin{bmatrix} 1 & 0 & i & 0 \\ 0 & 1 & 0 & -i \\ 0 & 1 & 0 & i \\ 1 & 0 & -i & 0 \end{bmatrix} \begin{bmatrix} \mathrm{HE}^{e}_{(l+1),m} \\ \mathrm{EH}^{e}_{(l-1),m} \\ \mathrm{HE}^{o}_{(l+1),m} \\ \mathrm{EH}^{o}_{(l-1),m} \end{bmatrix}. \tag{2.45}$$

2.3.3 Experimental setups

The versatile higher-order Poincaré sphere integrates angular momentum and polarization into a unified theoretical framework. It builds the relationship between vector and OAM modes as well, which could be utilized to analyze the performance of vector mode traveling in the fiber. Figure 2.18 illustrates the experimental setup to detect the vector mode after FMF transmission. The CW lightwave at 1550 nm from an external cavity laser (ECL) is divided into two branches by an optical coupler (OC). One branch acted as the reference light for the following interference experiment. Another branch is first converted to the linear polarized light after passing through the linear polarizer. The polarization controller (PC) in this branch is employed to maximize the output power from LP. Next, the linear polarized light is converted to TM_{01} mode by the Q-plate of $q = 1/2$ and is fed into the FMF. During the fiber propagation, a FMF-PC modeled according to a single-mode PC is utilized to properly adjust the output pattern. Then, the output beam from FMF passes through the polarization grating (PG), which is able to split orthogonal circular polarization. Finally, two separated beams are interfered with the reference light, respectively.

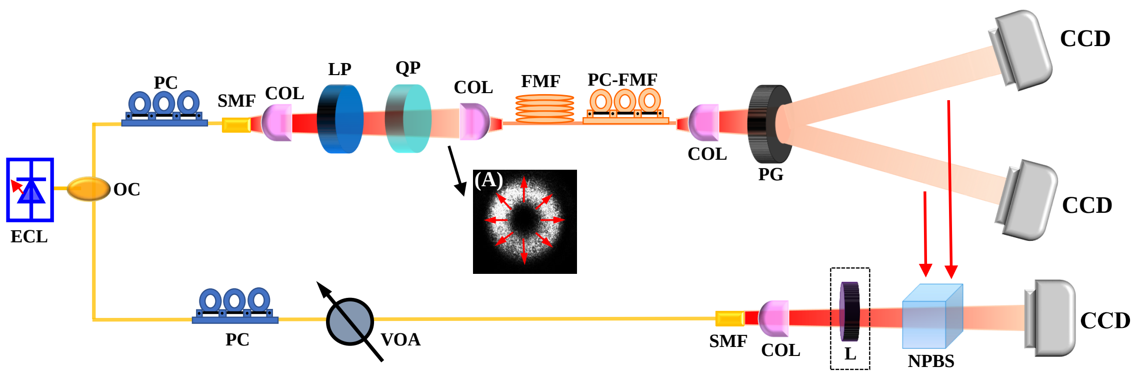

Figure 2.18: Experimental setup of characterizing VM performance over FMF transmission. ECL: external cavity laser; OC: optical coupler; PC: polarization controller; SMF: single-mode fiber; COL: collimator; LP: linear polarizer; QP: q-plate; FMF: few-mode fiber; PC-FMF: polarization controller based on four-mode fiber; PG: polarization grating; CCD: charged-coupled device camera; VOA: variable optical attenuator; L: lens; NPBS: non-polarizing beam splitter. Inset (A) depicts the intensity pattern of the generated vector mode.

2.3.4 Experimental results

To evaluate the performance of VM traveling in the FMF, the intensity profiles and SoP distributions before and after FMF transmission are first captured by CCD camera, which is the most intuitive judgment. Insets (A_1) and (A_2) in Fig.**2.19** (a) depicts the intensity patterns before and after FMF transmission. Compared to the input pattern with a standard doughnut shape, the output pattern is not perfect. Then, the SoP distribution is confirmed when LP rotates before CCD camera, which is shown in insets (a_1) and (a_2) in Fig.**2.19** (a). As can be seen, the output SoP still matches with the input although the output beam rotates a certain angle compared to the input beam. Based on Eq.**(2.15)**, the standard VM is composed of two OAM modes with opposite helical phases and opposite SAM. Theoretically, the power of these two branches of OAM modes is equivalent no matter in free space or fiber. Thus, the output beam from FMF is decomposed by PG in the above experiment and the power of two separate parts is measured by an optical power meter for free space, 5 m FMF and 100 m FMF transmission, respectively. According to the normalized results listed in Fig.2.19 (b), compared to free space transmission, the weight of two separate parts becomes further imbalanced after FMF transmission, which indicates the performance is degraded to a certain degree. There are some possible reasons that lead to this result such as immature optical components, imperfect structure of used fiber and random mode mixing during the fiber transmission. Finally, two branches split by PG after 5 m FMF transmission (insets (B_1) and (C_1) in Fig.2.19 (c) are respectively interfered with the reference beam of a spherical/plane wave. The interference patterns are respectively shown in insets (B_2)/(B_3) and (C_2)/(C_3) in Fig.2.19 (c), which agree with the theoretical analysis.

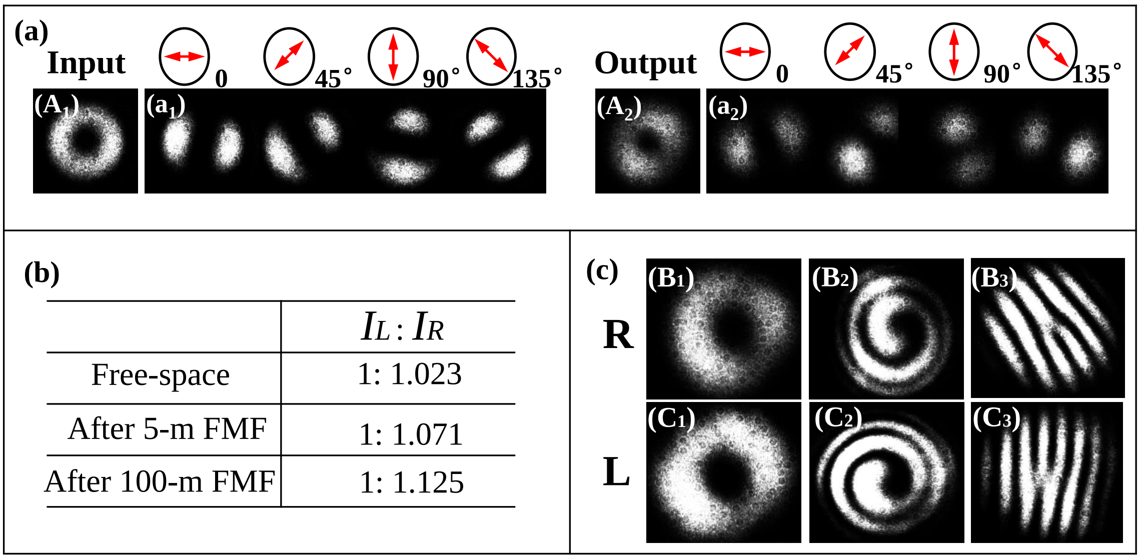

Figure 2.19: (a) Insets (A_1) and (A_2) are respectively the intensity distributions before and after FMF transmission. Insets (a_1) and (a_2) respectively depict the SoP of input and output patterns. (b) Measured power ratios after free space, 5 m FMF and 100 m FMF transmission. (c): Insets (B_1) and (C_1) show the separated left- and right-handed polarization intensity profiles after 5 m FMF transmission. Insets (B_2) and (C_2) depict the interference patterns of the clockwise spiral and the counter clockwise spiral with the fundamental mode of a spherical wave, respectively. Insets (B_3) and (C_3) depict the interference patterns of the clockwise spiral and the counter clockwise spiral with the fundamental mode of a plane wave, respectively.

2.4 Summary

In this chapter, CVB-based MDM FSO link (80 cm) under three atmospheric turbulence conditions by using Kramers–Kronig reception and 4×4 non-singular MIMO is first experimentally evaluated. Moreover, the performance of averaged BER properties of four used CV mode channels is analyzed. The results show that atmospheric turbulence will lead to the fluctuation of BER performance and the fluctuation of crosstalk within or among mode groups to some extent. Then, similar to the uniform state of polarization mapped on Poincaré sphere, the main feature of VM is presented and analyzed by high-order Poincaré sphere model. Finally, the performance of VMs propagated in FMF is also investigated based on Poincaré sphere.

3

High-capacity VM-based MDM FMF systems

In this chapter, based on fiber eigenmodes, two MDM scenarios aimed at developing short-reach fiber-optic communication systems are proposed and demonstrated, which provides the possibility of future high-capacity SDM/MDM transmission with high SE and low cost.

3.1 Fiber Vector Eigenmode Multiplexing Based Transmission with Kramers-Kronig receiver

3.1.1 Kramers-Kronig Receiver

Short-reach optical interconnect, such as data center interconnect (DCI), is an important component in the infrastructure to support massive Internet applications based on data centers. In the big-data and AI era, the fast-increasing capacity requirement has created the need to constantly improve the transmission data rate to meet the ever-increasing traffic demand. Optical interconnect, as a promising solution for up to 400 Gbit/s signal transmission in short-reach links, still faces various barriers and challenges. For fiber-optic communication systems, thanks to the digital coherent detection with DSP technique at the transceiver side, advanced multi-level and multi-dimensional modulation formats with high SE and high sensitivity can be successfully deployed, which enables high bit rate as well as long-haul transmission. Specifically, coherent detection can maximize the SNR of each optical communication channel. The high-spectral efficiency of signal modulation formats such as QAM relied on the high SNR. Thus, the signal can be transmitted in both intensity and phase of the optical wave. However, the SNR is hard to be further increased because of the limitation of transmission optical power by optical nonlinearity. In the meanwhile, the cost of the coherent receiver is a main barrier in the case of short-reach links, whose part in many fields of becomes more and more important. Actually, the coherent receiver utilized today is based on the intradyne scheme, which needs two optical hybrids and four pairs of balanced PDs, making its overall cost unacceptably high for short-reach links. Accordingly, I/Q modulation and coherent detection are generally abandoned in short-reach transmission. Compared to coherent detection, intensity modulation and direct detection (IM/DD) solutions have the advantages of low cost, low power consumption and simple optical hardware structure, which occupy the main market position of short-reach interconnects. In IM/DD systems, the information is encoded onto the amplitude of the optical wave and only real-valued signals could be transmitted. With the increasing demand for data rates, short-reach IM-DD transmission will be undoubtedly stretched to its limit.

Recently, I/Q modulation and Kramers-Kronig (KK) receiver which takes advantage of both complex modulation and direct detection are introduced in optical communication systems[2]. It is low-cost and can reconstruct the complex electrical field carried over optical light simply via PD by DD of the optical signal along with another same polarization optical tone shifted to the verge of the optical signal, where the amplitude information is directly obtained after detection and the phase information can be well-extracted by Hilbert transformation of amplitude information with enough optical carrier signal power ratio (CSPR) before PD. In the meanwhile, KK receiver can fully reconstruct optical phase information which is compatible with DSP for compensating the impairments. In detail, KK receiver requires two conditions: first, the optical signal is a single side band (SSB). Second, the high-power carrier should satisfy minimum phase condition, namely high carrier-to-signal power ratio (CSPR). Here, $E_s(t)$ represents the complex envelope of the electric field and is assumed to be contained within a finite optical bandwidth represented by B. The LO with the amplitude of E_0 is a CW signal whose frequency coincides with the left edge of the information-carrying signal spectrum. Therefore, the complex envelope of the field impinging upon the PD is $E(t) = E_s(t) + E_0\exp(i\pi Bt)$. The photocurrent I produced by the PD is proportional to the field intensity $I = |E(t)|^2$, where the proportionality coefficient can be set as 1. Assuming that E_0 is large enough to ensure that the signal $E(t)\exp(-i\pi Bt) = E_0 + E_s(t)\exp(-i\pi Bt)$ is minimum phase. The signal $E_s(t)$ could be reconstructed as follows:

$$E_s\left(t\right) = \left\{\sqrt{I\left(t\right)}\exp\left[i\phi_E\left(t\right)\right] - E_0\right\}\exp\left(i\pi Bt\right) \tag{3.1}$$

$$\phi_E\left(t\right) = \frac{1}{2\pi}\text{p.v.}\int_{-\infty}^{\infty} dt' \frac{\log\left[I\left(t'\right)\right]}{t-t'} \tag{3.2}$$

Figure **3.1** illustrates two schemes of KK receiver. In the first line, the carrier is electrically added along with the electrical signals, with half of the bandwidth frequency shift, while in the second line, the carrier is added optically with half of the bandwidth frequency shift. KK receiver scheme allows digital post-compensation of linear propagation impairments. In addition, compared to other existing solutions, KK receiver is more efficient in terms of spectral occupancy and energy consumption, making it a potential candidate for next-generation short-reach optical interconnects. In this section, to realize the VMDM-based short-reach transmission with large capacity and high performance, I/Q modulation and KK receiver are introduced. In the following experiment, the second scheme in Fig.3.1 is adopted, where each wavelength channel carries 16-QAM signal and the LO is accordingly shifted to the edge of the spectrum of each WDM signal-light.

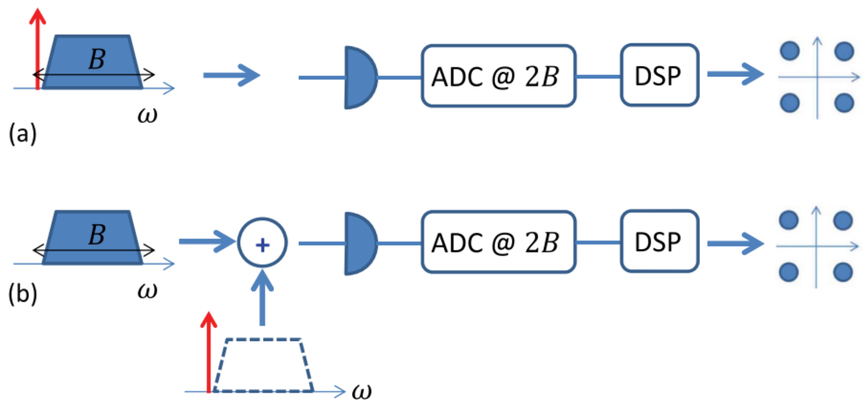

Figure 3.1: KK receiver with (a) digital carrier; (b) optical carrier[2].

3.1.2 Experimental setups and results of VM-based KK-receiver transmission over FMF link

Figure 3.2 shows the experimental setup for the generation and propagation of eigenmodes through the FMF described in the previous chapter. Firstly, the light beam is transformed to a homogeneous linearly polarized beam via PBS. After passing through the VWP, the light is converted to the VMs of $l = +2$ accordingly. After FMF propagation, another VWP is employed to convert the VM to the fundamental mode.

Here, the step-index FMF which supports the vector modes of HE11, TE01, HE21, TM01, HE31, EH11 and HE12 at 1550 nm is utilized for eigenmodes multiplexing

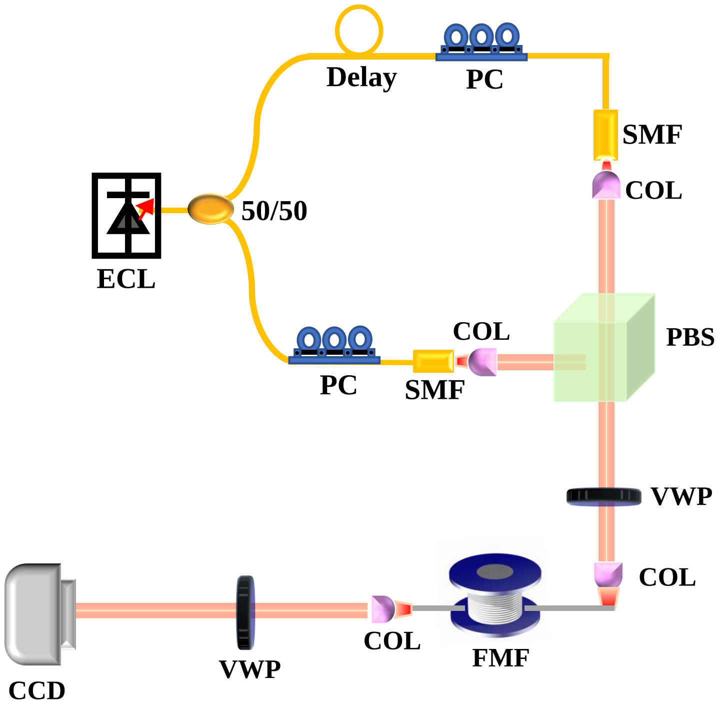

Figure 3.2: Generation and propagation of VM over 5 km FMF. ECL: external cavity laser; PC: polarization controller; SMF: single-mode fiber; COL: collimator; PBS: polarization beam splitter; VWP: vortex wave plate; FMF: few-mode fiber; CCD: charge-coupled device camera.

transmission as introduced in Chapter 2.3.1 in detail. n_{eff} of VMs of $l = 0$ and $l = +2$ (EH11 and HE11 modes) of the FMF at 1550 nm wavelength are illustrated in Fig.3.3 (a). As we can see, the effective refractive index difference Δn_{eff} between VMs of $l = 0$ and $l = +2$ is about 3×10^{-3}. Such relatively large Δn_{eff} indicates that low distributed mode coupling exists between the VMs of $l = 0$ and $l = +2$, when they are multiplexed and transmitted in the FMF. In order to characterize the propagation performance of these eigenmodes based on the VWP and FMF, we measure the crosstalk among four VMs after 5 km FMF transmission. The normalized mode crosstalk matrix is illustrated in Fig.3.3 (b). As we can see, the maximum mode isolation (MI) of VM channels between $l = 0$ and $l = +2$ is about 23.6 dB. For the VMs of $l = +2$, the MI larger than 21.1 dB can be obtained between odd and even modes. Accordingly, this large MI based on the FMF can be used to implement VMDM transmission.

The experiments of VMDM-based transmission over FMF link include three parts that respectively demonstrate two VMs of the same order ($l = +2$, EH11o and EH11e modes), two VMs of different orders ($l = 0$ and $l = +2$, HE11o and EH11e modes)

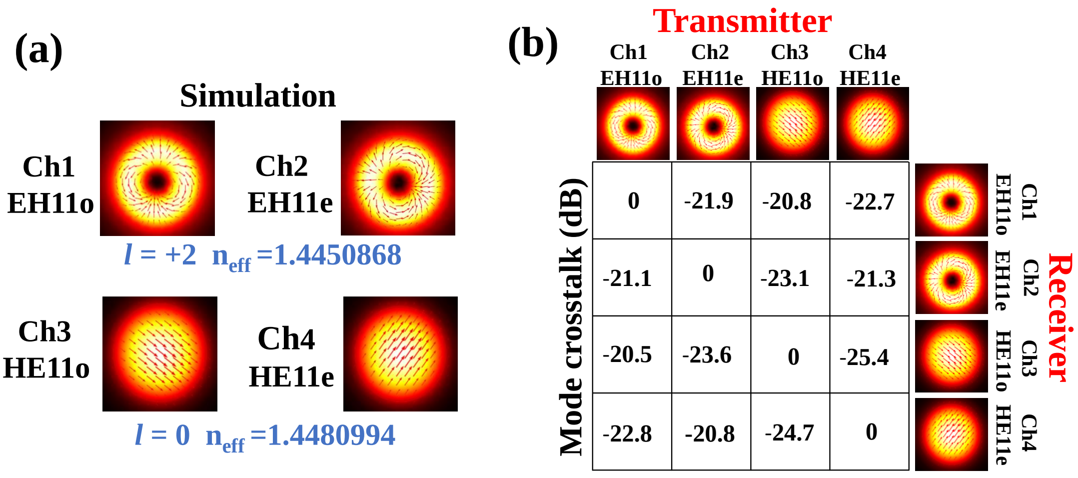

Figure 3.3: (a) Effective refractive index of the used vector modes of the FMF at 1550nm wavelength. (b) The normalized mode crosstalk matrix for four VM channels.

and two-VMs five-wavelength multiplexed signal transmissions over 5 km FMF. In the first experiment, EH11o and EH11e modes are employed as multiplexed channels and the experimental setup is shown in Fig.3.4. At the transmitter, the CW lightwave from the ECL (1550.12 nm) with 100 kHz linewidth is launched into an I/Q modulator (FUJITSU FTM7962EP) and modulated with 45 GBaud 16-QAM signal. This signal is shaped spectrally with a 0.02 roll-off factor (RF) raised-cosine (RC) filter and generated by an AWG (Keysight M8196A) with a 90 GSa/s sampling rate. The generated optical signal is then amplified by a low-noise EDFA to control the input power for the next multiplexing parts. In the VMDM part, the optical signal is divided into four branches via an OC. The PC in each branch is utilized to maximize the output power of horizontal and vertical light from PBS. Ch1 and Ch2 in Fig.3.4 are combined by a PBS as orthogonally polarized channels and are subsequently converted to EH11o and EH11e modes by VWP with $l = +2$. In the meantime, the collimated light beams of Ch3 and Ch4 in Fig.3.4 are directly converted to HE11o and HE11e modes via another PBS. Then, four branches are combined together by a NPBS.

Here, for the first demonstration, only Ch1 and Ch2 are used as multiplexed modes with Ch3 and Ch4 switched off. After generation and multiplexing, the light beam containing two VMs ($l = +2$) is aligned coaxially and a five-dimensional translational stage is used to adjust the position of the FMF to confirm the optimized angle when

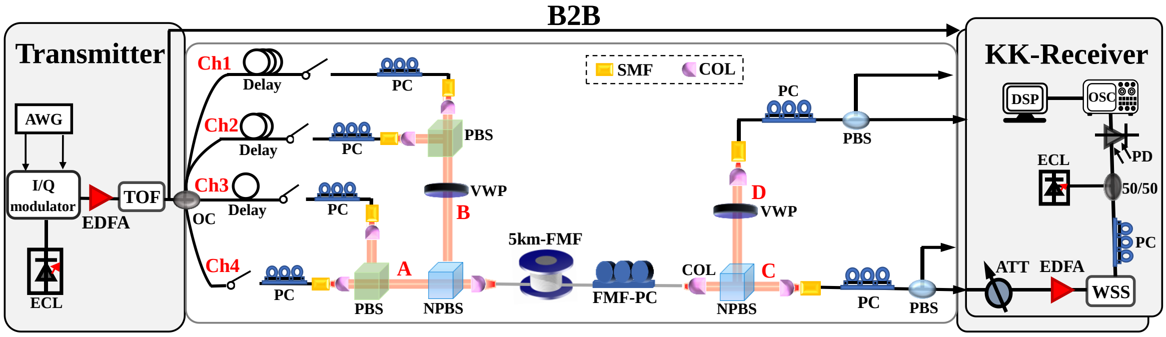

Figure 3.4: The experimental setup of the VM-based KK-receiver transmission over FMF link. AWG: arbitrary waveform generator; ECL: external cavity laser; EDFA: erbium-doped fiber amplifier; TOF: tunable optical fiber; OC: optical coupler; PC: polarization controller; COL: collimator; SMF: single-mode fiber; PBS: polarization beam splitter; VWP: vortex wave plate; NPBS: non-polarizing beam splitter; FMF: few-mode fiber; FMF-PC: FMF-based PC; ATT: attenuator; WSS: wavelength selective switch; PD: photo-detector; OSC: oscilloscope; DSP: digital signal processing, B2B: back-to-back.

incident modes are coupling into the FMF. In this link, just as common SMF-PC, an FMF-PC is used to adjust the polarization and intensity distribution of the output's beams[64]. When the FMF coupling parts are properly aligned, the FMF-PC is slightly adjusted until the mode crosstalk is minimized. After 5 km FMF transmission, VMDM signal is separated into two branches by another NPBS. One branch passing through another VWP is converted VMs back to the orthogonal fundamental modes before being collimated into the single-mode fiber. Subsequently, by rotating PC, the mutually orthogonal SOP can be separated via PBS. Another branch is coupled into the SMF directly to detect the VMs of $l = 0$ of the output beams. This branch is also prepared for de-multiplexing Ch3 and Ch4 for the second experiment.

At the receiver, the optical signal is attenuated by an ATT to change the ROP and then is amplified by the second EDFA operating at constant power output mode. After being filtered by a WSS, the received signal is coupled by an OC with a wavelength-tunable local carrier whose polarization is the same as the received signal controlled by PC and wavelength is set to around 1550.12 nm + 45 $\times$ (1+0.02)/2 GHz for KK reception. Before direct detection, the power of the local carrier is about 8 dBm and the power of the filtered optical signal is about 4 dBm adjusted by the second EDFA. This operation guarantees the coupled light with 12 dB CSPR which is practically sufficient to ensure the minimum phase property of KK relation. Finally, the electrical signal is detected by a 43 GHz PD and then sampled by a real-time OSC (Keysight DSAZ594A) at 160 GSa/s sampling rate and further processed by the offline DSP which includes the complex field reconstruction via KK relation, constant modulus algorithm (CMA) pre-equalization, radius directed equalization (RDE), frequency offset compensation, carrier phase recovery and BER decision. The aggregate raw bit rate of this system is 360 Gbit/s ($45 \times 4 \times 2 = 360$ Gbit/s). In the second experiment, EH11e mode of Ch2 and HE11o mode of Ch3 are employed in the VMDM transmission. Due to the largest mode isolation of these two modes, 50 GBaud 16-QAM signal with 0.02 RF RC filter is modulated on the used VMs. In the multiplexed parts, Ch2 in Fig.**3.4** is converted to EH11e mode after passing through PBS and VWP. Ch3 is directly converted to the HE11o mode by another PBS. Subsequently, two branches are multiplexed by a NPBS and coupled into the same 5 km FMF. After transmission, the output beams are divided into two parts by a NPBS. One part is fed into the SMF directly to filter higher-order VMs and HE11o mode can be detected. In another part, EH11e mode is demodulated by the second VWP. Meanwhile, HE11o mode is transformed into higher-order VM which cannot be coupled into SMF. In this way, Ch2 and Ch3 can be separated successfully. And these two detected signals are respectively sent to the KK receiver part for sampling and offline DSP. The total raw bit rate of this transmission scenario is 400 Gbit/s ($50 \times 4 \times 2 = 400$ Gbit/s).

Figure **3.5** illustrates the intensity patterns of the VMs ($l = 0$ and $l = +2$) of labeled points in Fig.**3.4** captured by the CCD camera. According to Eq.**(2.15)**, the Jones vector of EH11 modes can be expressed as: $(\cos 2\varphi \ \sin 2\varphi)^{\mathrm{T}}$ and $(\sin 2\varphi \ {-\cos 2\varphi})^{\mathrm{T}}$. Thus, when EH11 modes pass through a linear polarizer which only allows one linear SoP to pass, four lobes will be observed. In addition, by rotating the polarizer in front of CCD, the polarization distribution of each vector mode channel is observed. Fig.**3.5** (a), (b), (m) and (n) illustrate the four input VM channels and Fig.**3.5** (c), (d), (o) and (p) show the four output VM channels after 5 km FMF link. Fig.**3.5** (e), (f), (q) and (r) depict the patterns of these output VM channels after passing through the second VWP. Fig.**3.5** (g-l) show the SOP of the corresponding channels. As we can see, there are slight differences between the captured patterns before and after 5 km

FMF propagation.

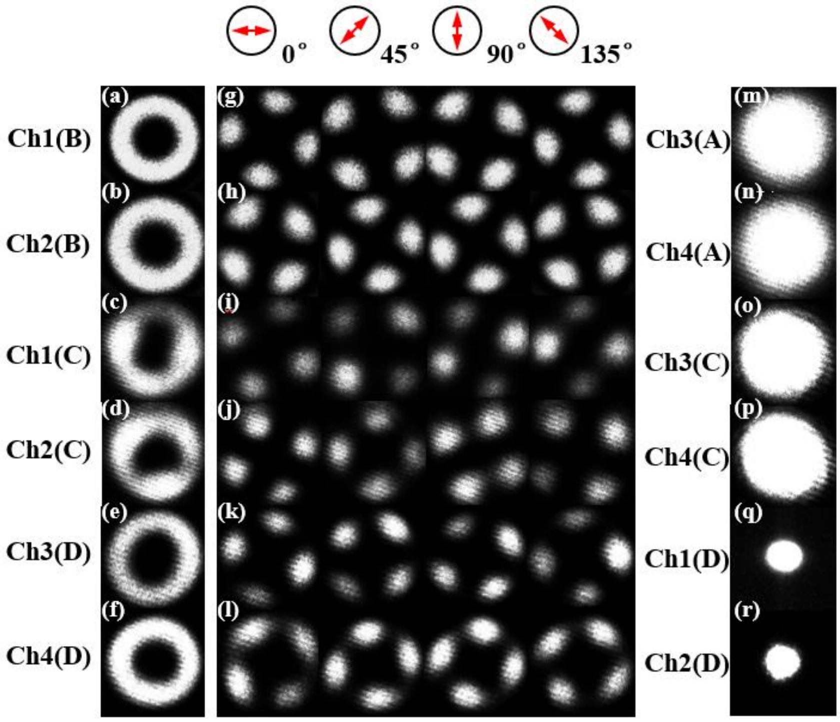

Figure 3.5: The intensity profiles of four channels of labeled points in Fig. 3.4 captured by CCD camera. The arrows indicate the orientations of the transmission axis of the polarizer.

To further evaluate the transmission performance for the above two experiments, the BER property versus ROP is evaluated for both single VM and multiplexed VMs scenarios. The experimental results are respectively shown in Fig.3.6 and Fig.3.7. When two channels of EH11o and EH11e are transmitted, 6.2 dB and 5.4 dB power penalties are induced between the B2B channel and VM channels respectively under the FEC threshold at 3.8×10^{-3}. In B2B transmission, the optical signal is directly injected into the receiver without propagating through the multiplexing system. Insets (I) and (II) of Fig.3.6 illustrate the constellations of the demodulated 16-QAM signal of EH11o and EH11e channels simultaneously propagating over FMF at the ROP of –16 dBm, respectively. In the second demonstration, both power penalties of HE11o and EH11e channels are 5.4 dB when the HE11o and EH11e modes are transmitted simultaneously. The constellations for HE11o and EH11e channels at the ROP of –16dBm are shown in the Insets (I) and (II) of Fig.3.7, respectively.

In the final experiment, WDM is introduced into the VMDM system to further boost

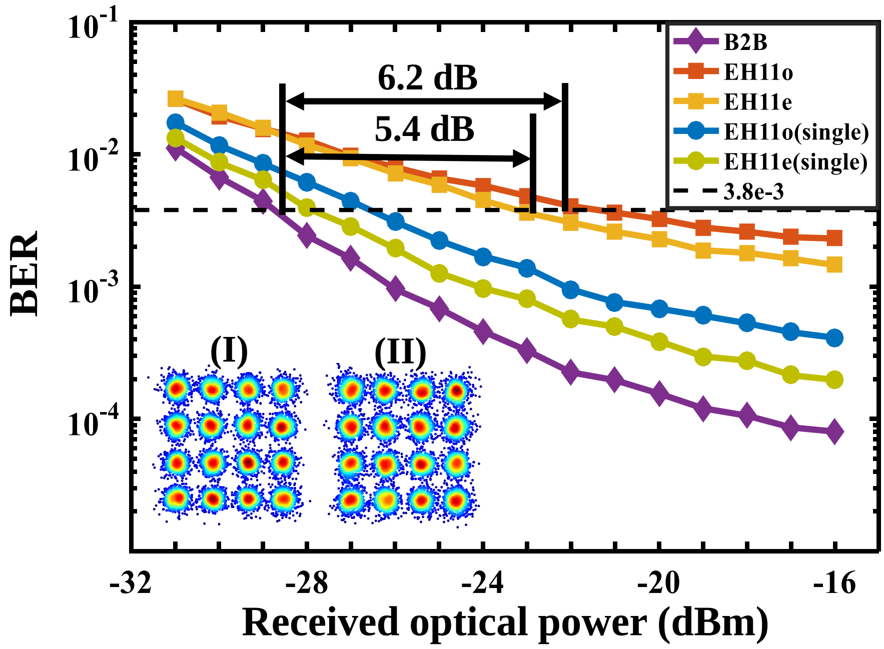

Figure 3.6: BER versus ROP of 45 GBaud 16-QAM over EH11o and EH11e channels.

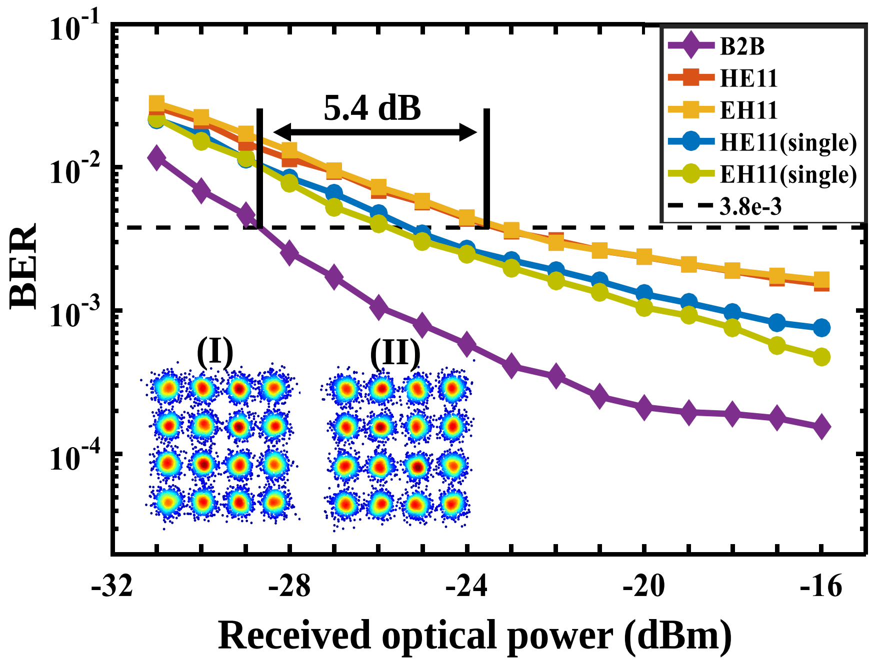

Figure 3.7: BER versus ROP of 50 GBaud 16-QAM over EH11 and HE11 channels.

the transmission capacity. The experiment system of two-dimensional VMDM-WDM is illustrated in Fig. 3.8.

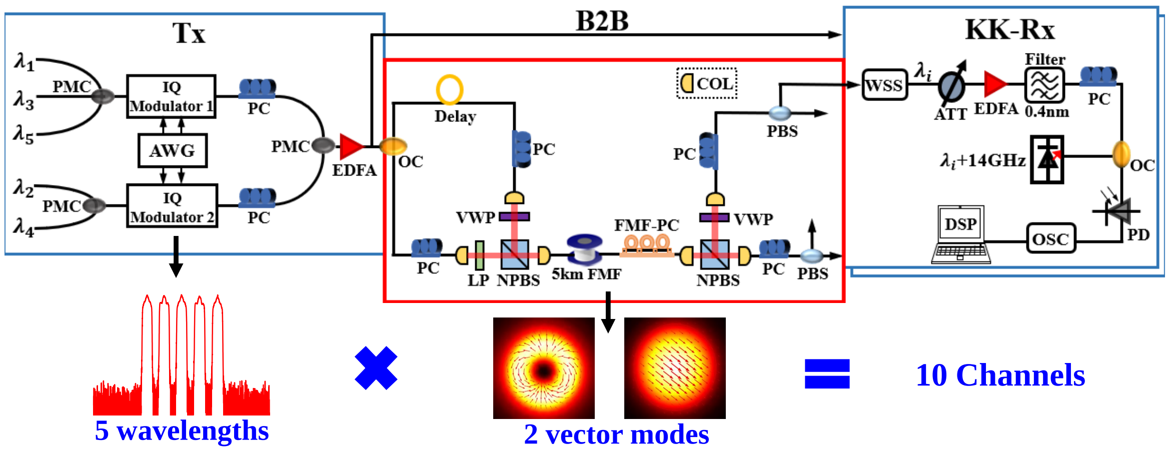

Figure 3.8: The experimental setup of VMDM-WDM transmission system based on KK-receiver over 5 km FMF link.

At the transmitter, five optical carriers (ranging from 1549.32 nm to 1550.92 nm, λ_1-λ_5) from ECLs (100 kHz linewidth) with a wavelength interval of 0.4 nm are adopted as the WDM channels. The odd carriers (λ_1, λ_3 and λ_5) and even carriers (λ_2 andλ_4) are respectively modulated by two I/Q modulators, which are driven by two independent 28 GBaud 16-QAM sequences using a raised-cosine filter with a roll-off factor of 0.1 from an AWG (Keysight M8196A) at 84 GSa/s sampling rate. Then, five optical channels are combined by a polarization-maintaining fiber coupler (PMC), amplified by an EDFA, and then split into two branches with an OC. One branch is converted to HE11 mode after passing through a linear polarizer. By employing the VWP, another branch of these carriers is converted to EH11 mode. Two PCs are used to maximize output power of both branches. Subsequently, two branches are multiplexed by a NPBS and coupled into the 5 km FMF link. After transmission, the output beams are divided into two parts by another NPBS. One part is fed into the SMF directly to filter EH11 mode. In the other part, EH11 mode is transformed back into the fundamental mode after passing through the second VWP. Meanwhile, HE11 mode is converted to higher-order VM which cannot be coupled into SMF. Consequently, two VM channels can be separated successfully by this method. The PBS is used to further reduce the mode crosstalk. Fig.3.9 shows the intensity profiles of two VMs captured by the CCD camera before ((A) and (B)) and after ((C) and (D)) 5 km FMF transmission, respectively. By rotating the polarizer after the EH11 mode, observe the polarization distribution of EH11 mode channel can be observed, which are shown in the Fig.3.9 (a)(A_1)/(C_1). The measured crosstalk of two VMs is shown in Fig.3.10 (c). As can be seen that the minimum isolation is approximately 21.7 dB between the two mode channels.

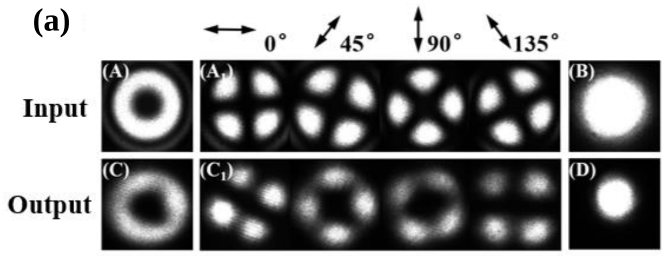

(b) **Mode crosstalk (dB)**

Rx \ Tx	HE11	EH11
HE11	0	-21.7
EH11	-22.9	0

Figure 3.9: The intensity profiles of multiplexed VMs before ((A) and (B)) and after ((C) and (D)) transmission over 5 km FMF, respectively. Insets (A_1) and (C_1): The polarization distribution of EH11 channel with the polarizer. (c) Measured crosstalk matrix for two VM channels over 5 km FMF.

At the receiver, λ_i, one of the five WDM channels, is selected by WSS to evaluate its transmission performance. The subsequent optical ATT is used to adjust the ROP. After being amplified by an EDFA and filtered by a 0.4 nm optical filter, the received optical signal is then coupled by an OC with the local carrier (frequency shift of λ_i approximate 15 GHz) for KK reception. Before direct detection, the CSPR is set to 12.5 dB which is sufficient to ensure the minimum phase property of KK relation. After being detected by a 43 GHz PD, the electrical waveform is sampled by a real-time OSC at 160 GSa/s sampling rate and then processed by offline DSP.

The measured transmission performance of VMDM-WDM is shown in Fig.3.10. As illustrated in Fig.3.10 (a), the measured BER performance of 10 channels (two vector modes $\times$ five wavelengths) are below the 7% FEC limit of 3.8×10^{-3} at the ROP of -20 dBm. The inset (I) of Fig.3.10 (a) depicts the optical spectrum of the five WDM channels. Then, without loss of the generality, the BER performance versus ROP of one wavelength channel at 1550.12 nm is measured, plotted in Fig.3.10 (b). The performance of the fundamental HE11 mode is better than the higher-order EH11 mode due to the lower mode crosstalk. There are 4 dB and 6.4 dB power penalties between the B2B and vector mode channels respectively under the FEC limit. Insets (I) and (II) of Fig.3.10 (b) show the constellations of HE11 and EH11 channels (1550.12 nm) respectively at -20 dBm ROP after 5 km FMF transmission. To the best of our knowledge, this is the highest data rate of vector mode division multiplexing demonstration over several kilometers FMF (10 parallel channels with a total data rate of 1.12 Tbit/s ($28 \times 4 \times 2 \times 5 = 1.12$ Tbit/s)). This realization would pave the way for high-speed large-capacity short-reach optical interconnect, such as next-generation 800 G or 1 T and beyond DCI.

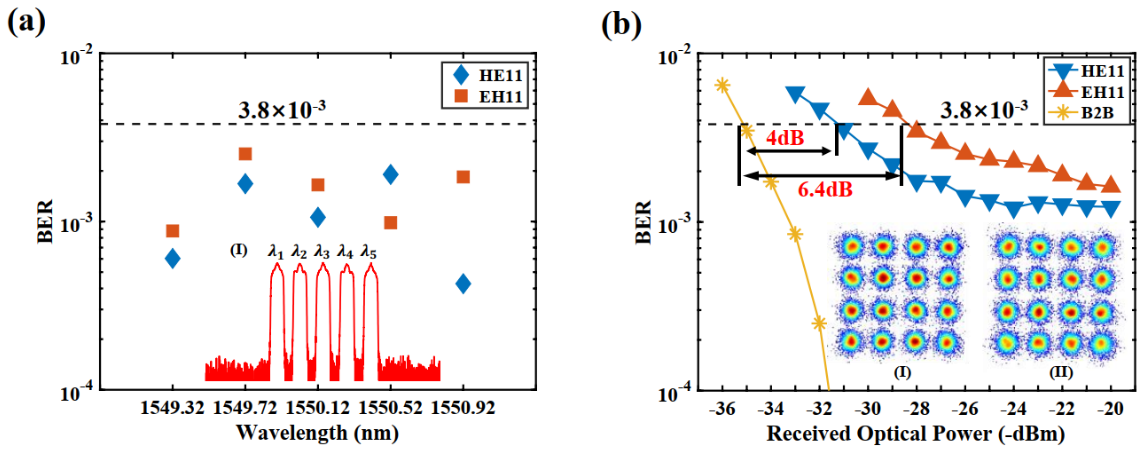

Figure 3.10: BER performance of all 10 channels (ROP = -20 dBm). (b) BER performance versus ROP at 1550.12 nm.

3.2 Fiber Vector Eigenmode multiplexing Based Bi-directional full-duplex transmission

3.2.1 Bi-directional passive optical network

Over the past few decades, the advent of Internet of things (IoT), the evolution of bandwidth-hungry applications and the surge of global IP traffic have fueled the demands for high-speed high-capacity optical communication. Such a fast-changing environment needs advanced optical access networks which keep pace with the ever rapid-growing bandwidth demand. Currently, practical passive optical network (PON) which adopts a point-to-multipoint framework is widely viewed as a suitable scheme for optical access networks. Due to technological and commercial maturity, protocol transparency and high security, WDM-based PON is generally regarded as the most promising solution for the next generation access network[65,66], where every optical network unit (ONU) is allocated certain wavelength. However, the scalability of WDM-based PON is subject to the limited bandwidth resource. On the other hand, it is worth noting that, PON is a typical bi-directional communication system case, in which Rayleigh back scattering (RB) and Fresnel reflection (FR) that are the intrinsic processes of fibers will inevitably degrade the system performance[67–70]. In order to alleviate RB and FR effects, various bi-directional schemes have been proposed, such as wavelength offset detuning[71,72], frequency dithering[73,74], cross-remodulation schemes[75,76] and time-division-duplexing[77,78]. However, the performance upgradation based on these scenarios requires extra bandwidth or extra laser sources or time-sharing basis, which will definitely result in low SE and resource-wasting. Undoubtedly, future fiber-optic network is expected to achieve higher performance, higher capacity, and higher bandwidth utilization. Recently, in order to further improve the scale of PON, hybrid-PON architecture introducing some other multiplexing granularity to accommodate more and more ONUs comes to people's sight and might be an alternative solution in the future. Thus, SDM/MDM-based bi-directional transmission merits more focus. In addition, compared to conventional PON schemes, SDM/MDM-based PONs enable the reduction of power consumption and SE, which provides cost advantages for commercial applications. Although there have been several works that demonstrate the feasibility of LP/OAM-based MDM bi-directional links[79–81], the system limitation and optimization are not widely investigated and discussed.

In this section, by using the direct fiber eigenmodes, vector modes, two full-duplex full-polarization bi-directional architectures of homo-VMs and hetero-VMs transmitted in two directions over 3 km FMF is respectively experimentally demonstrated. The degradation caused by crosstalk due to RB and FR in the FMF under homo-modal link is evaluated and analyzed. To strengthen the immunity to RB and FR of systems, a simple and effective approach by utilizing the hetero-modes on two ends of bi-directional transmission is proposed. Then, a 448 Gbit/s full-duplex bi-directional

VMDM link with 28 GBaud 16-QAM is demonstrated, in which two VMs of $l = 0$ and two VMs of $l = +2$ are respectively loaded in the uplink and downlink with isolation between counter direction larger than 19 dB using a 9-tap 2×2 MIMO equalizer. Moreover, also based on this scheme, a 1.792 Tbit/s WDM-MDM full-duplex bi-directional link is successfully realized. All experimental results meet the 7% HD-FEC BER of 3.8×10^{-3}, demonstrating that the proposed hetero-modal scheme could be a competitive candidate for future high-SE high-capacity bi-directional transmission link.

3.2.2 Experimental setups and results of Full-duplex Homo-VMs based MDM bi-directional transmission

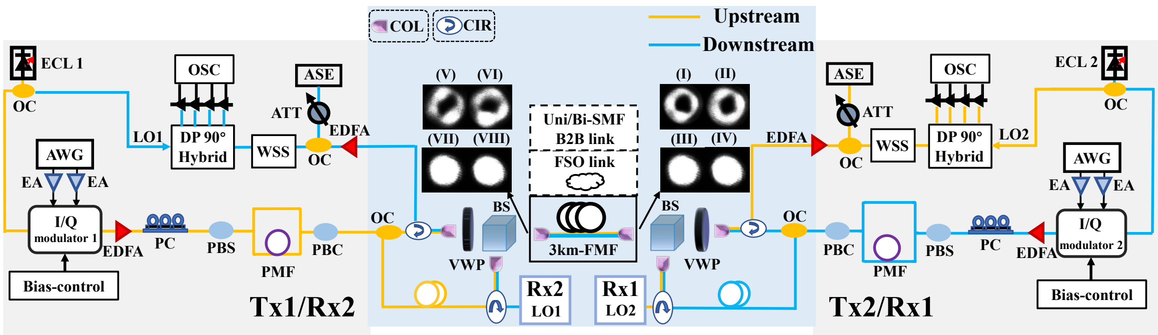

Figure 3.11: The experimental setup of full-duplex homo-VMs based MDM bi-directional transmission. AWG: arbitrary waveform generator; EA: electrical amplifier; ECL: external cavity laser; OC: optical coupler; EDFA: erbium-doped fiber amplifier; PC: polarization controller; PBS: polarization beam splitter; PBC: polarization beam combiner; PMF: polarization maintaining fiber; CIR: circulator; COL: collimator; VWP: vortex wave plate; BS: beam splitter; FMF: few-mode fiber; ATT: attenuator; WSS: wavelength selective switch; ASE: amplifier spontaneous-emission noise; OSC: oscilloscope; LO: local oscillator; B2B: back-to-back; FSO: free space optical.

Figure 3.11 illustrates the homo-mode based full-duplex bi-directional transmission over 3 km FMF, in which identical four VMs are transmitted on both uplink and downlink. At each transmitter (Tx1/Tx2), the CW light-wave from the ECL (1550.12 nm, ~100 kHz linewidth) is split into two branches by a 1:1 OC. One branch is used as the LO for the opposite transmission signal by coherent detection. Another branch is fed into the I/Q modulator driven by the 14 GBaud QPSK signal, which is shaped spectrally with a 0.5 roll-off factor (RF) raised-cosine (RC) filter and generated by an arbitrary waveform generator (AWG, Keysight M8196A), operating at 84 GSa/s sampling rate. After amplified by an EDFA, PDM is emulated by PBS and PBC. The

PC after EDFA is utilized to balance the power of horizontal and vertical light beams of PDM. Then, the mutually orthogonal signals are split into two parts by a 1:1 OC. One is employed to generate VMs of $l = +2$ (EH_{11o} and EH_{11e} modes) by VWP and another is directly employed as VMs of $l = 0$ (HE_{11o} and HE_{11e} modes). Next, four VMs are multiplexed together by a BS and coupled into the 3 km FMF through a COL. Here, the fiber coupling loss is about 3 dB including the COL. The used step-index FMF with the transmission loss of about 0.25 dB/km has been introduced in Chapter 2.3.1 in detail. The effective refractive index difference Δn_{eff} between VM of $l = 0$ and $l = +2$ is around 3×10^{-3}. Such relatively large Δn_{eff} indicates that the couplings between VMs of $l = 0$ and $l = +2$ are low when they are multiplexed and transmitted in this FMF. In the FMF link, a FMF-based PC (FMF-PC) is utilized to adjust the polarization and intensity distribution of the output beams for the optimal pattern. In Fig.**3.11**, insets (I) to (IV) and (V) to (VIII) respectively show the captured intensity profiles of uplink and downlink for VM channels after 3 km FMF transmission. After full-duplex fiber transmission, the light beams are separated into two parts by another BS. One branch is directly fed into the SMF to filter higher-order VMs and only VMs of $l = 0$ with mutually orthogonal SoPs can be detected. In another branch, VMs of $l = +2$ are converted back to the orthogonal fundamental modes after passing through the VWP. Meanwhile, VMs of $l = 0$ are transferred to higher-order VMs that cannot be coupled into SMF. In this way, VMs of $l = 0$ and $l = +2$ are separated and are sent to the corresponding receiver. At each receiver (Rx1/Rx2), dual-polarized signals and LO are sent to DP 90° hybrid for coherent detection after a circulator (CIR). The laser of Tx2/Tx1 can be served as LO in Rx1/Rx2 for the sake of the same wavelength used in both ends. Then, four electrically-received signals after four balanced PDs go through the offline DSP which accordingly includes resampling, fractionally-spaced 2×2 constant modulus algorithm (CMA) for adaptively demultiplexing and equalizing of dual-polarized signals[82], frequency offset estimation using the periodogram of the 4th power of equalized signals[83], carrier phase recovery, BER calculation and signal-noise ratio (SNR) calculation. Here, the number of taps in CMA is set to 5, which is enough for the differential group delay (DGD) compensation and other inter-symbol interference (ISI) within same order VMs after 3 km FMF transmission.

Figure 3.12 shows the measured crosstalk of two used VM MGs in this full-duplex system based on the power measurement, including uni-directional crosstalk and bi-directional crosstalk. For uni-directional transmission, the isolation between the two VM MGs of uni-directional is larger than 18.5 dB. Inter-modal crosstalk could be introduced when VMs are coupling into FMF from free space, because it is hard to realize perfect vertical incidence. Besides, channel crosstalk may be caused by fiber perturbation and imperfection, which could further lead to mode degradation. For bi-directional link, except for uni-directional crosstalk mentioned before, counterpropagating signals of the same wavelength and homo-mode unavoidably suffer severe deterioration. In the experiment, crosstalk caused by RB is very small due to short-reach FMF. FR, especially connector (FC/PC, made of ourselves) reflection, is mainly accountable for crosstalk between the same modes in the counter direction. As it can be seen, the measured bi-directional crosstalk from the counter direction is less than −13.8 dB, which is the major impairment for the whole system.

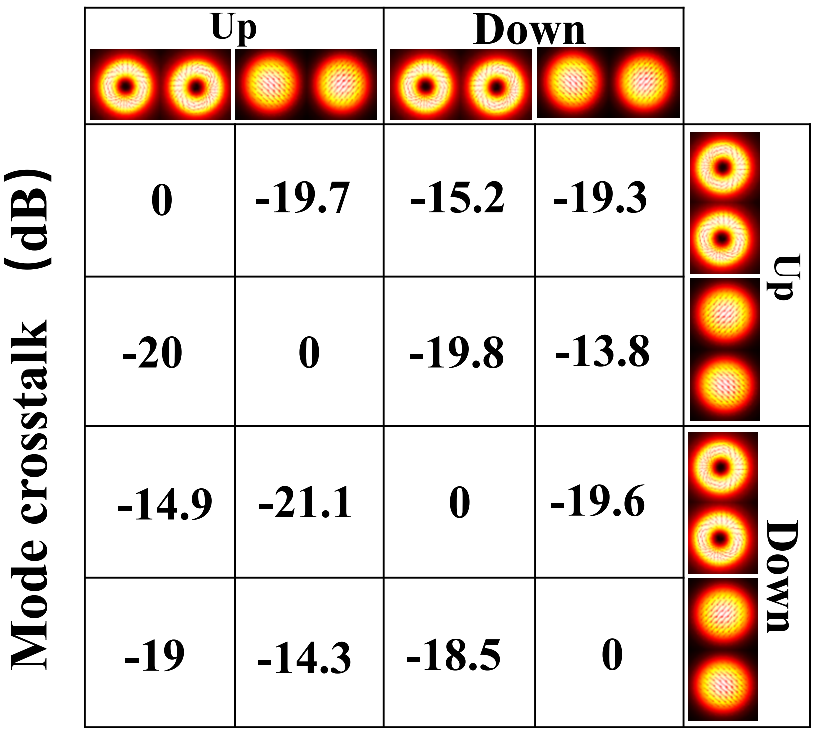

Figure 3.12: The normalized mode crosstalk matrix for such full-duplex VMDM bi-directional system.

To further evaluate the transmission performance of this VMDM-based bi-directional system, the BER property versus the OSNR is measured under SMF B2B, bi-directional SMF B2B, bi-directional FSO and bi-directional FMF link cases, respectively. Here, the B2B case is the DP signals are directly sent to the receiver. The measured BER performance of DP signals for VMs of $l = 0$ and $l = +2$ under uplink (BiU0/BiU2) and downlink (BiD0/BiD2) transmission are plotted with up-pointing triangles and down-pointing triangles, respectively, in Fig.**3.13**, using 14 GBaud QPSK for each mode with the aggregate capacity of 224 Gbit/s ($14 \times 2 \times 4 \times 2$ (directions) = 224 Gbit/s). The BER performance of VMs of $l = 0$ is always better than that of VMs of $l = +2$ under two cases. Compared with uni/bi-directional B2B and bi-directional FSO links (empty/filled circles and empty triangles in Fig.**3.13**), the power penalties for uplink and downlink are respectively about 6/6/5 dB and 5/5/4 dB of VMs of $l = 0$ under the 7% hard decision FEC threshold of 3.8×10^{-3} BER. As for VMs of $l = +2$, the power penalties are about 8/8/6.5 dB and 8.5/8.5/7 dB respectively for uplink and downlink at BER of 3.8×10^{-3}. Such penalties are mainly induced by back crosstalk, which is also the key limitation of system capacity. As for the uni-bidirectional transmission, the system crosstalk is less than -18.5 dB according to Fig.**3.12**, which is much less than the back crosstalk. In order to evaluate the system impact of crosstalk, higher order modulation format of 16-QAM signal with the same GBaud rate of 14 GBaud is loaded on each mode channel in such uni-bidirectional link. The BER properties of four mode channels versus the OSNR are also measured, which are shown in Fig.**3.14**. Compared with the B2B scenario, 4 dB and 4.5 dB power penalties are induced for HE11 ($l = 0$) and EH11 ($l = 2$) channels respectively under the FEC threshold at 3.8×10^{-3}.

In order to suppress the back crosstalk of bi-directional system, wavelength offset detuning[71,72] is a simple and general method, in which wavelengths transmission in opposite directions are sufficiently spaced to alleviate RB and FR effects. Here, to verify the impact of wavelengths offset for VMDM bi-directional link, the wavelength of VM channels in uplink and downlink are respectively adjusted. It is noted that only

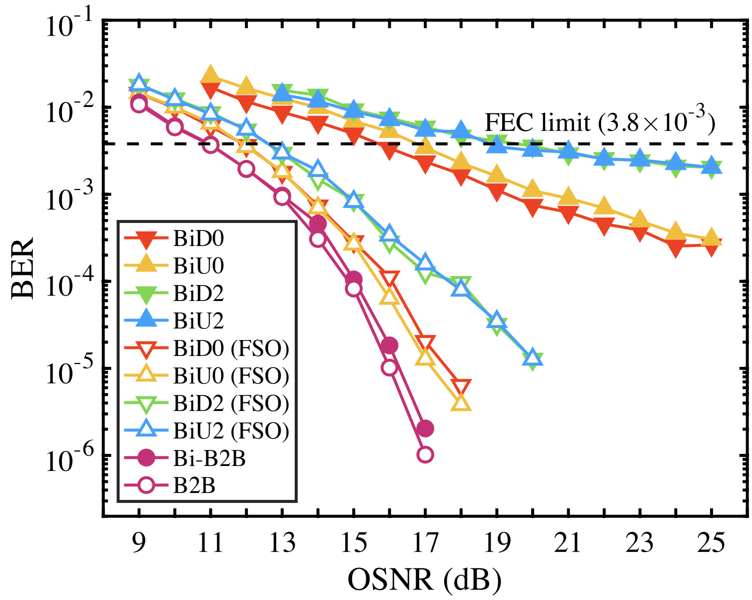

Figure 3.13: Measured BER versus OSNR of 14 GBaud QPSK signal for four homo-VMs based MDM bi-directional transmission over 3 km FMF.

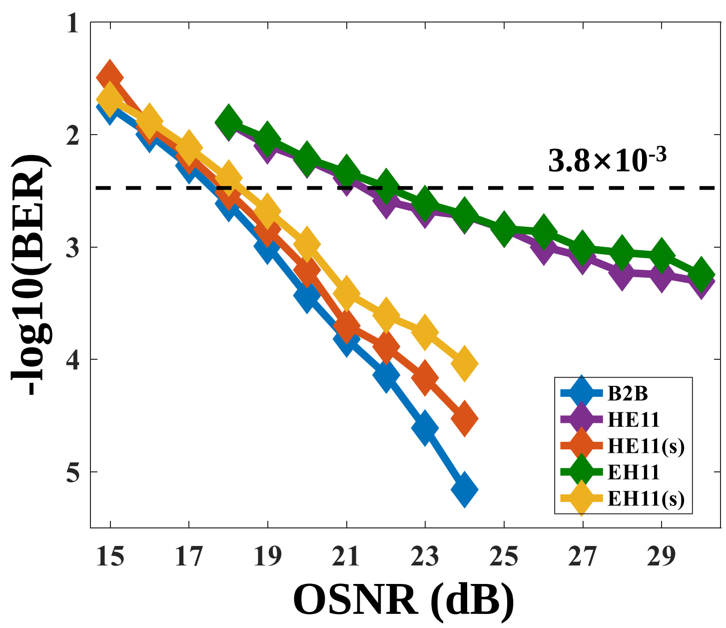

Figure 3.14: Measured BER versus OSNR of 14 GBaud 16-QAM signal for four-VM-multiplexing uni-bidirectional transmission over 3 km FMF.

one identical VM MG in each end is transmitted each time to exclude impacts from other interferences. Fig.3.15 plots the calculated SNR as a function of wavelength offset when two VMs of $l = 0$ or $l = +2$ are transmitted bi-directionally. We can find that SNR is significantly improved when the wavelength offset is larger than the signal's bandwidth $14 \times (1 + 0.5) = 21$ GHz ($\sim$0.168 nm).

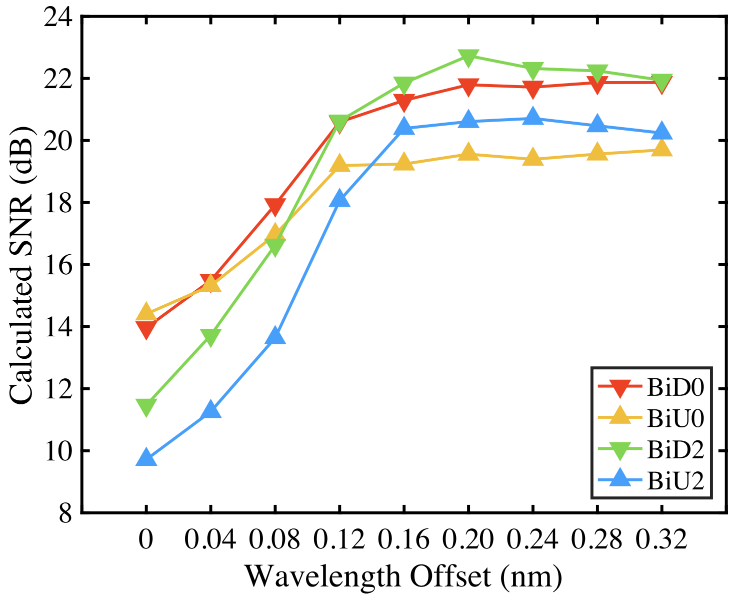

Figure 3.15: Calculated SNR performance versus wavelength offset when VMs of $l = 0$ or $l = +2$ are transmitted bi-directionally.

For bi-directional transmission, with the implementation of the same wavelengths and modes, counterpropagating signals suffer from back crosstalk. In the wavelength detuning scheme, the performance improvement is based on extra bandwidth, which will result in low SE. Admittedly, hetero-mode full-duplex architecture is also a kind of wasting the space dimension. Nevertheless, the hetero-mode architecture is a better choice. First, it enables wavelength dimension to be fully utilized. Compared with space dimension, wavelength dimension is now more scalable and mature. Second, for coherent detection with higher SE, the same wavelength in the uplink and downlink can be utilized as LO for counter direction at the Rx. On the contrary, this wavelength detuning scheme requires extra laser source as LO, leading to extra cost or complexity. In addition, this scheme is at the price of extra bandwidth requirement, which will no longer satisfy future bandwidth-hungry applications in full-duplex WDM-PON. Thus, hetero-mode same-wavelength scheme is a suitable tradeoff.

3.2.3 Experimental setups and results of Full-duplex Hetero-VMs based MDM bi-directional transmission

To further enhance system immunity to opposite-directional signal degradation, a simple and effective scheme by employing hetero-VMs on two ends of bi-directional transmission is demonstrated. The experimental setup of full-duplex hetero-VMs based MDM bi-directional link is also based on Fig.3.11 and the simplified schematic diagram is shown in Fig.3.16. Here, two VMs of $l = +2$ and two VMs of $l = 0$ are respectively employed in the uplink and downlink. As it can be seen in Fig.3.12, the bi-directional crosstalk for hetero-VMs MGs is less than -19 dB. Accordingly, 28 GBaud 16-QAM signals with 0.1 RF RC filter are modulated on the used VMs on two terminals. At the receiver, different from DSP for homo bi-directional QPSK signal in Chapter 3.4.2, 2×2 CMA is only used for pre-equalization in-tandem with a 2×2 radius directed equalizer (RDE) performed for further adaptive equalization of 16-QAM signal[84]. The number of taps used for CMA and RDE are both set to 9, which, for a fair comparison, covers the same ISI duration as 5 taps in 14 GBaud QPSK in Chapter 3.4.2.

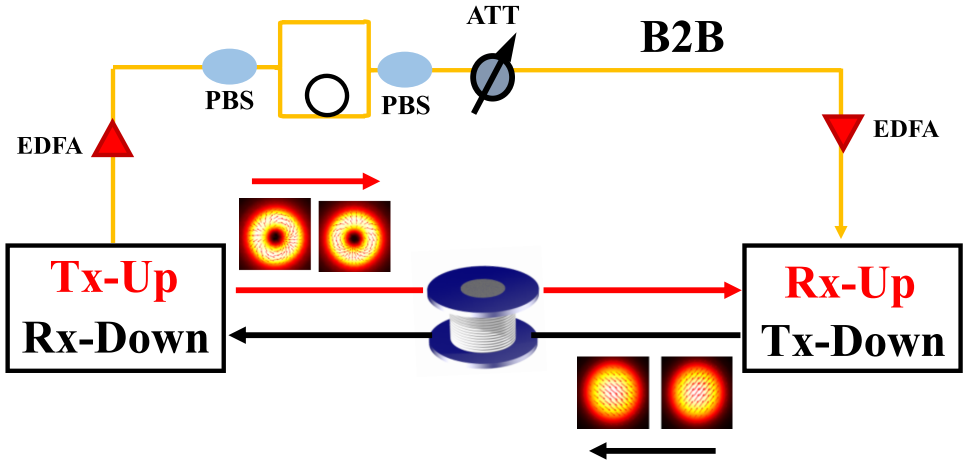

Figure 3.16: Schematic diagram of full-duplex hetero-VMs based MDM bi-directional link.

Then, the BER performance over a single wavelength (1550.12 nm) bi/uni-directional transmission with uni-directional SMF B2B transmission carrying DP signals is evaluated for comparison. The BER versus OSNR of used VM MGs for bi/uni-direction is plotted with triangles/circles in Fig.3.17. There is about 1.1 dB/1.3 dB power penalty between the uni-directional uplink (UniU2) /downlink (UniD0) and B2B (empty circles in Fig.3.17). Under bi-directional transmission, there are just around 3.8 dB and 4 dB power penalties for uplink (BiU2) and downlink (BiD0) referring to uni-directional SMF B2B, respectively. The constellation diagrams of the demodulated 16-QAM signals for full-duplex uplink and downlink at the OSNR of 32 dB are shown in Fig.3.17 (I) and (II), respectively. The data capacity of this demonstration is 448 Gbit/s ($28 \times 4 \times 2 \times 2$ (directions) = 448 Gbit/s). Compared with the former homo-modal scheme, the hetero-modal scheme doubles the overall data capacity of bi-directional transmission enabling a higher baud-rate (28 GBaud) and higher modulation format (16-QAM), which indicates this scheme can be further applied to longer distance fiber-optic transmission.

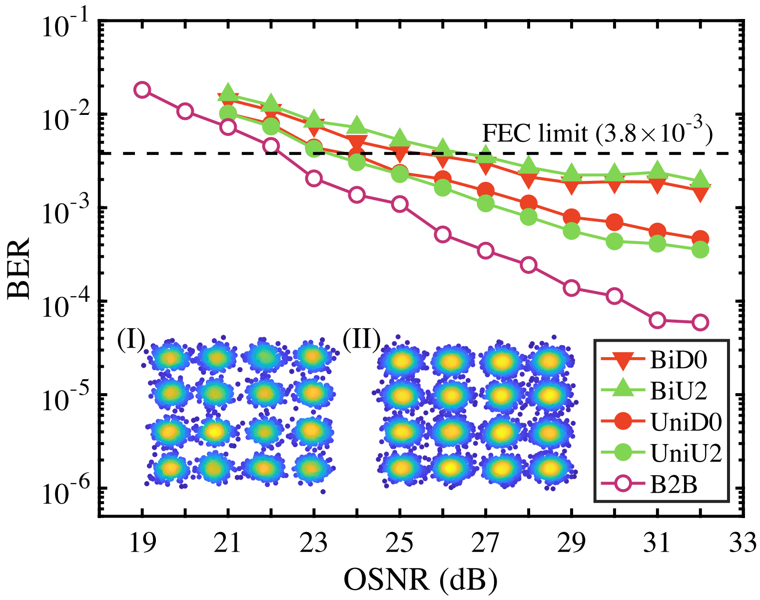

Figure 3.17: Measured BER versus OSNR of 28 GBaud 16-QAM signal for hetero-VMs based MDM bi-directional transmission.

Hetero-modal scheme is also compatible with the existing WDM systems and enables the wavelength resource to be fully explored. To further demonstrate the reliability and feasibility of the proposed hetero-VMs based bi-directional scheme, we therefore conduct the hetero-VMs WDM bi-directional system. Figure 3.18 shows the schematic of full-duplex hetero-VMs based MDM-WDM transmission. In this configuration, at each transmitter 4 wavelengths (ranging from 1549.72 nm to 1550.92 nm, λ_1 to λ_4) from 4 ECLs (~100 kHz linewidth) in a 0.4 nm/50 GHz grid are combined by a wavelength division multiplexer. Then, 4 optical carriers are modulated by 28 GBaud 16-QAM signal using a RC filter with a RF of 0.1. PDM for the generated signal is enabled by a PDM emulator. Subsequently, by employing VWP, uplink beams are converted to the VMs of $l = +2$ and then coupled into the FMF after a BS. Downlink beams are directly employed as VMs of $l = 0$ and are coupled into FMF.

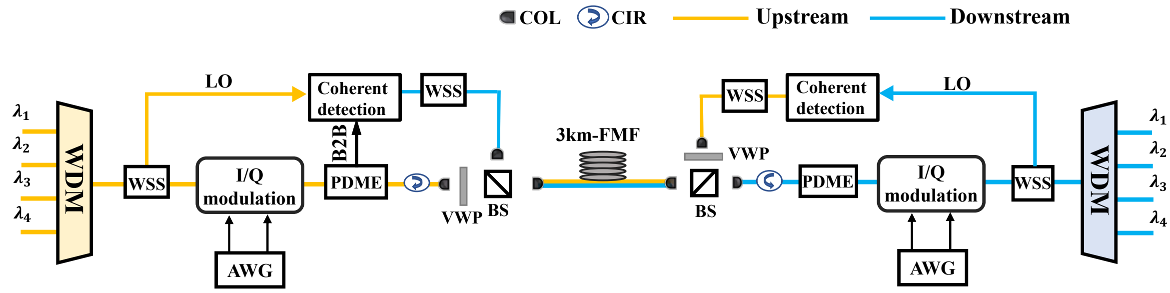

Figure 3.18: The experimental setup of full-duplex hetero-VMs based MDM-WDM bi-directional transmission.

After 3 km full-duplex FMF transmission, followed by the BS, uplink beams are converted back to the orthogonal polarizations by another VWP for detection. Meanwhile, downlink beams can be directly sent to the receiver for coherent detection. At each receiver, LO and signals from the opposite direction are filtered accordingly by wavelength selective switch (WSS) and then are sent to the receiver for coherent detection and DSP.

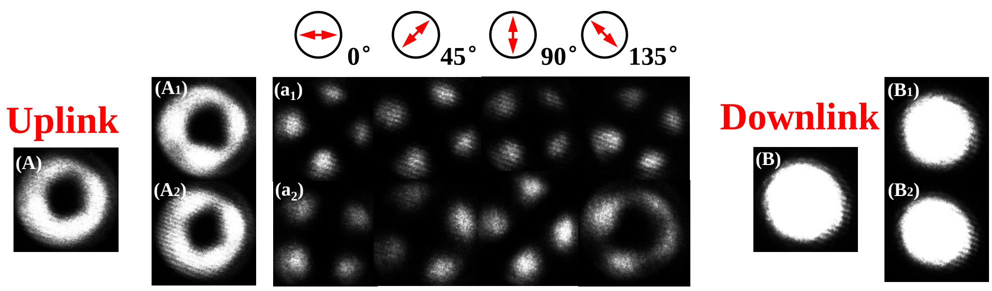

Figure 3.19: The intensity profiles of mode channels of uplink/downlink after 3 km FMF transmission. The arrows represent the direction of the polarizer.

Insets (A)/(B) in Fig.3.19 show the captured intensity profiles of uplink/downlink output beams after 3 km FMF transmission. Meanwhile, Insets (A_1) and (A_2)/(B_1) and (B_2) in Fig.3.19 respectively show the single mode channel of uplink/downlink after 3 km FMF transmission. As for two higher-order VM channels of uplink, insets (a_1) and (a_2) in Fig.3.19 respectively show the SoP distribution of the corresponding channels.

The BER performance for bi/uni-directional transmission is shown in Fig.3.20. The inset (I) of Fig.3.20 depicts the corresponding optical spectrum of the 4 WDM channels of 28 GBaud 16-QAM. It can be seen that the BER values of VMs of $l = +2$ (uplink) and VMs of $l = 0$ (downlink) at 4 different wavelengths are all below the FEC threshold of 3.8×10^{-3} with the total capacity of 1.792 Tbit/s (28×4×2×4×2 (directions) = 1.792 Tbit/s). This realization further indicates that this scheme exhibits robust performance and presents powerful extensibility. What's more, with the development of specially-designed FMF/MMF for VM and OAM and the corresponding mode multiplexer/de-multiplexer, bi-directional MDM link with more mode channels could be realized and it is a powerful candidate for future full-duplex PON with the requirement of high-capacity.

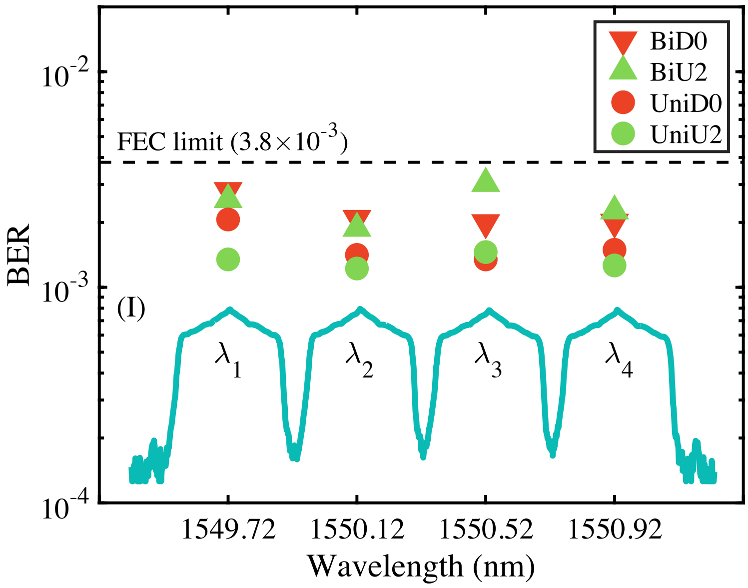

Figure 3.20: Measured BER performance of all 16 channels for MDM-WDM bi-directional transmission.

3.3 Summary

There are two main works in this chapter, which are all involved to vector-eigenmode based MDM fiber-optic communication systems. First, two VMs of the same order (EH11o and EH11e modes) and two VMs of different orders (HE11o mode and EH11e mode) multiplexing transmissions over 5 km FMF are respectively constructed. To increase the transmission capacity and reduce the system cost, KK receiver is employed and the single-wavelength two sets of eigenmodes multiplexed 360 Gbit/s and 400 Gbit/s signal transmission links are achieved, respectively. Furthermore, WDM-MDM transmission is implemented over the same FMF. A total data rate of 1.12 Tbit/s MIMO-free link with 28 GBaud 16-QAM signal over all 10 channels (five wavelengths and two VMs) is realized. Then, by employing the fiber eigenmodes, two architectures of full-duplex full-polarization MDM bi-directional transmission are proposed, demonstrated and evaluated. For homo-VMs link, both uplink and downlink transmit four identical VMs and the full-duplex crosstalk is less than -13.8 dB. Accordingly, a 224 Gbit/s QPSK bi-directional transmission over 3 km FMF is implemented, using a 2×2 MIMO for each MG. In order to enhance the tolerance against back crosstalk, hetero-mode-based bi-directional link is proposed. Two VM MGs are respectively loaded in the uplink and downlink with isolation between counter directions larger than 19 dB, achieving a 448 Gbit/s 16-QAM bi-directional link over 3 km FMF. Moreover, based on the same hetero-modal scheme, a 1.792 Tbit/s WDM-MDM full-duplex bi-directional link is further demonstrated.

4

Dynamic performance evaluation of eigenmode-based MDM FMF transmission systems

This chapter extends the study to investigate the robustness and practicality of eigenmode-based MDM short-reach links. Dynamic performance evaluation is carried out on the proposed MIMO-free MGDM and MIMO-based MDM fiber transmission systems.

4.1 MIMO-free Direct-detection MGDM fiber system

4.1.1 Principle and Schematic diagram of Mode-group Filter Scheme.

As one paradigm of SDM techniques, MDM based on FMFs or MMFs has drawn lots of attention. Potentially, MDM scheme can significantly increase the capacity of optical transmission systems by multiplying the capacity of a single-mode fiber by the number of co-transmitted modes. However, the increase of mode channel counts is limited by modal crosstalk caused by mode-coupling in fiber transmission[45]. To address this concern, coherent detection in conjunction with MIMO DSP is frequently resorted to reducing the impact of crosstalk. However, this has resulted in high power consumption and huge computational complexity[26,47]. For practical short-reach transmission systems, low system cost, high energy efficiency, and simple hardware implementation are critical considerations. Thus, MIMO-free IM/DD solution is highly preferred over coherent schemes.

Until now, two main types of MIMO-free IM/DD mode-multiplexed fiber links have been reported, including MDM and MGDM transmission[85,86]. For IM/DD MDM scenarios, each fiber mode is transmitted and received as an independent channel to carry the optical signal. Weakly-coupled FMF or specially-designed fiber such as air core fiber (ACF) and ring core fiber (RCF) based on different types of modal basis sets (LP mode, OAM, VM, *etc.*) have been proposed to suppress the mode coupling[85,87–89]. However, in the circular-symmetric fiber, polarization degeneracy still exists, which will lead to mutual coupling and random rotation among degenerated modes traveling in the fiber. As a result, large power fluctuation occurs at the receiver and the performance is unavoidably affected. For IM/DD MGDM scenarios, modes sharing near-degenerate effective refractive index (n_{eff}) in the fiber are treated as one MG or one super-channel and all modes belonging to the same MG should be received simultaneously. Compared to the MDM scheme, MGDM scheme is more suitable and promising for MIMO-free transmission from a practical perspective since degenerate modes of certain MG performed as one super-channel help to eliminate the need for intra-MG crosstalk suppression. Specifically, a certain modal basis set along with a certain type of weakly-coupled FMF is a typical approach to ease the random inter-MG coupling for MGDM systems, such as the reported demonstrations of OAM-based MGDM over RCF and LP mode based MGDM over OM2 fiber. In general, the illustration of MG propagating in optical fiber can be shown in Fig.4.1. For an certain MG_n in the MGDM transmission, $m_{n,1}$, $m_{n,2}$, ..., m_{n,K_n} are the degenerate modes (polarization is excluded) and $m_{n,k}$ is an arbitrary mode within MG_n. K_n represents the number of intra-MG modes belonging to MG_n.

Mode group	Spatial modes
$\mathbf{MG_1}$	$\mathbf{m_{1,1},\ldots\ldots\ m_{1,K_1}}$
$\mathbf{MG_2}$	$\mathbf{m_{2,1},\ldots\ldots m_{1,K_2}}$
⋮	⋮
$\mathbf{MG_n}$	$\mathbf{m_{n,1},\ldots\ldots m_{1,K_n}}$

Figure 4.1: Illustration of mode groups within the transmission fiber.

For IM/DD MGDM link, MG demultiplexer (DeMUX)-based scheme and mode-diversity scheme are two representative reception methods[90,91], which are respectively illustrated in Fig.4.2 and Fig.4.3. For the former, independent optical signal is respectively loaded on an arbitrary mode ($m_{1,k}$, $m_{2,k}$, ..., $m_{n,K}$) of each MG. After mode multiplexing and fiber transmission, intra-MG modes belonging to each MG are demultiplexed by MG DeMUX and are then detected by a multimode PD, which is the most direct and convenient approach. However, MG DeMUX depends on special design and is generally compatible with certain types of fiber or mode basis. In addition, relatively high inter-MG crosstalk introduced by MG DeMUX will also degrade the performance of the system. Mode-diversity-based MGDM transmission is a single-input multiple-output (SIMO) architecture enabled by corresponding DSP for signal detection. At the transmitter, the independent optical signal is respectively loaded on an arbitrary mode

($m_{1,k}$, $m_{2,k}$, ..., $m_{n,K}$) of each MG. After mode multiplexing and fiber transmission, each intra-MG mode (polarization is excluded) is converted to the fundamental mode and is then detected by a SMF-PD at the receiver. Since more than one receiving channel is required to handle each degenerate mode within one MG, different channel responses need to be compensated by the corresponding DSP, such as maximal ratio combining (MRC) and SIMO algorithms[91,92]. Accordingly, the cost and complexity of the whole system are inevitably increased.

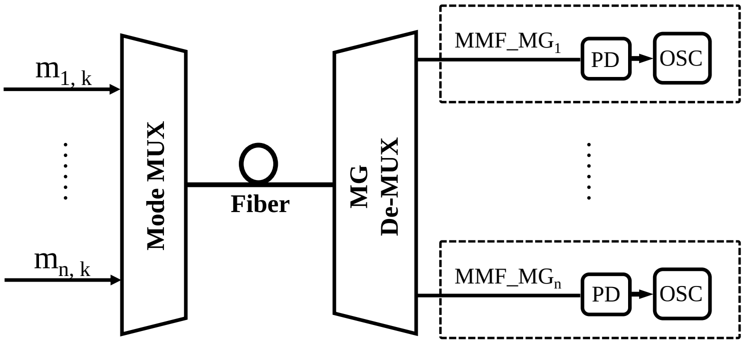

Figure 4.2: Schematic diagram of MG DeMUX-based scheme for IM/DD MGDM transmission.

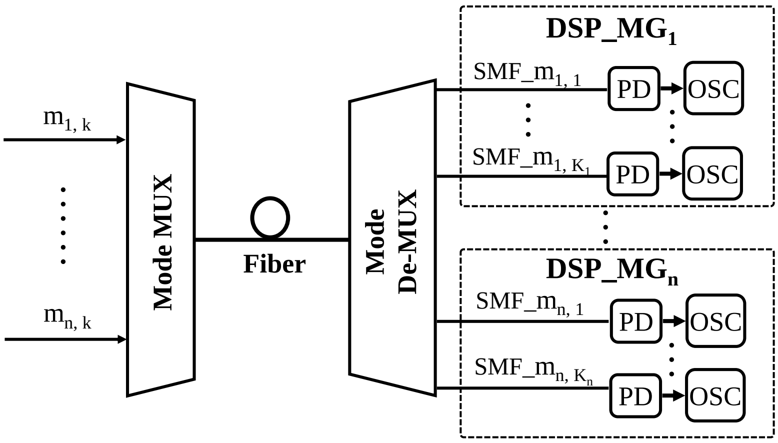

Figure 4.3: Schematic diagram of mode-diversity scheme for IM/DD MGDM transmission.

Different from previous MGDM schemes employing special MG DeMUX or mode-diversity technique, a novel and versatile MG filter architecture for IM/DD MGDM transmission is proposed, which is displayed in Fig.4.4. First, the independent optical signal is respectively loaded on an arbitrary mode ($m_{1,k}$, $m_{2,k}$, ..., $m_{n,K}$) of each MG. After mode multiplexing and fiber transmission, all the intra-MG modes of the same MG should be simultaneously received to mitigate signal power fluctuation induced from random mode crosstalk/rotation within one MG. At the receiver, in order to separate MG$_n$ from other MGs, each degenerate mode of MG$_n$ ($m_{n,1}$, $m_{n,2}$, ..., m_{n,K_n}) is demultiplexed to the fundamental mode by the corresponding mode DeMUX and then is respectively fed into SMF, filtering other MG channels. To realize single output for one MG super-channel without signal interference and loss, these parallel channels of fundamental modes are subsequently converted to K_n arbitrary orthogonal modes m_{i_1,j_1}, m_{i_2,j_2}, ..., $m_{i_{K_n},j_{K_n}}$ by the corresponding mode converters, respectively. Note that the orthogonality condition is utilized to avoid co-channel interference. Finally, these orthogonal modes are multiplexed into one output and coupled into a MMF-PD for signal detection. Accordingly, the filter for MG of MG$_n$ is realized and this approach will be further clarified with the following experimental demonstration.

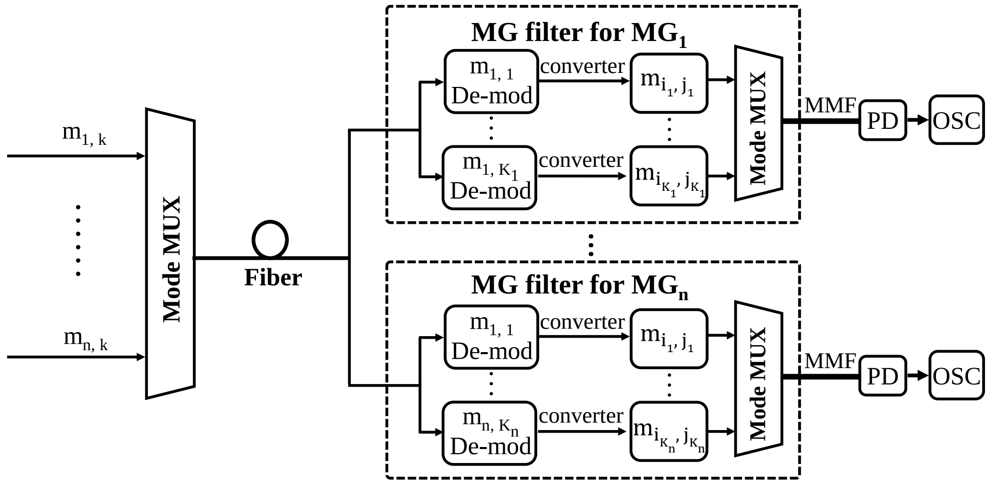

Figure 4.4: Schematic diagram of the proposed MG filter scheme for IM/DD MGDM transmission.

4.1.2 Experimental setup of MIMO-free dual-channel simultaneous transmit and receive MGDM system enabled by MG filter approach

Figure 4.5 illustrates the experimental setup of 152 Gbit/s MIMO-free two-OAM-MG MGDM transmission enabled by the MG filter scheme. At the transmitter, 38-GBaud PAM-4 pulse-shaped by 0.01 roll-off factor raised-cosine filter is generated by an arbitrary waveform generator (AWG, *Keysight*, M8196A) with 92-GSa/s sampling rate and then is boosted by the electrical amplifier (EA, *SHF*, S807). Next, it is employed to modulate the optical carrier in the intensity by a Mach-Zehnder modulator (MZM, *Fujitsu*, FTM7938EZ). The carrier at the wavelength of 1550.12 nm is from an ECL. After being amplified by an EDFA, the optical PAM-4 signal is divided into two branches by an OC. One is delayed by a long SMF jumper for signal decorrelation and is directly employed as fundamental mode channel ($l = 0$) after being collimated by a COL. Another branch is converted to OAM mode channel of $l = +3$ by a vortex phase plate (VPP, *RPC Photonics*, VPP-m1550). These two channels are multiplexed together by a NPBS and then coupled into 5 km step-index FMF (*YOFC*, FM2012-B). To calculate the crosstalk between two used MG channels in this link, we simultaneously measure the received power before PD-1 and PD-2 when only OAM of $l = 0$/OAM of $l = +3$ is transmitted. The absolute value of their difference indicates the channel isolation. For this system, the MG isolation is higher than 21.1dB, which is shown in inset (I) in Fig.4.5. Insets (II) and (III) in Fig.4.5 display the intensity profiles of two OAM channels captured by a CCD camera after FMF transmission, respectively. In order to detect two MGs simultaneously, the output light beams from FMF are divided into two parts by a 20:80 NPBS.

- At the receiver 1 (Rx-1), 20% part is directly coupled into the SMF-pigtailed photodetector integrated with a trans-impedance amplifier (TIA) (PD-1, *Finisar*, XPRV2022A) with 3-dB bandwidth of $\sim$ 32 GHz for optical-to-electrical (O/E) conversion, and the detected analog signal is denoted as $I_1(t)$. Since higher-order MGs ($l > 0$) will be filtered by SMF, only MG of $|l| = 0$ can be received;
- At the receiver 2 (Rx-2), MG filter for OAM-MG $|l| = 3$ is implemented first. 80% output beams from FMF are separated into two branches by a NPBS. In each branch, intra-MG OAM mode $l = +3/-3$ is re-converted to the fundamental mode by the corresponding VPP and then is respectively fed into SMF to filter other higher-order modes. After collimation, to satisfy the mutual orthogonality of such two branches, the upper branch is converted to $l = -3$ and the lower branch is still employed as fundamental mode. Here, these two branches could be theoretically converted to any

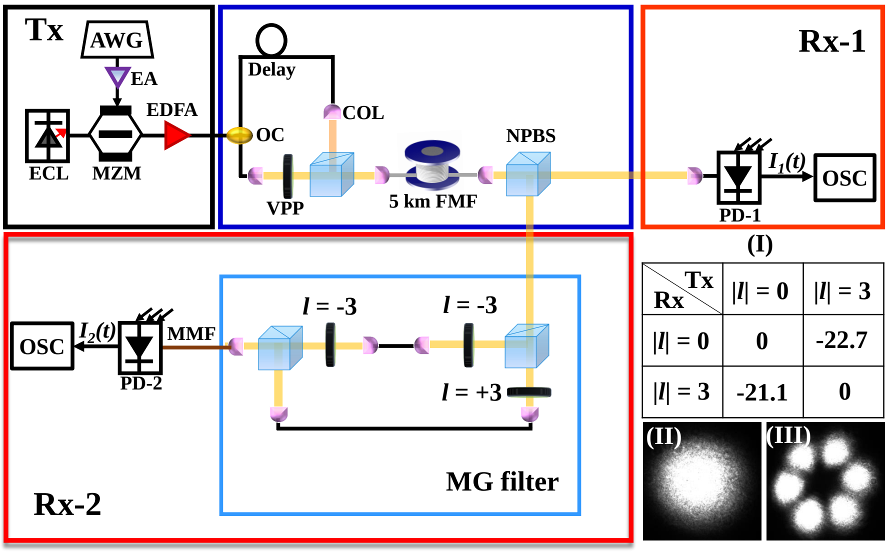

Figure 4.5: Setup of 152 Gbit/s MIMO-free OAM-based dual-channel simultaneous transmit and receive MGDM system enabled by MG filter approach. ECL: external cavity lase; MZM: Mach-Zehnder modulator; AWG: arbitrary waveform generator; EA: electrical amplifier; EDFA: erbium-doped fiber amplifier; OC: optical couple; VPP: vortex phase plate; COL: collimator; FMF: few-mode fiber; NPBS: non-polarizing beam splitter; PD: photodetector; MMF: multimode fiber; OSC: oscilloscope. Inset (I): Measured inter-MG crosstalk matrix (dB) of this transmission system. Insets (II) and (III) show the intensity profiles of $|l| = 0$ and $|l| = 3$ after 5 km FMF transmission, respectively.

two orthogonal modes (polarization is excluded). Specifically, these two paths are precisely aligned by a z-axis rail below the COL of the lower branch before multiplexing, avoiding multi-path interference from another path. Next, two branches are multiplexed into one output by a NPBS. Accordingly, a single-input and single-output (SISO) MG filter is realized. Then, the output light is injected into the MMF-pigtailed PD with TIA (PD-2, *Newport*, 1544-B) with 3-dB bandwidth of $\sim$ 12 GHz for O/E conversion, and the detected analog signal is denoted as $I_2(t)$;

- Finally, the electrical signals $I_1(t)$ and $I_2(t)$ respectively detected by the PD-1 and the PD-2 are sampled simultaneously by the two-channel oscilloscope (OSC, *Keysight* DSAZ634A) operating at a 160-GSa/s sampling rate and further processed by the off-line DSP, including synchronization, equalization by the simple T/2-spaced feed-forward equalizer (FFE), and BER decision.

4.1.3 Dynamic performance evaluation and results

Compared to SMF-based optical system, FMF/MMF-supported backbone is more vulnerable to environmental disturbance because external perturbations such as wind, temperature, and mechanical stress/bending will cause random mode mixing within and between MGs[31,90]. Thus, for a practical IM/DD MGDM system, apart from total capacity and cost per bit, robust and reliable performance is equally important.

To further evaluate the transmission performance, both static and dynamic performance evaluation are implemented on this two-MG MGDM system. First, its static BER properties over 5 km FMF transmission versus ROP are measured. Here, the ROP of each channel is adjusted by the EDFA with an output power control function at the transmitter and the signal sets of two channels are simultaneously stored by the identical OSC. Fig.4.6 and Fig.4.7 respectively present the averaged BER performance for MGs $|l| = 0$ and $|l| = 3$ using FFE with different number of taps. Obviously, FFE with more taps is more beneficial to the system performance at the price of higher computational complexity. BER saturation is almost achieved for both MGs when 40-tap FFE is implemented, which is also adopted in the following experiments. In addition, it can be seen that the required ROPs for $|l| = 0$ and $|l| = 3$ are approximately -7.7 dBm and -7.3 dBm at 7% HD-FEC of BER at 3.8×10^{-3}, with power penalty < 0.5 dB for $|l| = 3$.

Furthermore, 8 static cases are considered for BER evaluation, and the experimental results are shown in Fig.4.8, where $|l| = 0/3$ and $l = -3/+3$ respectively represent the full-MG reception using the proposed filter approach and partial-MG reception(single intra-group mode, mode $l = -3$ or mode $l = +3$) when blocking the path of $l = +3$ or mode $l = -3$. (S.) and (M.) represent the single-MG ($|l| = 0/3$) transmission and dual-MG transmission ($|l| = 0$ and $|l| = 3$), respectively. Here, the ROP of $|l| = 3$ (the total power of $l = -3$ and $l = +3$) is also used to represent the ROP of $l = -3/+3$ for simplicity. For single-MG transmission, the BER of MG $|l| = 3$ is worse than that of MG $|l| = 0$ mainly due to the narrower bandwidth of PD-2. For two-MG multiplexing transmission, BERs of approximately 5×10^{-5} and 2×10^{-4} for MG $|l| = 0$ and $|l| = 3$

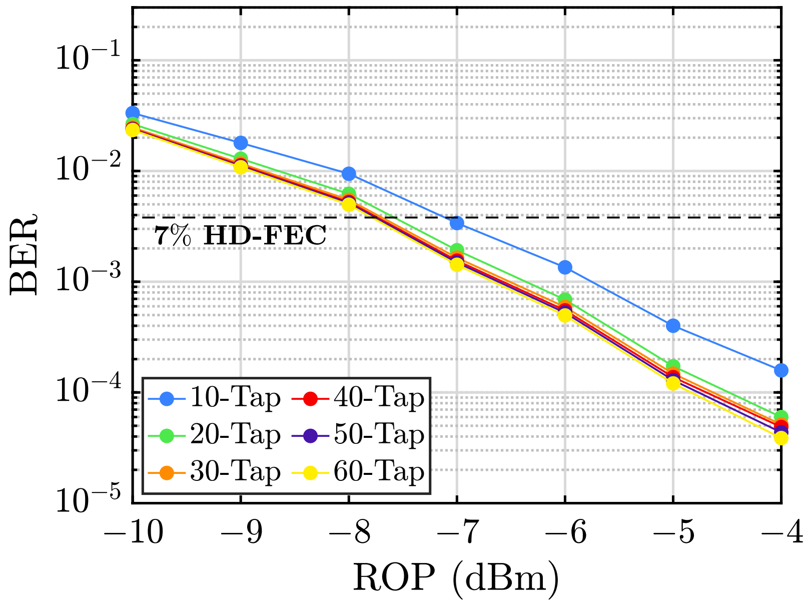

Figure 4.6: Measured BER versus ROP using FFE with different numbers of taps for (a) $|l| = 0$ over 5 km FMF.

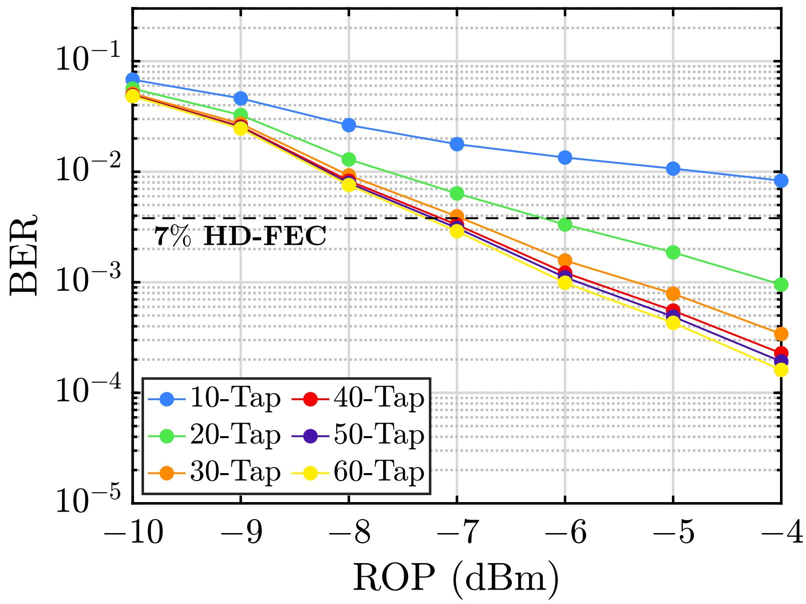

Figure 4.7: Measured BER versus ROP using FFE with different numbers of taps for (a) $|l| = 3$ over 5 km FMF.

can be realized, respectively. The BERs of MG $|l| = 0$ and MG $|l| = 3$ are still different because of the differences in power responses of two used PDs and inter-MG crosstalk. In addition, it is clearly observed that partial-MG reception ($l = -3$ or $l = +3$) has worse BER performance compared to full-MG reception ($|l| = 3$) with/without inter-MG crosstalk since it lost the power of undetected modes within the MG. Theoretically, due to random mode coupling/rotation within MG during the fiber propagation, ROP and BER of partial-MG reception vary with time. Meanwhile, full-MG reception is not affected and its performance is always superior to partial-MG reception since mode power loss within MG can be avoided.

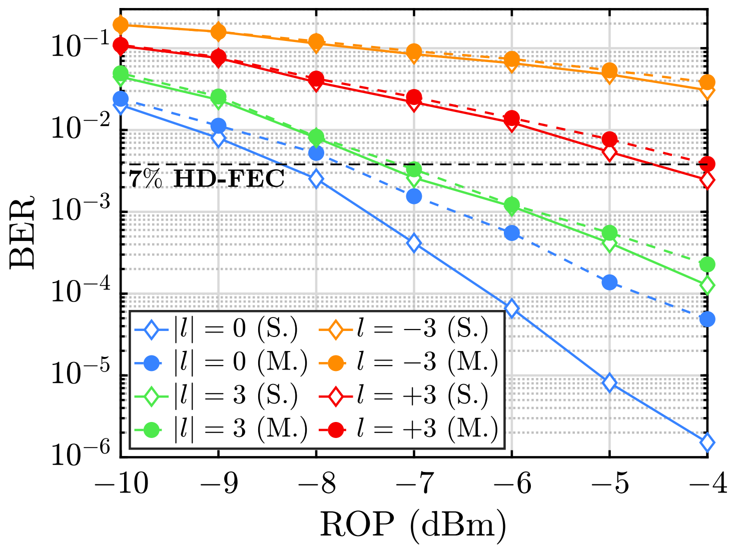

Figure 4.8: Measured BER versus ROP over 5 km FMF.

Besides, the variation of the calculated SNR versus ROP is depicted in Fig.4.9. It can be seen that even during a short time of static testing, the inter-MG crosstalk not only degrades the SNR/BER performance but also enlarges the system variation in SNR/BER performance, especially for MG $|l| = 0$ with better SNR performance in this system.

For a practical IM/DD MGDM link, stable polarization-/mode-independent performance is highly desirable. To ensure the reliability of our system, dynamic performance evaluation of BER under four scenarios over five timeslots (3.5 hours in total) is also implemented at the ROP of −4 dBm as shown in Fig.4.10.

- First scenario from 23:00 to 23:30 Hong Kong time (HKT): only MG $|l| = 0$ is trans-

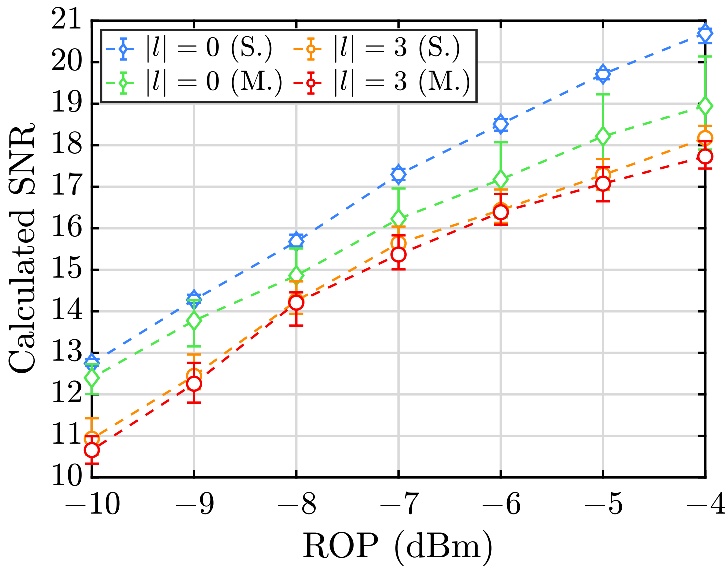

Figure 4.9: Calculated SNR variation versus ROP over 5 km FMF.

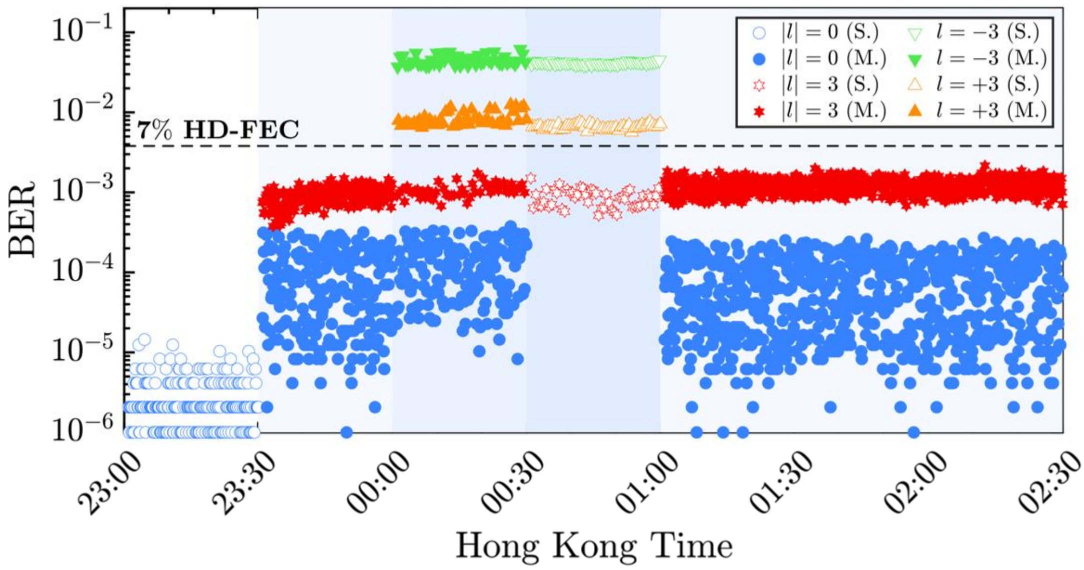

Figure 4.10: Dynamic evaluation of BER performance versus time (HKT) under four scenarios at the ROP of −4 dBm.

mitted and received. BER performance of MG $|l| = 0$ are quite low and stable during this timeslot without inter-MG crosstalk;

- Second scenario from 23:30 to 00:00 HKT, MG $|l| = 3$ is then co-transmitted with MG $|l| = 0$ and these two MGs are simultaneously received. It is clearly observed that the BERs for both MGs are always lower than 3.8×10^{-3}, although BER performance of $|l| = 0$ has degraded to a certain extent compared with its value in the first scenario. In addition, the fluctuation of BER for $|l| = 0$ is increased from the first scenario to this scenario with inter-MG crosstalk and is also larger compared with its value for MG $|l| = 3$, probably because the BER for MG $|l| = 0$ is better and the effect of crosstalk is more obvious.
- Third scenario from 00:00 to 00:30 HKT, same as in the second scenario, two MGs are simultaneously transmitted. But at the receiver side, MGs of $|l| = 0$ and $|l| = 3$ (full-MG reception), or MG $|l| = 0$ and mode $l = +3/-3$ (partial-MG reception) are simultaneously received. As it can be seen that BER performance of partial-MG reception is much worse than full-MG reception, since the partial one loses certain power over undetected modes within the MG;
- Fourth scenario from 00:30 to 01:00 HKT, MG $|l| = 0$ is switched off and then only MG $|l| = 3$ is transmitted. At the receiver, MG $|l| = 3$, mode $l = +3$, and mode $l = -3$ are sequentially and repeatedly received over time. Obviously, without crosstalk from MG $|l| = 0$, BERs of MG $|l| = 3$, mode $l = -3$, and mode $l = +3$ are improved on average and have smaller fluctuation over time;
- Back to the second scenario from 01:00 to 02:30 HKT, BERs of both two MGs still reach the previous plateau below 3.8×10^{-3} and are close to them in the timeslot from 23:30 to 00:00 HKT.

During the dynamic performance evaluation, some phenomena are similar to those in static cases. All these static and dynamic evaluations have demonstrated the practicality and reliability of such MGDM system. On the other hand, it can be deduced that compared to single-MG transmission, inter-MG crosstalk in MGDM system will cause larger fluctuation in BER/SNR performance to a certain extent and may have various impacts on different transmitted MGs. Thus, dynamic performance evaluation and margin assessment for practical IM/DD MGDM systems are necessary and significant and deserve further study and discussion in the future.

4.2 MIMO-based four VMs multiplexing system

4.2.1 Experimental setup of Four Vector Eigenmode Multiplexing transmission based on Kramers–Kronig Receiver

As for SDM/MDM fiber-optic transmission with MIMO DSP, mode coupling and mode-dependent loss or gain (MDL or MDG) induced by external perturbation are inherently random variables, which will undoubtedly increase the chance of singularity attack for MIMO systems[93–95]. As a result, the accuracy and reliability of system evaluation are challenged. Thus, this subchapter focuses on the singularity phenomena, the impact of MDL, and mode coupling/rotating in the MIMO-MDM system.

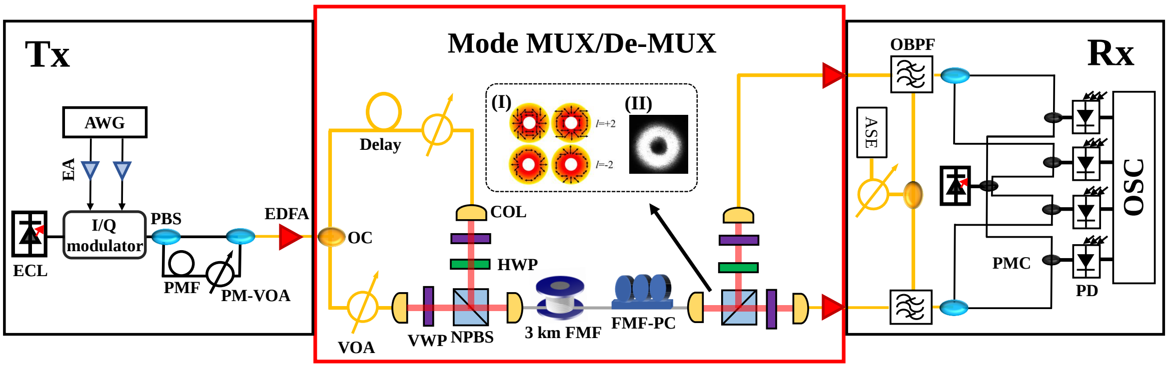

Figure 4.11: Framework of illustrated 448 Gbit/s 16-QAM VM-based MDM transmission with KK reception and 4×4 non-Singular MIMO over 3 km FMF. ECL: external cavity laser; AWG: arbitrary waveform generator; EA: electrical amplifier; I/Q Mod.: in-phase/Quadrature modulator; PBS: polarization beam splitter; PMF: polarization maintaining fiber; PM-VOA: polarization maintaining variable optical attenuator; EDFA: erbium-doped fiber amplifier; OC: optical coupler; VOA: variable optical attenuator; Col: collimator; VWP: vortex wave plate; HWP: half-wave plate; NPBS: non-polarizing beam splitter; FMF: few mode fiber; FMF-PC: few-mode fiber-based polarization controller; OBPF: optical bandpass filter; ASE: amplified spontaneous emission source; PMC: polarization maintaining coupler; PD: photodetector; OSC: oscilloscope. Insert (I) displays the theoretical SoP distribution of used four fiber eigenmodes of $|l| = 2$. Insert (II) displays the intensity profiles of the multiplexed eigenmodes after 3 km FMF transmission.

Figure 4.11 presents the framework of 448 Gbit/s VM-based MDM transmission over 3 km FMF. At the transmitter, the 28-GBaud 16-QAM signal spectrally-shaped with a 0.1 roll-off factor (RF) raised-cosine (RC) filter is generated by an arbitrary waveform generator (AWG, *Keysight* M8194A) operating at a 112-GSa/s sample rate and then is amplified by the electrical amplifier (EA, *SHF*, S807). Subsequently, it is utilized to modulate the optical lightwave from the external cavity laser (1550.12 nm, 100 kHz linewidth) through in-phase/quadrature modulator (I/Q modulator, *Fujitsu* FTM7962EP). Next, PDM is emulated by two PBSs. In order to fully de-correlate signals of such two orthogonal channels, a 1-m polarization-maintaining fiber (PMF) jumper and a polarization-maintaining variable optical attenuator (PM-VOA) with the function of altering polarization-dependent loss (PDL) are inserted into one path. After amplified by an EDFA, such daul-polarization signal is divided into two branches by an OC. Here, the signal of one branch is de-correlated by a 10-m SMF jumper. for de-correlation. Then, each branch is followed by a variable optical attenuator (VOA) to adjust MDL in the experiment.

In the part of mode MUX/De-MUX, one branch is converted to vector modes of $l = +2$ ($EH_{11,even}$ and $EH_{11,odd}$ modes) after passing through a vortex wave plate (VWP, *Thorlabs*, WPV10-1550). Meanwhile, another branch is transformed to vector modes of $l = -2$ ($HE_{31,even}$ and $HE_{31,odd}$ modes) by a VWP and a HWP. Accordingly, four vector modes of $|l| = 2$ are generated (including polarization), whose theoretical SoP distribution are respectively displayed in insert (I) in Fig.**4.11**. Then, such four vector modes are multiplexed together by a NPBS and then fed into the 3 km step-index FMF which has been introduced in Chapter 2.3.1 in detail. Here, a self-fabricated FMF-PC is employed to adjust the SoP and mode coupling of the beam of output. Insert (II) in Fig.**4.11** shows the intensity pattern of multiplexed eigenmodes of $|l| = 2$ after 3 km FMF transmission. Next, the output is divided into two parts by another NPBS. Two vector modes of $l = +2$ of one part are reconverted to orthogonal fundamental modes by a VWP. while two vector modes of $l = -2$ of another part are also reconverted by HWP cascaded with VWP. Afterwards, each part is coupled into the SMF to directly detect the fundamental modes with two orthogonal SoPs.

At the KK receiver, the signal of each part is first amplified by a EDFA and then is coupled with an amplified spontaneous emission source (ASE) in tandem with a VOA to attenuate OSNR. After being filtered by an optical bandpass filter (OBPF), the orthogonal SoPs of each part are split by a PBS and coupled with the LO source. Such LO is offered by another ECL, which is divided into four parts equally by a polarization maintaining coupler (PMC). Here, compared to the optical carrier at the transmitter, these four LOs all have a frequency offset (FO) of 28-GHz$\times(1+0.1)/2$. In addition, the carrier-to-signal power ratio (CSPR) is arranged at 12 dB for KK reception. Next, these four parts are respectively sent to four PDs and are simultaneously sampled by the four-channel oscilloscope (OSC, *Keysight*, DSAZ634A). Specifically, these four optical parts from the final NPBS to four PDs are carefully aligned to reduce path delay. Finally, the recorded signals are further processed by the offline DSP. where the 4×4 multi-user constant modulus algorithm (MU-CMA) is applied in the pre-convergence stage to avoid singularity issues and lower complexity and then the estimated non-singular channel matrix by MU-CMA is utilized to initialize all taps of 4×4 RDE for adaptive demultiplexing and equalizing such MIMO-based MDM system[31,96].

4.2.2 Experimental results and discussion

During the FMF transmission, mode coupling among multiple MGs and mode rotation within each MG and MDL (Hereafter, MDL is employed to refer to MDL,MDG and PDL.) variations among all guided mode channels will occur when external disturbance or manufacturing imperfection change locally, leading to power exchange among MDM channels. In order to investigate the resilience and survivability of such MDM system, both static and dynamic performance evaluation are implemented. For simplicity, mode 1, mode 2, mode 3, and mode 4 are respectively employed to represent these four vector modes.

Firstly, the averaged BER property of all four channels versus OSNR with different taps of 4×4 MU-CMA and RDE are measured, which is illustrated in Fig.4.12 (a). As can be seen, the BER performance can meet HD-FEC of 3.8×10^{-3} under certain OSNR. Apparently, the BER reaches a saturation level of approximately 1.3×10^{-3} under 36-dB OSNR when the number of taps is 19. Fig.4.12 (b) illustrates the BER

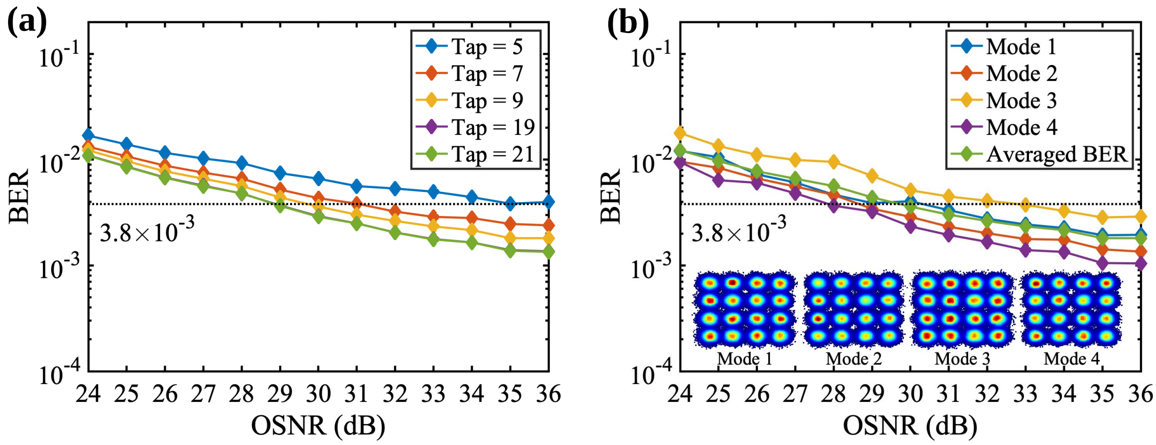

Figure 4.12: (a): Averaged BER performance of four eigenmodes versus OSNR with different numbers of taps. (b): Averaged BER performance of four eigenmodes versus OSNR with 9-tap case. The exhibited constellation of each mode is under 36-dB OSNR with 9-tap.

performance of each channel versus OSNR with 9 taps which is the minimum number of taps for HD-FEC of BER at 3.8×10^{-3} for each channel. The constellations of each channel under 36-dB OSNR are also inserted in Fig.**4.12** (b). Note that there is a slight difference in performance among these four channels, which may result from MDL.

Next, to imitate and further evaluate the impact of MDL, four scenarios under static case with different MDL conditions including no extra MDL, 3-dB MDL by attenuating 3-dB power of $l = -2$, of $l = +2$, and of X-polarization are carried out, which is enabled by two VOAs and one PM-VOA with the function of adjusting the launched power of corresponding modes. The calculated SNR of each mode channel versus OSNR is plotted in Fig.**4.13** (a-d), respectively. Here, in order to optimize the compensation of linear distortions in this MDM system, 19-tap MU-CMA in tandem with 19-tap RDE is utilized.

Under the OSNR as high as 36 dB, the largest gap of the calculated SNR among these four mode channels is viewed as MDL. For example, when no extra MDL is involved, the averaged SNR of four modes can respectively reach 16.3 dB, 16.7 dB, 16.0 dB and 17 dB. Thus, the MDL for this scenario is approximately 1 dB, which may be induced by discrete components and non-coaxial alignment in the experiment. As for the other three scenarios, extra 3-dB MDL leads to both SNR improvements over modes without power attenuation and SNR degradations over modes with power attenuation. The averaged SNRs under all four scenarios are listed in Table **4.1**.

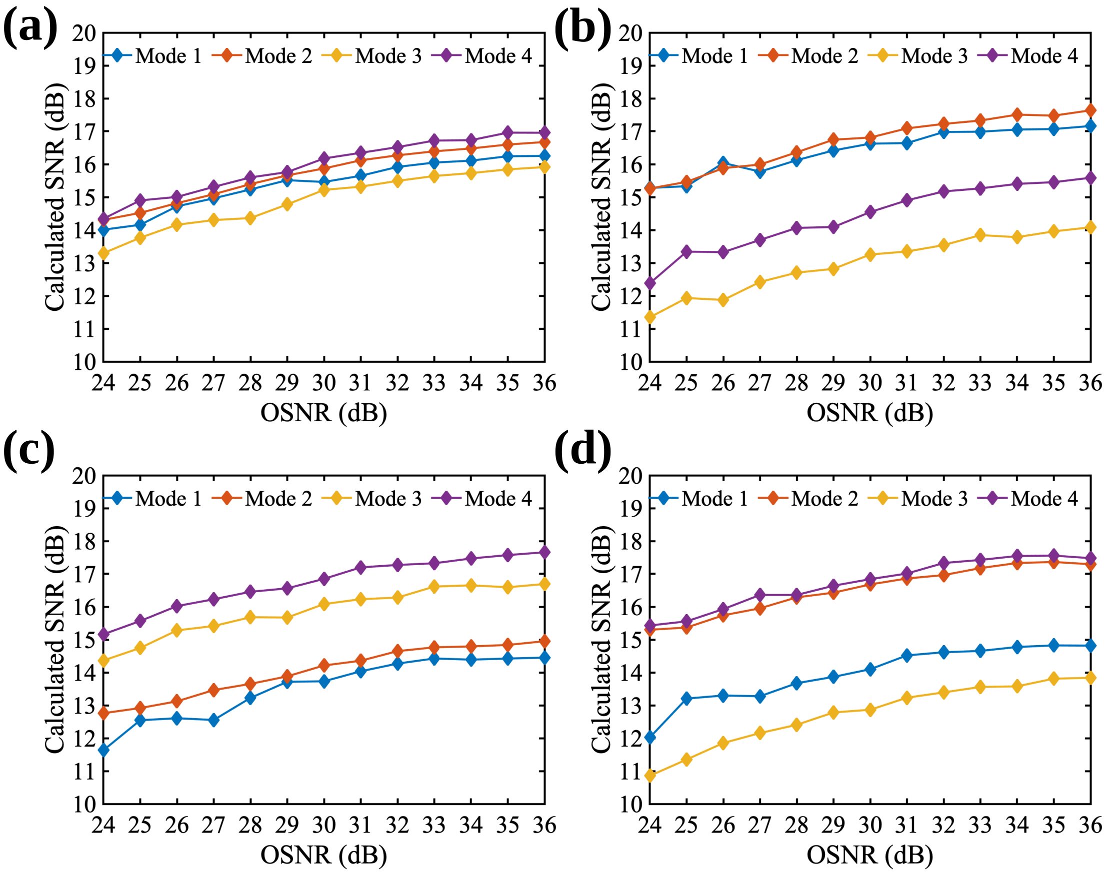

Figure 4.13: Calculated SNRs of four eigenmodes with 19 tap under: (a) no extra MDL; (b) 3-dB MDL over $l = -2$; (c) 3-dB MDL over $l = +2$; (d) 3-dB MDL over X polarization.

Table 4.1: Calculated SNRs of four eigenmodes with 19-tap and 36-dB OSNR under different scenarios.

Scenarios	Mode 1	Mode 2	Mode 3	Mode 4
without extra MDL	16.3 dB	16.7 dB	16.0 dB	17.0 dB
$l = -2$ with 3-dB MDL	17.2 dB	17.6 dB	14.1 dB	15.6 dB
$l = +2$ with 3-dB MDL	14.5 dB	15.0 dB	16.7 dB	17.7 dB
X Pol. with 3-dB MDL	14.8 dB	17.3 dB	13.8 dB	17.5 dB

To assess the survivability and reliability of this system, dynamic performance evaluation of BER and calculated SNR is also implemented at the OSNR of 36 dB, which includes two stages. In the first stage, the test is performed under the general lab environment without extra perturbation, which lasts 12 hours. In the second stage, a self-fabricated FMF-PC is employed during the FMF transmission to randomly change mode coupling and MDL over 1 hour. Such FMF-PC is modeled by reference to commercial SMF-based PC, which is shown in Fig.**4.14**. To fully compensate linear impairments during the dynamic testing, 19-tap MU-CMA along with 19-tap RDE is adopted in the MIMO DSP. The experimental results of BER performance and calculated SNR versus HKT are respectively plotted in Fig.**4.15** and Fig.**4.16**.

First stage: from 2:00 AM to 2:00 PM HKT (12 hours in total). It is to be observed that from 2:00 AM to 8:00 AM, the BER values of each mode channel are relatively stable, which always meet HD-FEC of 3.8×10^{-3}. Meanwhile, the calculated SNR of all channels is also stable during that time. It can be reasonably speculated that there is nobody in the lab and the experimental environment is stable to a certain extent. However, during the interval between 8:00 AM and 9:00 AM HKT, both BER and SNR performance of four mode channels encounter larger fluctuation and degrade slightly. It may be ascribed to the disturbance by the staff members who walk into the lab successively to start work during this time slot. After 9:00 AM HKT, BER and SNR values of all channels reach a new plateau with performance degradation until 2:00 PM HKT. Even though the system performance experiences deterioration and fluctuation in the whole process, none of the singular problems is detected. In addition, the averaged BER value of all channels can be lower than 2.2×10^{-3} which still satisfies HD-FEC of 3.8×10^{-3}.

Second stage: from 2:00 PM to 3:00 PM (1 hour in total). During this time span, in order to imitate and further accelerate the change of mode mixing and MDL, the self-made FMF-PC is rotated at random. Obviously, due to direct perturbation, the fluctuation of both BER and SNR performance of all channels are greatly enlarged compared to the first stage. In spite of excessive fluctuation and distortion in system

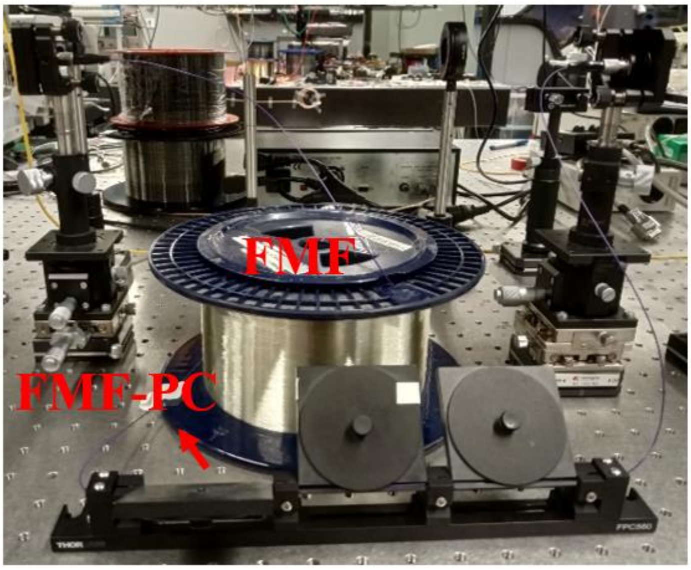

Figure 4.14: Used few mode fiber-based PC in the experiment.

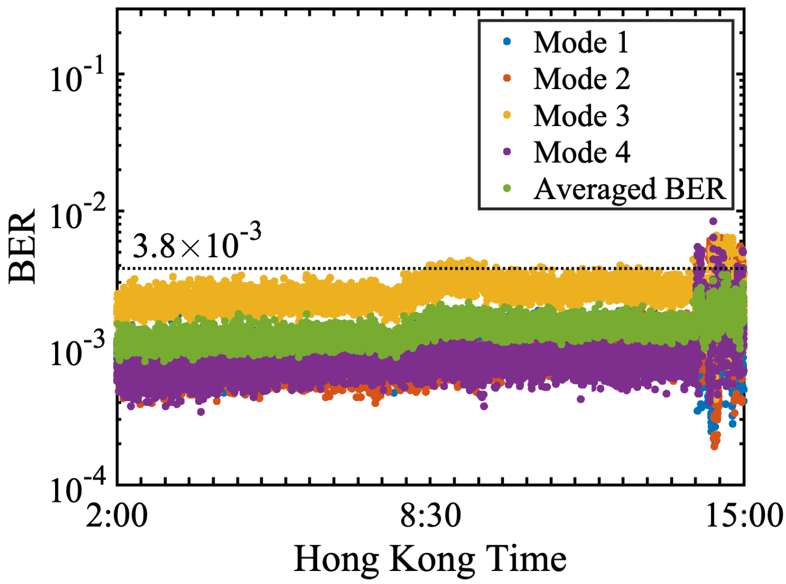

Figure 4.15: Dynamic performance evaluation of BER property versus time (HKT) with 19 taps.

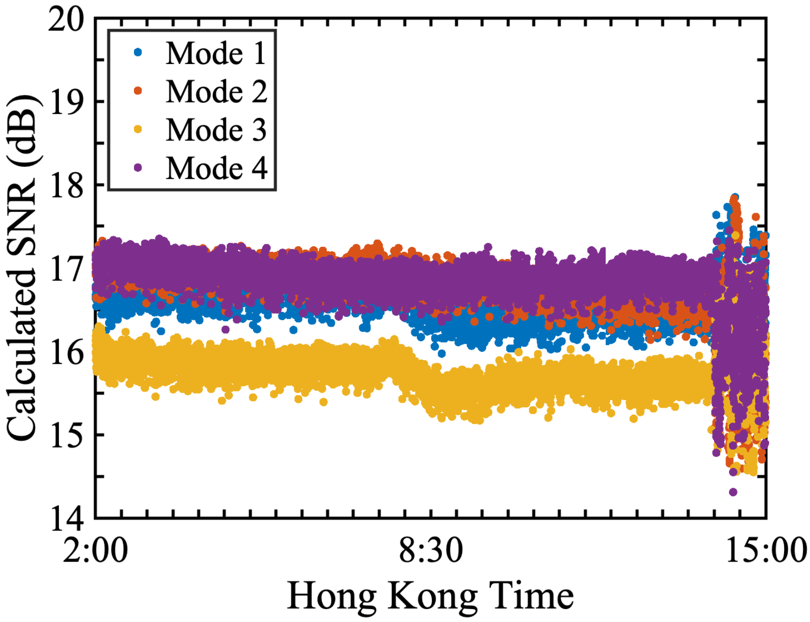

Figure 4.16: Dynamic performance evaluation of calculated SNRs versus time (HKT) with 19 taps.

performance, singularity phenomena are undetected as well. Moreover, the maximum value of averaged BER of all channels is approximately 3.4×10^{-3}, which still remains below 3.8×10^{-3}.

Figure 4.17 (a) and (b) respectively present the absolute value of weights of all test results over 16 filters in 4×4 MIMO in these two stages, which can be employed to analyze mode coupling/rotating. Specifically, the value of each normalized w_{ij} can denote the degree of channel coupling from mode j to mode i. For example, w_{23} in Fig.4.17 (a) can be regarded as almost zero for the central tap, indicating that the power coupling from mode 3 to mode 2 seems very weak during the first stage. Meanwhile, w_{24} and w_{41} seldom appear relatively large central tap compared to other weights except for w_{23}, which reveals that the frequency of mode coupling between these corresponding channels is probably low during this time slot. Theoretically, the ideal FMF-PC enables each high-order guided mode to realize four-dimensional rotation. However, it is almost impossible to be realized by the self-fabricated FMF-PC. According to Fig.4.17 (b), when FMF-PC is rotated randomly, a large central tap appears in the weight of w_{23} on several occasions, while the central taps of w_{24} and w_{41} still remain at almost the same level.

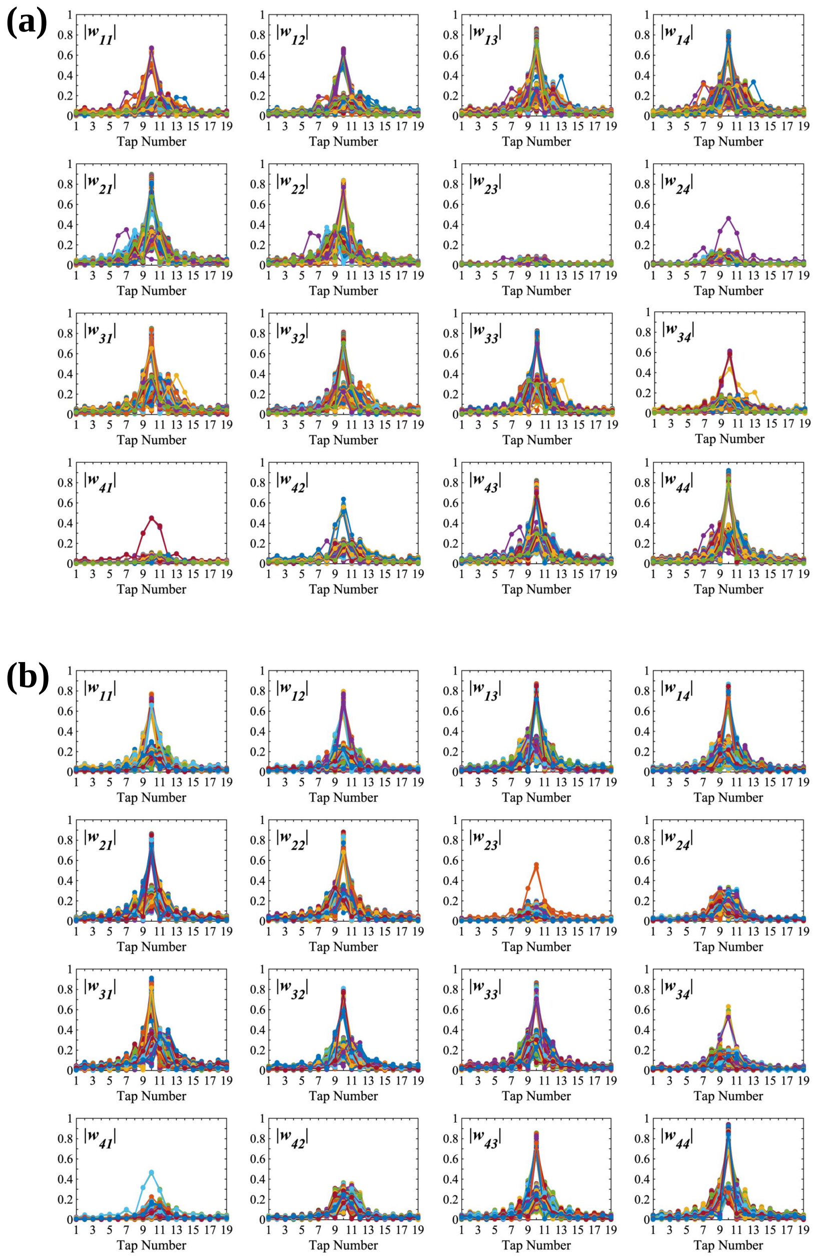

Figure 4.17: Absolute value of weights under (a) 12-hour stable duration; (b) 1-hour FMF-PC rotation duration, with 19 taps.

4.3 Summary

In this chapter, a simple and versatile MG filter architecture for MGDM IM/DD transmission is proposed, demonstrated and evaluated for the first time to the knowledge. The MG filter is realized in the optical domain and only a single PD is required to receive the signal carried by each MG. Based on this scheme, by utilizing two OAM MGs ($|l| = 0$ and $|l| = 3$) and one SMF-PD and one MMF-PD, a 152 Gbit/s PAM-4 MIMO-free simultaneous transmit and receive IM/DD system over 5 km FMF is successfully realized, in which BER of approximately 4×10^{-5} for MG of $|l| = 0$ and BER of approximately 2×10^{-4} for MG of $|l| = 3$ are obtained in the static test, both below the 7% HD-FEC BER threshold of 3.8×10^{-3}. In order to evaluate the practicality and stability of this transmission, BER performance of each MG under different conditions over a reasonably long period of time (210 minutes in total) is assessed dynamically, in which all the BER results under the proposed scheme stay below 3.8×10^{-3}. Secondly, a 448 Gbit/s 16-QAM four-vector-mode multiplexing transmission over 3 km FMF is constructed, utilizing KK reception and 4×4 non-Singular MIMO for presentation. For the static test, the BER performance of all four mode channels can be lower than 3.8×10^{-3}. For the 13-hour dynamic test, including stable duration lasting 12 hours and FMF-PC rotating duration lasting one hour, the averaged BERs of all channels can also meet FEC BER threshold of 3.8×10^{-3} with the maximum averaged BERs of 2.2×10^{-3} and 3.4×10^{-3} respectively. The experimental results sufficiently prove that the proposed VM-based MDM system is at least to some extent immune to singular issues and certain PDL/MDL. The demonstrations in this chapter pave the way toward the practical application of eigenmode-based MDM fiber-optic communication links.

5

Conclusions and Prospect

In this chapter, conclusions of this thesis are presented with a prospective outlook for potential future works of fiber eigenmode based MDM short-reach transmission.

5.1 Conclusions

Progress made in fiber-optic communication networks during the past several decades has greatly stretched transmission capacities to the physical limit of SMF. Currently, SDM technology is expected to play a highly active and vital role to break through the capacity limit. As one branch of SDM, MDM involves the simultaneous transmission of multiple orthogonal fiber modes, each carrying an independent optical signal over FMF/MMF. As the true eigenmodes of optical fiber, Vector modes actually manifest the most exact, straightforward and full basis set, which is worthwhile to explore in MDM fiber transmission. In this thesis, the frameworks of direct eigenmode based MDM transmission systems are presented. Furthermore, to enhance the system capacity and simplify the MDM transmission architecture, several novel MDM scenarios for the short-reach links are proposed and investigated in detail.

In Chapter 1, the derivation and the developmental process of SDM/MDM technology are overviewed. Among the intrinsic DoFs of optical light, spatial dimension might be the last one to exploit. As the information carriers of the MDM scheme, two typical guided modes in the fiber, including rigorous theory based vector mode and simplified approach based scalar mode are introduced in mathematical equations derived from Maxwell equations. Although efficiently harnessing the spatial DoF of the optical carrier provides fresh insights into the upgradation and revolution of fiber-optic communication networks, a variety of formidable challenges still remain. Thus, in the thesis, both novel schemes and practical execution of the fiber eigenmode based MDM transmission in realistic systems are taken into consideration.

In Chapter 2, to characterize the FSO transmission properties of vector mode, the degree of divergence and the impact of atmospheric turbulence are experimentally investigated and analyzed, respectively. Compared to the scalar Gaussian mode, the donut-shaped vector mode tends to diverge faster in FSO link. As for the influence of atmospheric turbulence, Spatially multiplexed free-space communication based on four vector modes belonging to the MG of $|l| = 2$, each carrying high speed signal of 28-Gbaud 16-QAM, are implemented and discussed under three different levels of atmospheric turbulence. Before characterizing the FMF transmission performance of vector mode, unique traits of vector modes are elaborated based on the higher-order Poincare sphere model. In addition, the corresponding relationships between vector mode associated with non-homogeneous SoPs and two types of scalar modes including LP mode and OAM mode are also built.

In Chapter 3, various fiber eigenmode-based MDM schemes for short-reach optical interconnects are proposed and experimentally demonstrated. In order to deal with the trade-off between high capacity with superior performance and simple structure with low power dissipation in short-distance link, KK reception which possesses significant advantage in terms of cost-effectiveness is employed to guarantee favorable performance in the following schemes. By using the same order vector modes of $l = +2$, EH11o and EH11e modes, 360 Gbit/s VMDM with 45 GBaud 16-QAM over 5 km FMF transmission is achieved without MIMO DSP. Then, two vector modes of different orders ($l = 0$ and $l = +2$) multiplexed 50 GBaud 16-QAM signal transmission over 5 km FMF is realized without MIMO DSP as well. Furthermore, wavelength- and vector mode-division multiplexing transmission including five wavelengths and two VMs (HE11 and EH11 modes) is implemented over the same fiber. A total data rate of 1.12 Tbit/s MIMO-free link with 28 GBaud 16-QAM signal over all 10 channels is successfully demonstrated. For bi-directional link, two bi-directional architectures of homo-VMs and hetero-VMs transmitted in two directions are implemented based on coherent detection and 2×2 MIMO DSP. Initially, both uplink and downlink transmit four identical vector modes. Due to the same-mode crosstalk caused by RB and FR of this full-duplex system, each mode channel is only able to carry 14 GBaud QPSK signal and a 224 Gbit/s bi-directional link over 3 km FMF is demonstrated. Next, the second scheme of employing different VMs on two ends to minimize the impact from back crosstalk on the same mode is proposed. Two dual-polarization VMs of $l = 0$ and two dual-polarization VMs of $l = +2$ are respectively loaded in the up and down streams. The isolation between opposite directions is larger than 19 dB and a

448 Gbit/s bi-directional VMDM transmission is demonstrated over 3 km FMF. Obviously, compared with the former demonstration, this scheme doubles the transmission capacity under the same hardware conditions. Additionally, in tandem with WDM technology, a 1.792 Tbit/s WDM-VMDM full-duplex bi-directional system with four wavelengths on the two ends is successfully achieved. The experimental results of the above demonstrations fully indicate that fiber eigenmode based MDM scenarios could find enormous potential for future high-speed short-haul interconnect systems.

Chapter 4 further extends the study to investigate the reliability of fiber eigenmode based MDM fiber-optic systems, which should be resilient to changes in the external environment of field experiments. First, a simple, flexible, and cost-effective MG filter approach for MGDM IM/DD transmission is reported, which avoids received power fluctuation by random mode rotation through FMF with time. By utilizing this MG filter scheme, a MIMO-free MGDM IM/DD multiplexing two OAM MGs with a total of 152 Gbit/s PAM-4 is experimentally demonstrated over 5 km FMF. The performance of BER and SNR is evaluated statically versus ROP and dynamically over time. The BER of two MGs can satisfy 7% HD-FEC BER threshold of 3.8×10^{-3} under both static and dynamic cases, which adequately verifies the robustness and feasibility of such MGDM scheme based on the proposed MG filter architecture. Next, a 448 Gbit/s four vector modes multiplexing transmission with 28-GBaud 16-QAM signal over 3 km FMF is experimentally demonstrated based on KK Reception and 4×4 non-Singular MIMO DSP. To justify the practicality and stability of such link, 7408 signal sets which include 598 static sets and 6,810 dynamic sets over 13-hour are tested and none of the singular problems is detected. These experimental results sufficiently verify that the fiber eigenmode based MDM transmission might be a competitive candidate for realistic high-capacity optical interconnect networks.

In the final chapter, the main works of the thesis are concluded. The research contributions in the thesis just cover a small portion of a holistic consideration of issues related to the VMDM-based fiber-optic communication systems and other practical applications, which might be beneficial to the exploration of the potential of MDM schemes. Despite some successful realizations of demonstration experiments enabled by various SDM/MDM-based scenarios in the past few years, The anticipated performance and operational simplicity of SDM/MDM-based fiber-optic networks are far from reaching the stage of practical deployment, where more research effort and cooperation are needed in the future.

5.2 Future works

The studies of fiber-based structured light fields and SDM/MDM-based fiber-optic communication systems in the course of the Ph.D. period enlarge my knowledge scope of optical fiber waveguides, fiber drawing process and fiber-optic communication systems. Based on the presented works, some potential extensions related to this research thesis are illustrated and discussed as follows.

A: An ideal property for future SDM/MDM-based short-reach optical links is the realization of signal processing and optimization in the optical domain. Thus, the SDM/MDM-related optical elements with high fidelity are necessary and crucial, such as SDM/MDM optical EDFA, fan-in fan-out device for SDM fiber, mode (de)-multiplex, mode filter, mode switch and so on[97–99]. Figure 5.1 depicts an ideal SDM/MDM communication link with ideal optical devices (SDM/MDM Fan-in/fan-out and SDM/MDM EDFA), which exhibits a high level of convenience and compactness. However, SDM/MDM-based communication networks are still being studied in laboratory environment and corresponding optical devices for optical communication links are not yet mature and commercially available, which deserves more attention and investigation. Notably, the development of SDM/MDM-related optical devices and schemes will further facilitate the practical application of SDM/MDM. In addition, some optical-domain compensation or optimization techniques for SDM/MDM systems, such as mode-coupling compensation, optical path matching and (de)-correlation, are equally significant[100,101]. After all, compared to dealing with signals in the electrical domain, optical information processing is more direct, convenient and efficient, which could alleviate latency, computational demand and power consumption to some extent.

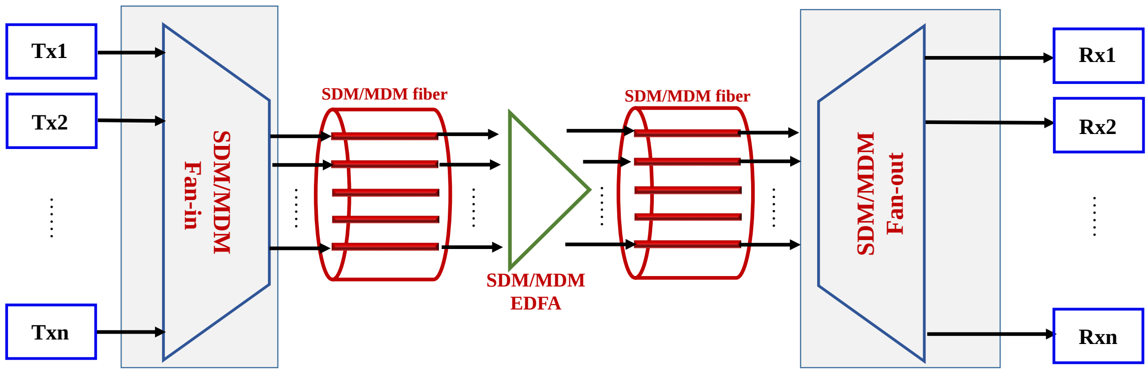

Figure 5.1: Simplified diagram of ideal SDM/MDM communication system.

B: It is noted that cost and size are two main concerns that should be weighed properly for SDM/MDM optical links, especially for short-haul networks. The reasonable utilization and allocation of multi-dimensional resources are significant considerations for operators, who are under the pressure of reduction in cost per bit as well as improvement in system performance. Wavelength-routed optical network (WRON) which is regarded as the current mainstream solution will eventually be constrained since the high-quality frequency resources are +limited. In addition, WRON is not helpful for a substantial reduction in cost. Compared to wavelength resources, the spatial dimension is theoretically able to provide infinite sub-channels and is also competitive as an economical means for large-capacity transmission. However, problems of high-density SDM/MDM including sophisticated SDM/MDM fiber drawing process, finite transmitting and receiving apertures, the crosstalk among parallel spatial channels and huge computational complexity are difficult to overcome. There is also a growing consensus that SDM/MDM fiber-optic systems ought to take advantage of spatial resources in a rational and efficient manner. With the fast-increasing capacity requirement, non-orthogonal multiplexing access (NOMA) scenarios composing one of the critical parts of the fifth generation (5G) technology are proposed to fully optimize spectral efficiency. For example, the spectrally efficient frequency division multiplex (SEFDM) scheme has displayed the potential of non-orthogonal multiplexing, which inspires us to pay attention to spatial modes with non-orthogonality. In the physical sense, the order of spatial mode can be viewed as continuous like frequency. Thus, except for spatial modes with integer orders, spatial modes with fractional orders might also be considered for both FSO and fiber-optic transmission, which has the potential to become an alternative scheme[102–105]. Actually, some scientists have presented a kind of Bessel beam with non-integer order[106]. Such Bessel beam is defined by the Bessel function whose order could be an arbitrary value in the continuous domain. When such beams are involved in MDM communication systems, lots of unexplored issues need to be investigated, such as the stabilization of spatial modes with non-integer, compensation for loss of orthogonality between spatial channels, mode sorter at the receiver and so on.

C: Polarization-/mode-independent performance is a key requirement for communication systems. Thus, improving the robustness of SDM/MDM fiber-optic systems should be taken into account. So far, most of SDM/MDM communication demonstrations are implemented in the laboratory with a relatively stable external environment. Although the experimental results of these demonstrations are reasonably satisfactory for lab testing, Such solutions are currently unsuitable for industrial applications in practical real-world transmission networks because of various limitations. One of them is system stability. Compared to the SMF-based transmission link, larger performance fluctuation of SDM/MDM link has been observed due to time-dependent physical effects such as mode coupling and MDL. Such physical effects in SDM/MDM fibers are well-known to be induced by random imperfection, stressing, twisting and bending of fibers and other employed optical components. As a result of mode coupling, power exchange among specific mode channels and tends to randomly change over time. MDL will lead to random signal power variation among mode channels. In practice, any perturbation that might affect crosstalk distribution will result in performance fluctuation, limiting flexibility and reliability. For future commercialized SDM/MDM-related implementations, besides low cost and high throughput, consistent and reliable performance is highly desirable as well. However, dynamic performance evaluation and field experiments of SDM/MDM-based links have not been widely conducted and discussed to date. The issue whether the SDM/MDM-based links in the industrial implementation could withstand the environmental disturbance and outperform conventional SMF-based communication links requires more research.

D: Since SDM/MDM fiber-optic transmission links are sensitive to the surroundings as mentioned in the last paragraph. Such feature enables SDM/MDM technology with multi-modal configuration to find new applications in distributed fiber sensors where the forward or returning echo of each spatial channel could be collected and analyzed to monitor changes in the external environment, such as temperature, vibration, strain, pressure, bending, twisting, etc[107–109]. Furthermore, the response of each spatial channel within the waveguide for specific sensing parameter may be different and then each spatial channel could play the role of an orthogonal geophone. Therefore, SDM/MDM technology is capable of achieving some functionalities which are hard to realize in SMF-based deployments, such as simultaneous multi-parameter sensing. With parallel spatial channels, such a multi-modal sensor paradigm will be not only beneficial to the improvement of sensing sensitivity and detection speed, but also helpful in widening the range of sensing. In addition, implementing SDM/MDM in sensing systems has a comparative advantage of phase-/polarization-fading elimination. Similarly, some techniques in distributed fiber sensors could also be employed to characterize and evaluate SDM/MDM-based links, thereby providing better guidance for communication systems. With the development of SDM/MDM-based communication systems, fiber sensing applications related to SDM/MDM will attract more interest.

References

[1] N. Tirkey, V. Sahu, and S. M. Shrivastava, “High spatial multiplicity enhancement for dense sdm using multi-core few-mode or multi-mode fiber,” *i-Manager’s Journal on Communication Engineering and Systems*, vol. 6, no. 3, p. 31, 2017.

[2] A. Mecozzi, C. Antonelli, and M. Shtaif, “Kramers–Kronig coherent receiver,” *Optica*, vol. 3, no. 11, pp. 1220–1227, 2016.

[3] R.-J. Essiambre and R. W. Tkach, “Capacity trends and limits of optical communication networks,” *Proceedings of the IEEE*, vol. 100, no. 5, pp. 1035–1055, 2012.

[4] H. Chen and A. Koonen, “Spatial division multiplexing,” in *Fibre Optic Communication*, pp. 1–48, Springer, 2017.

[5] R. W. Tkach, “Scaling optical communications for the next decade and beyond,” *Bell Labs Technical Journal*, vol. 14, no. 4, pp. 3–9, 2010.

[6] C. Shannon, “Claude shannon,” *Information Theory*, vol. 3, p. 224, 1948.

[7] B. J. Puttnam, G. Rademacher, and R. S. Luís, “Space-division multiplexing for optical fiber communications,” *Optica*, vol. 8, no. 9, pp. 1186–1203, 2021.

[8] S. Inao, T. Sato, S. Sentsui, T. Kuroha, and Y. Nishimura, “Multicore optical fiber,” in *Optical Fiber Communication Conference*, p. WB1, 1979.

[9] S. Berdagué and P. Facq, "Mode division multiplexing in optical fibers," *Applied optics*, vol. 21, no. 11, pp. 1950–1955, 1982.

[10] D. J. Richardson, J. M. Fini, and L. E. Nelson, "Space-division multiplexing in optical fibres," *Nature photonics*, vol. 7, no. 5, pp. 354–362, 2013.

[11] N. Bozinovic, Y. Yue, Y. Ren, M. Tur, P. Kristensen, H. Huang, A. E. Willner, and S. Ramachandran, "Terabit-scale orbital angular momentum mode division multiplexing in fibers," *science*, vol. 340, no. 6140, pp. 1545–1548, 2013.

[12] G. Li, N. Bai, N. Zhao, and C. Xia, "Space-division multiplexing: the next frontier in optical communication," *Advances in Optics and Photonics*, vol. 6, no. 4, pp. 413–487, 2014.

[13] G. Milione, E. Ip, Y.-K. Huang, P. Ji, T. Wang, M.-J. Li, J. Stone, and G. Peng, "1.2-Tb/s MIMO-less transmission over 1 km of four-core elliptical-core few-mode fiber with 125-μm diameter cladding," in *OptoElectronics and Communications Conference (OECC) held jointly with International Conference on Photonics in Switching (PS)*, pp. 1–3, 2016.

[14] S. Li and J. Wang, "A compact trench-assisted multi-orbital-angular-momentum multi-ring fiber for ultrahigh-density space-division multiplexing (19 rings$\times$ 22 modes)," *Scientific reports*, vol. 4, no. 1, pp. 1–8, 2014.

[15] P. Gregg, P. Kristensen, S. Golowich, J. Olsen, P. Steinvurzel, and S. Ramachandran, "Stable transmission of 12 OAM states in air-core fiber," in *CLEO: 2013*, pp. 1–2, 2013.

[16] C. Brunet, B. Ung, L. Wang, Y. Messaddeq, S. LaRochelle, and L. A. Rusch, "Design of a family of ring-core fibers for OAM transmission studies," *Opt. Express*, vol. 23, no. 8, pp. 10553–10563, 2015.

[17] S. Beppu, D. Soma, S. Sumita, Y. Wakayama, H. Takahashi, T. Tsuritani, I. Morita, and M. Suzuki, "402.7-Tb/s MDM-WDM transmission over weakly

coupled 10-mode fiber using rate-adaptive PS-16QAM signals," *Journal of Lightwave Technology*, vol. 38, no. 10, pp. 2835–2841, 2020.

[18] R. Ryf, N. K. Fontaine, S. Wittek, K. Choutagunta, M. Mazur, H. Chen, J. Carlos Alvarado-Zacarias, R. Amezcua-Correa, M. Capuzzo, R. Kopf, A. Tate, H. Safar, C. Bolle, D. T. Neilson, E. Burrows, K. Kim, M. Bigot-Astruc, F. Achten, P. Sillard, A. Amezcua-Correa, J. M. Kahn, J. Schröder, and J. Carpenter, "High-spectral-efficiency mode-multiplexed transmission over graded-index multimode fiber," in *European Conference on Optical Communication (ECOC)*, pp. 1–3, 2018.

[19] G. Rademacher, B. J. Puttnam, R. S. Luís, T. A. Eriksson, N. K. Fontaine, M. Mazur, H. Chen, R. Ryf, D. T. Neilson, P. Sillard, F. Achten, Y. Awaji, and H. Furukawa, "1.01 Peta-bit/s C+L-band transmission over a 15-mode fiber," in *European Conference on Optical Communications (ECOC)*, pp. 1–4, 2020.

[20] L. Zhu, G. Zhu, A. Wang, L. Wang, J. Ai, S. Chen, C. Du, J. Liu, S. Yu, and J. Wang, "18 km low-crosstalk OAM + WDM transmission with 224 individual channels enabled by a ring-core fiber with large high-order mode group separation," *Opt. Lett.*, vol. 43, no. 8, pp. 1890–1893, 2018.

[21] J. Zhang, J. Liu, L. Shen, L. Zhang, J. Luo, J. Liu, and S. Yu, "Mode-division multiplexed transmission of wavelength-division multiplexing signals over a 100-km single-span orbital angular momentum fiber," *Photonics Research*, vol. 8, no. 7, pp. 1236–1242, 2020.

[22] B. J. Puttnam, R. S. Luis, W. Klaus, J. Sakaguchi, J.-M. D. Mendinueta, Y. Awaji, N. Wada, Y. Tamura, T. Hayashi, M. Hirano, *et al.*, "2.15 Pb/s transmission using a 22 core homogeneous single-mode multi-core fiber and wideband optical comb," in *European Conference on Optical Communication (ECOC)*, pp. 1–3, 2015.

[23] A. Turukhin, O. V. Sinkin, H. Batshon, H. Zhang, Y. Sun, M. Mazurczyk, C. R. Davidson, J.-X. Cai, M. A. Bolshtyansky, D. G. Foursa, *et al.*, "105.1 Tb/s power-efficient transmission over 14,350 km using a 12-core fiber," in *Optical Fiber Communications Conference and Exhibition (OFC)*, pp. 1–3, 2016.

[24] G. Rademacher, R. S. Luís, B. J. Puttnam, R. Ryf, S. van der Heide, T. A. Eriksson, N. K. Fontaine, H. Chen, R.-J. Essiambre, Y. Awaji, H. Furukawa, and N. Wada, "172 Tb/s C+L Band Transmission over 2040 km Strongly Coupled 3-Core Fiber," in *Optical Fiber Communication Conference Postdeadline Papers 2020*, p. Th4C.5, 2020.

[25] D. Soma, Y. Wakayama, S. Beppu, S. Sumita, T. Tsuritani, T. Hayashi, T. Nagashima, M. Suzuki, H. Takahashi, K. Igarashi, *et al.*, "10.16 peta-bit/s dense SDM/WDM transmission over low-DMD 6-mode 19-core fibre across C+L band," in *European Conference on Optical Communication (ECOC)*, pp. 1–3, 2017.

[26] G. Rademacher, B. J. Puttnam, R. S. Luís, J. Sakaguchi, W. Klaus, T. A. Eriksson, Y. Awaji, T. Hayashi, T. Nagashima, T. Nakanishi, *et al.*, "10.66 peta-bit/s transmission over a 38-core-three-mode fiber," in *Optical Fiber Communication Conference*, pp. Th3H–1, 2020.

[27] S. O. Arik, J. M. Kahn, and K.-P. Ho, "MIMO Signal Processing for Mode-Division Multiplexing: An overview of channel models and signal processing architectures," *IEEE Signal Processing Magazine*, vol. 31, no. 2, pp. 25–34, 2014.

[28] P. J. Winzer and G. J. Foschini, "Optical MIMO-SDM system capacities," in *Optical Fiber Communication Conference*, p. Th1J.1, 2014.

[29] K. Shi, Y. Jung, Z. S. Eznaveh, J. A. Zacarias, J. A. Lopez, H. Zhou, R. Zhang, S. Chen, H. Wang, Y. Yang, *et al.*, "10×10 MDM transmission over 24 km of ring-core fibre using mode selective photonic lanterns and sparse equalization," in *European Conference on Optical Communication (ECOC)*, pp. 1–3, 2017.

[30] S. Beppu, D. Soma, H. Takahashi, N. Yoshikane, I. Morita, and T. Tsuritani, "Experimental verification on digital back propagation gain in mcf transmission over 6020-km uncoupled and coupled 4-core fibres," in *European Conference on Optical Communications (ECOC)*, pp. 1–4, 2020.

[31] X. Wu, J. Zhang, Q. Fan, Z. Tan, J. Li, X. Yi, Z. Li, A. P. T. Lau, and C. Lu, "Dynamic Evaluation of Four CV Modes Multiplexing System Using Kramers–Kronig Reception and 4×4 Non-Singular MIMO," *Journal of Lightwave Technology*, vol. 40, no. 7, pp. 1962–1971, 2021.

[32] J. Zhang, X. Wu, Q. Fan, X. Yi, Z. Tan, J. Li, Z. Li, and C. Lu, "4×56 Gb/s MIMO-less Fiber-eigenmode multiplexing transmission over 3 km FMF," in *Optoelectronics and Communications Conference*, pp. W3B–3, 2021.

[33] D. Soma, S. Beppu, Y. Wakayama, Y. Kawaguchi, K. Igarashi, and T. Tsuritani, "257-Tbit/s Partial MIMO-based 10-Mode C+L-band WDM Transmission over 48-km FMF," in *European Conference on Optical Communication (ECOC)*, pp. 1–3, 2017.

[34] J. Liu, J. Zhang, J. Liu, Z. Lin, Z. Li, Z. Lin, J. Zhang, C. Huang, S. Mo, L. Shen, *et al.*, "1-Pbps orbital angular momentum fibre-optic transmission," *Light: Science & Applications*, vol. 11, no. 1, pp. 1–11, 2022.

[35] T. Hu, J. Li, D. Ge, Z. Wu, Y. Tian, L. Shen, Y. Liu, S. Chen, Z. Li, Y. He, and Z. Chen, "Weakly-coupled 4-mode step-index FMF and demonstration of IM/DD MDM transmission," *Opt. Express*, vol. 26, no. 7, pp. 8356–8363, 2018.

[36] K. Ingerslev, P. Gregg, M. Galili, F. Da Ros, H. Hu, F. Bao, M. A. U. Castaneda, P. Kristensen, A. Rubano, L. Marrucci, *et al.*, "12 mode, WDM, MIMO-free orbital angular momentum transmission," *Optics Express*, vol. 26, no. 16, pp. 20225–20232, 2018.

[37] R. Zhang, H. Tan, J. Zhang, L. Shen, J. Liu, Y. Liu, L. Zhang, and S. Yu, "A novel ring-core fiber supporting MIMO-free 50km transmission over high-order OAM

modes," in *Optical Fiber Communications Conference and Exhibition (OFC)*, pp. 1–3, 2019.

[38] L. Wang, R. M. Nejad, A. Corsi, J. Lin, Y. Messaddeq, L. Rusch, and S. LaRochelle, "Linearly polarized vector modes: enabling MIMO-free mode-division multiplexing," *Opt. Express*, vol. 25, no. 10, pp. 11736–11749, 2017.

[39] L. Zhu, A. Wang, S. Chen, J. Liu, Q. Mo, C. Du, and J. Wang, "Orbital angular momentum mode groups multiplexing transmission over 2.6-km conventional multi-mode fiber," *Opt. Express*, vol. 25, no. 21, pp. 25637–25645, 2017.

[40] D. G. Hall, "Vector-beam solutions of maxwell's wave equation," *Optics letters*, vol. 21, no. 1, pp. 9–11, 1996.

[41] G. Zhu, Z. Hu, X. Wu, C. Du, W. Luo, Y. Chen, X. Cai, J. Liu, J. Zhu, and S. Yu, "Scalable mode division multiplexed transmission over a 10-km ring-core fiber using high-order orbital angular momentum modes," *Opt. Express*, vol. 26, no. 2, pp. 594–604, 2018.

[42] J. Liu, S.-M. Li, L. Zhu, A.-D. Wang, S. Chen, C. Klitis, C. Du, Q. Mo, M. Sorel, S.-Y. Yu, X.-L. Cai, and J. Wang, "Direct fiber vector eigenmode multiplexing transmission seeded by integrated optical vortex emitters," *Light: Science & Applications*, vol. 7, no. 3, pp. 17148–17148, 2018.

[43] Y. Chen, L. A. Rusch, and W. Shi, "Integrated Circularly Polarized OAM Generator and Multiplexer for Fiber Transmission," *IEEE Journal of Quantum Electronics*, vol. 54, no. 2, pp. 1–9, 2018.

[44] Y. Wen, I. Chremmos, Y. Chen, G. Zhu, J. Zhang, J. Zhu, Y. Zhang, J. Liu, and S. Yu, "Compact and high-performance vortex mode sorter for multi-dimensional multiplexed fiber communication systems," *Optica*, vol. 7, no. 3, pp. 254–262, 2020.

[45] F. Yaman, E. Mateo, and T. Wang, "Impact of modal crosstalk and multi-path interference on few-mode fiber transmission," in *Optical Fiber Communication Conference*, pp. OTu1D–2, 2012.

[46] D. Soma, Y. Wakayama, S. Beppu, S. Sumita, T. Tsuritani, T. Hayashi, T. Nagashima, M. Suzuki, M. Yoshida, K. Kasai, *et al.*, "10.16-Peta-B/s dense SDM/WDM transmission over 6-mode 19-core fiber across the C+L band," *Journal of Lightwave Technology*, vol. 36, no. 6, pp. 1362–1368, 2018.

[47] R. Ryf, N. K. Fontaine, S. Wittek, K. Choutagunta, M. Mazur, H. Chen, J. C. Alvarado-Zacarias, R. Amezcua-Correa, M. Capuzzo, R. Kopf, *et al.*, "High-spectral-efficiency mode-multiplexed transmission over graded-index multimode fiber," in *European Conference on Optical Communication (ECOC)*, pp. 1–3, 2018.

[48] X. Zhu and J. M. Kahn, "Free-space optical communication through atmospheric turbulence channels," *IEEE Transactions on communications*, vol. 50, no. 8, pp. 1293–1300, 2002.

[49] K. Pang, H. Song, Z. Zhao, R. Zhang, H. Song, G. Xie, L. Li, C. Liu, J. Du, A. F. Molisch, *et al.*, "400-Gbit/s QPSK free-space optical communication link based on four-fold multiplexing of Hermite–Gaussian or Laguerre–Gaussian modes by varying both modal indices," *Optics letters*, vol. 43, no. 16, pp. 3889–3892, 2018.

[50] J. Zhang, F. Li, J. Li, Y. Feng, and Z. Li, "120 Gbit/s 2×2 vector-modes-division-multiplexing DD-OFDM-32QAM free-space transmission," *IEEE Photonics Journal*, vol. 8, no. 6, pp. 1–8, 2016.

[51] C. Paterson, "Atmospheric turbulence and orbital angular momentum of single photons for optical communication," *Physical review letters*, vol. 94, no. 15, p. 153901, 2005.

[52] L. C. Andrews, "Laser beam propagation through random media," in *SPIE-International Society for Optical Engineering*, 2005.

[53] W. Cheng, J. W. Haus, and Q. Zhan, "Propagation of vector vortex beams through a turbulent atmosphere," *Opt. Express*, vol. 17, no. 20, pp. 17829–17836, 2009.

[54] O. Edfors and A. J. Johansson, "Is Orbital Angular Momentum (OAM) Based Radio Communication an Unexploited Area?," *IEEE Transactions on Antennas and Propagation*, vol. 60, no. 2, pp. 1126–1131, 2012.

[55] X. Wu, J. Zhang, Q. Fan, Z. Tan, J. Li, X. Yi, Z. Li, A. P. T. Lau, and C. Lu, "Dynamic Evaluation of Four CV Modes Multiplexing System using KramersKronig Reception and 4×4 Non-Singular MIMO," *Journal of Lightwave Technology*, pp. 1–1, 2021.

[56] C. He, Y. Shen, and A. Forbes, "Towards higher-dimensional structured light," *Light: Science & Applications*, vol. 11, no. 1, pp. 1–17, 2022.

[57] Y. Shen and C. Rosales-Guzmán, "Nonseparable states of light: From quantum to classical," *Laser & Photonics Reviews*, p. 2100533, 2022.

[58] G. Milione, H. I. Sztul, D. A. Nolan, and R. R. Alfano, "Higher-order poincaré sphere, stokes parameters, and the angular momentum of light," *Phys. Rev. Lett.*, vol. 107, p. 053601, 2011.

[59] S. Chen, X. Zhou, Y. Liu, X. Ling, H. Luo, and S. Wen, "Generation of arbitrary cylindrical vector beams on the higher order poincaré sphere," *Opt. Lett.*, vol. 39, no. 18, pp. 5274–5276, 2014.

[60] B. Ndagano, H. Sroor, M. McLaren, C. Rosales-Guzmán, and A. Forbes, "Beam quality measure for vector beams," *Opt. Lett.*, vol. 41, no. 15, pp. 3407–3410, 2016.

[61] W. K. Wootters, "Entanglement of formation and concurrence.," *Quantum Inf. Comput.*, vol. 1, no. 1, pp. 27–44, 2001.

[62] Q. Zhan, "Cylindrical vector beams: from mathematical concepts to applications," *Adv. Opt. Photon.*, vol. 1, no. 1, pp. 1–57, 2009.

[63] A. Rubano, F. Cardano, B. Piccirillo, and L. Marrucci, "Q-plate technology: a progress review," *JOSA B*, vol. 36, no. 5, pp. D70–D87, 2019.

[64] G. Milione, D. A. Nolan, and R. R. Alfano, "Determining principal modes in a multimode optical fiber using the mode dependent signal delay method," *JOSA B*, vol. 32, no. 1, pp. 143–149, 2015.

[65] F.-T. An, K. S. Kim, D. Gutierrez, S. Yam, E. Hu, K. Shrikhande, and L. Kazovsky, "SUCCESS: a next-generation hybrid WDM/TDM optical access network architecture," *Journal of Lightwave Technology*, vol. 22, no. 11, pp. 2557–2569, 2004.

[66] H. Rohde, E. Gottwald, A. Teixeira, J. D. Reis, A. Shahpari, K. Pulverer, and J. S. Wey, "Coherent ultra dense wdm technology for next generation optical metro and access networks," *Journal of Lightwave Technology*, vol. 32, no. 10, pp. 2041–2052, 2014.

[67] A. Rashidinejad, A. Nguyen, M. Olson, S. Hand, and D. Welch, "Real-Time Demonstration of 2.4Tbps (200Gbps/) Bidirectional Coherent DWDM-PON Enabled by Coherent Nyquist Subcarriers," in *Optical Fiber Communication Conference (OFC)*, p. W2A.30, 2020.

[68] C.-H. Lee, W. V. Sorin, and B. Y. Kim, "Fiber to the Home Using a PON Infrastructure," *Journal of Lightwave Technology*, vol. 24, no. 12, pp. 4568–4583, 2006.

[69] M. Nakazawa, "Rayleigh backscattering theory for single-mode optical fibers," *J. Opt. Soc. Am.*, vol. 73, no. 9, pp. 1175–1180, 1983.

[70] Z. Wang, H. Wu, X. Hu, N. Zhao, Q. Mo, and G. Li, "Rayleigh scattering in few-mode optical fibers," *Scientific Reports*, vol. 6, no. 1, p. 35844, 2016.

[71] T. Gui, X. Wang, M. Tang, Y. Yu, Y. Lu, and L. Li, "Real-Time Demonstration of 600 Gb/s DP-64QAM SelfHomodyne Coherent Bi-Direction Transmission with Un-Cooled DFB Laser," in *Optical Fiber Communication Conference Postdeadline Papers*, p. Th4C.3, 2020.

[72] T. Zami, B. Lavigne, O. B. Pardo, S. Weisser, J. David, M. L. Monnier, and J.-P. Faure, "31.2-Tb/s real time bidirectional transmission of 78x400 Gb/s interleaved channels over C band of one 90-km SMF span," in *Optical Fiber Communication Conference*, p. W1B.5, 2018.

[73] J. A. Lazaro, C. Arellano, V. Polo, and J. Prat, "Rayleigh Scattering Reduction by Means of Optical Frequency Dithering in Passive Optical Networks With Remotely Seeded ONUs," *IEEE Photonics Technology Letters*, vol. 19, no. 2, pp. 64–66, 2007.

[74] D. Kim, B. G. Kim, T. Bo, and H. Kim, "80-km Reach 28-Gb/s/λ RSOA-based Coherent WDM PON Using Dither-Frequency-Tuning SBS Suppression Technique," in *Optical Fiber Communication Conference (OFC)*, p. Th3F.6, 2019.

[75] H.-H. Lin, C.-Y. Lee, S.-C. Lin, S.-L. Lee, and G. Keiser, "WDM-PON Systems Using Cross-Remodulation to Double Network Capacity with Reduced Rayleigh Scattering Effects," in *Optical Fiber Communication Conference/National Fiber Optic Engineers Conference*, p. OTuH6, 2008.

[76] C. H. Yeh, C. W. Chow, and H. Y. Chen, "Simple Colorless WDM-PON With Rayleigh Backscattering Noise Circumvention Employing m -QAM OFDM Downstream and Remodulated OOK Upstream Signals," *Journal of Lightwave Technology*, vol. 30, no. 13, pp. 2151–2155, 2012.

[77] L. Hu, G. Wu, H. Zhang, and J. Chen, "A 300-kilometer optical fiber time transfer using bidirectional TDM dissemination," in *Proceedings of the 46th Annual Precise Time and Time Interval Systems and Applications Meeting*, pp. 41–44, 2014.

[78] V. Houtsma and D. van Veen, “Bi-Directional 25G/50G TDM-PON With Extended Power Budget Using 25G APD and Coherent Detection,” *Journal of Lightwave Technology*, vol. 36, no. 1, pp. 122–127, 2018.

[79] J. Sakaguchi, W. Klaus, Y. Awaji, N. Wada, T. Hayashi, T. Nagashima, T. Nakanishi, T. Taru, T. Takahata, and T. Kobayashi, “228-Spatial-Channel Bi-Directional Data Communication System Enabled by 39-Core 3-Mode Fiber,” *Journal of Lightwave Technology*, vol. 37, no. 8, pp. 1756–1763, 2019.

[80] S. Chen, J. Liu, Y. Zhao, L. Zhu, A. Wang, S. Li, J. Du, C. Du, Q. Mo, and J. Wang, “Full-duplex bidirectional data transmission link using twisted lights multiplexing over 1.1-km orbital angular momentum fiber,” *Scientific Reports*, vol. 6, no. 1, p. 38181, 2016.

[81] T. Hu, J. Li, K. Zhang, F. Ren, Q. Mo, Y. Ke, C. Du, Z. Liu, Y. He, Z. Li, and Z. Chen, “Experimental Demonstration of Bidirectional MDM-WDM-TDM-PON Over Low Modal-crosstalk FMF,” in *Optical Fiber Communication Conference*, p. M3C.2, 2016.

[82] M. Selmi, Y. Jaouen, and P. Ciblat, “Accurate digital frequency offset estimator for coherent PolMux QAM transmission systems,” in *2009 35th European Conference on Optical Communication*, pp. 1–2, 2009.

[83] D. Godard, “Self-Recovering Equalization and Carrier Tracking in Two-Dimensional Data Communication Systems,” *IEEE Transactions on Communications*, vol. 28, no. 11, pp. 1867–1875, 1980.

[84] M. Ready and R. Gooch, “Blind equalization based on radius directed adaptation,” in *International Conference on Acoustics, Speech, and Signal Processing*, pp. 1699–1702 vol.3, 1990.

[85] J. Li, J. Zhang, F. Li, X. Huang, S. Gao, and Z. Li, “DD-OFDM transmission over few-mode fiber based on direct vector mode multiplexing,” *Opt. Express*, vol. 26, no. 14, pp. 18749–18757, 2018.

[86] K. Benyahya, C. Simonneau, A. Ghazisaeidi, N. Barré, P. Jian, J.-F. Morizur, G. Labroille, M. Bigot, P. Sillard, J. G. Provost, H. Debrégeas, J. Renaudier, and G. Charlet, "Multiterabit Transmission Over OM2 Multimode Fiber With Wavelength and Mode Group Multiplexing and Direct Detection," *J. Lightwave Technol.*, vol. 36, no. 2, pp. 355–360, 2018.

[87] K. Ingerslev, P. Gregg, M. Galili, F. Da Ros, H. Hu, F. Bao, M. A. Usuga Castaneda, P. Kristensen, A. Rubano, L. Marrucci, S. Ramachandran, K. Rottwitt, T. Morioka, and L. K. Oxenløwe, "12 Mode, MIMO-free OAM transmission," in *Optical Fiber Communications Conference and Exhibition (OFC)*, pp. 1–3, 2017.

[88] L. Shen, D. Ge, Y. Liu, L. Xiong, S. Chen, H. Zhou, R. Zhang, L. Zhang, J. Luo, and J. Li, "MIMO-Free $20-\mathrm{Gb/s} \times 4 \times 2$ WDM-MDM Transmission Over 151.5-km Single-Span Ultra Low-Crosstalk FMFs," in *European Conference on Optical Communication (ECOC)*, pp. 1–3, 2018.

[89] C. Brunet, B. Ung, L. Wang, Y. Messaddeq, S. LaRochelle, and L. A. Rusch, "Design of a family of ring-core fibers for OAM transmission studies," *Opt. Express*, vol. 23, no. 8, pp. 10553–10563, 2015.

[90] K. Benyahya, C. Simonneau, A. Ghazisaeidi, R. R. Muller, M. Bigot, P. Sillard, P. Jian, G. Labroille, J. Renaudier, and G. Charlet, "200Gb/s Transmission Over 20km of FMF Fiber Using Mode Group Multiplexing and Direct Detection," in *European Conference on Optical Communication (ECOC)*, pp. 1–3, 2018.

[91] J. Zhang, G. Zhu, J. Liu, X. Wu, J. Zhu, C. Du, W. Luo, Y. Chen, and S. Yu, "Orbital-angular-momentum mode-group multiplexed transmission over a graded-index ring-core fiber based on receive diversity and maximal ratio combining," *Opt. Express*, vol. 26, no. 4, pp. 4243–4257, 2018.

[92] G. Zhu, X. Wu, J. Liu, Y. Chen, J. Zhang, J. Zhu, C. Du, and S. Yu, "Random Degenerate-Mode-Mixing Independent OAM Mode-Group (De)multiplexing over

a Graded-Index Ring-Core Fiber," in *Asia Communications and Photonics Conference (ACP)*, pp. 1–3, 2017.

[93] K. Kikuchi, "Polarization-demultiplexing algorithm in the digital coherent receiver," in *Digest of the IEEE/LEOS Summer Topical Meetings*, pp. 101–102, 2008.

[94] B. Szafraniec, B. Nebendahl, and T. Marshall, "Polarization demultiplexing in stokes space," *Optics express*, vol. 18, no. 17, pp. 17928–17939, 2010.

[95] A. Vgenis, C. S. Petrou, C. B. Papadias, I. Roudas, and L. Raptis, "Nonsingular constant modulus equalizer for PDM-QPSK coherent optical receivers," *IEEE Photonics Technology Letters*, vol. 22, no. 1, pp. 45–47, 2009.

[96] C. B. Papadias and A. J. Paulraj, "A constant modulus algorithm for multiuser signal separation in presence of delay spread using antenna arrays," *IEEE signal processing letters*, vol. 4, no. 6, pp. 178–181, 1997.

[97] J. Ma, F. Xia, S. Chen, S. Li, and J. Wang, "Amplification of 18 OAM modes in a ring-core erbium-doped fiber with low differential modal gain," *Optics Express*, vol. 27, no. 26, pp. 38087–38097, 2019.

[98] Z. Xie, S. Gao, T. Lei, S. Feng, Y. Zhang, F. Li, J. Zhang, Z. Li, and X. Yuan, "Integrated (de) multiplexer for orbital angular momentum fiber communication," *Photonics Research*, vol. 6, no. 7, pp. 743–749, 2018.

[99] H. Huang, Y. Ren, G. Xie, Y. Yan, Y. Yue, N. Ahmed, M. P. Lavery, M. J. Padgett, S. Dolinar, M. Tur, *et al.*, "Tunable orbital angular momentum mode filter based on optical geometric transformation," *Optics letters*, vol. 39, no. 6, pp. 1689–1692, 2014.

[100] V. S. Lyubopytov, A. R. Gizatulin, A. Z. Tlyavlin, and A. K. Sultanov, "Optical-domain mode coupling compensation for mode division multiplexing systems," in *Optical Technologies for Telecommunications 2013*, vol. 9156, pp. 28–33, 2014.

[101] V. S. Lyubopytov, A. Tatarczak, X. Lu, R. V. Kutluyarov, S. Rommel, A. K. Sultanov, and I. T. Monroy, "Optical-domain compensation for coupling between optical fiber conjugate vortex modes," in *Conference on Lasers and Electro-Optics/Pacific Rim*, p. PDP_T12_1001, 2015.

[102] Y. Zhao, X. Zhong, G. Ren, and Z. Wu, "Fractional fourier transform of non-integer vortex beams," in *Optics and Photonics for Information Processing IX*, vol. 9598, pp. 119–125, 2015.

[103] Z. Xu, C. Gui, S. Li, J. Zhou, and J. Wang, "Fractional orbital angular momentum (OAM) free-space optical communications with atmospheric turbulence assisted by mimo equalization," in *Photonic Networks and Devices*, pp. JT3A–1, 2014.

[104] Y. Zhao, X. Zhong, G. Ren, S. He, and Z. Wu, "Capacity of arbitrary-order orbital angular momentum multiplexing system," *Optics communications*, vol. 387, pp. 432–439, 2017.

[105] J. Wang, J. Liu, S. Li, L. Zhu, C. Li, M. Luo, Q. Yang, and S. Yu, "Experimental demonstration of free-space optical communications using OFDM-QPSK/16QAM-carrying fractional orbital angular momentum (OAM) multiplexing," in *Optical Fiber Communications Conference and Exhibition (OFC)*, pp. 1–3, 2015.

[106] S. H. Tao, W. M. Lee, and X. Yuan, "Experimental study of holographic generation of fractional bessel beams," *Applied optics*, vol. 43, no. 1, pp. 122–126, 2004.

[107] Y. Weng, E. Ip, Z. Pan, and T. Wang, "Advanced spatial-division multiplexed measurement systems propositions—from telecommunication to sensing applications: a review," *Sensors*, vol. 16, no. 9, p. 1387, 2016.

[108] Z. Zhao and M. Tang, "Distributed fiber sensing using SDM fibers," in *Optoelectronics and Communications Conference*, pp. W4D–1, 2021.

[109] I. Ashry, A. Wang, and Y. Xu, "Mode-division-multiplexing of absorption-based fiber optical sensors," *Optics Express*, vol. 24, no. 5, pp. 5186–5202, 2016.